Whole-heart Coverage Quantitative First-pass Spiral Perfusion in
Cardiac Magnetic Resonance Imaging

A Dissertation

Presented to

the faculty of the School of Engineering and Applied Science

University of Virginia

in partial fulfillment
of the requirements for the degree

Doctor of Philosophy

by

Yang Yang

May

2016

APPROVAL SHEET

The dissertation

is submitted in partial fulfillment of the requirements

for the degree of

Doctor of Philosophy

_____
AUTHOR

The dissertation has been read and approved by the examining committee:

Michael Salerno
_____
Advisor

Craig H. Meyer
_____

Frederick H. Epstein
_____

Christopher M. Kramer
_____

John P. Mugler III
_____

_____

Accepted for the School of Engineering and Applied Science:

Craig H. Benson, Dean, School of Engineering and Applied Science

May

2016

Abstract

First-pass adenosine stress cardiac magnetic resonance (CMR) perfusion imaging is a promising modality for evaluating coronary artery disease (CAD) and is capable of providing comprehensive assessment of ischemia, function, and scarring[1-6]. Measuring the extent of ischemic myocardium accurately has important implications in determining patients that may benefit from revascularization[7]. The absolute quantification of perfusion reserve (PR) by CMR with whole heart coverage may more accurately reflect the extent of ischemia as compared to the relative assessment provided by SPECT[8]. However, current CMR perfusion techniques are limited by spatial coverage and dark-rim artifacts (DRA) which may be mistaken for true perfusion abnormalities resulting in false positive studies[9-12].

Spiral imaging trajectories are robust to motion, have high signal-to-noise ratios and are superior data acquisition efficiency compared to standard Cartesian trajectories. These advantages could help to reduce DRA artifacts which are known to be exacerbated by low spatio-temporal resolution[9]. Recent studies have demonstrated excellent image quality and high diagnostic accuracy of first-pass adenosine stress perfusion imaging using an optimized spiral pulse sequence[13]. However, this sequence was only capable of imaging 3 short-axis slices at heart rates up to 110 BPM without absolute quantification. Considering that greater than 10 million stress tests are performed in the US alone, improvements in the accuracy of non-invasive assessments of CAD could significantly reduce health care costs resulting from incorrect diagnoses. Therefore, we hypothesize

that whole-heart absolute quantification of perfusion using spiral trajectories can provide high quality images to detect small perfusion abnormalities and accurately assess the extent of ischemia. This hypothesis will be tested by the following specific aims:

Specific Aim #1 is to develop a 2D multi-slice spiral perfusion pulse sequence with whole heart coverage. (a) Design a spiral pulse sequence to achieve whole heart coverage. (b) Characterize the performance of different spiral trajectories and k-t sampling patterns for parallel imaging and compressed sensing reconstruction. (c) Perform retrospective reconstructions to validate the spiral trajectories and k-t sampling patterns. (d) Apply the sequence in clinical subjects.

Specific Aim #2 is to develop a reduced field-of-view (FOV) whole-heart coverage single-shot excitation spiral perfusion pulse sequence with outer volume suppression (OVS). (a) Design a 2D OVS pulse and validate its performance in phantom experiments. (b) Incorporate 2D OVS into the single-shot excitation spiral pulse sequence. (c) Compare the rFOV single-shot excitation perfusion sequence with normal FOV single-shot perfusion sequence in clinical patients.

Specific Aim #3 is to develop a quantitative spiral perfusion sequence with validation in phantoms and clinical patients. (a) Design a quantitative dual-contrast spiral perfusion sequence to quantify myocardial blood flow. (b) Validate the sequence in gadolinium phantoms and healthy volunteers. (c) Quantify absolute myocardial perfusion in patients with suspected CAD at both rest and stress.

Acknowledgement

I was totally stunned by the beautiful, high quality brain MRI images when I first saw them in 2009. I decided to switch gears from robotics to medical imaging that year and came to the United States to pursue a Ph.D. degree in medical imaging. I spent two years in Biomedical Research Imaging Center at the University of North Carolina at Chapel Hill. During that time, I learned MR physics and medical imaging processing techniques. I would like to thank my mentors Dr. Hongyu An and Dr. Weili Lin who provided me with the opportunity to conduct research in brain MRI.

Dr. Michael Salerno sparked my interest in MR pulse sequence design after I transferred from UNC to University of Virginia in 2011. Although he is a practicing doctor, Mike is very enthusiastic about MR technique development. His M.D./Ph.D. background provides him with a great perspective for us to undertake translational studies. I would like to thank Mike for the great support in my dissertation projects. He gave me the freedom and independency to develop MR pulse sequence. I really enjoyed my scientific discussions with Mike and he always has brilliant ideas to do some cool and innovative stuff. He is not only my advisor but also my friend in life. It is hard to imagine an advisor that will stay till very late at night to debug the sequence with his student and figure out the problem. It already is a legendary story among the technicians that the PI and his student worked together until 2 am at the scanner. I really appreciate Mike's effort in my Ph.D. career.

I would like to also thank my Ph.D. committee chair, Dr. Craig H. Meyer. He is the so-called 'father of spiral' among our students. He is very knowledgeable about MR

physics and pulse sequence. My dissertation is based on the spiral trajectory first-pass perfusion and Craig gave me a lot of great advice on spiral trajectory design, off-resonance correction etc., which improved my image quality dramatically.

I also need to thank Dr. Christopher M. Kramer for his great clinical support. Chris is an incredibly organized doctor and is always the first to respond my group emails about paper/abstract editing, scheduling meetings, etc. I want to also thank my committee member Dr. Frederick H. Epstein. He taught me that seeing the big picture is very important as a scientific researcher. A good researcher can not only do technical development but also vision the significance of the technique. Additionally, thanks to Dr. John P. Mugler, who is the most reliable person to get Siemens source code and very knowledgeable about the sequence development.

I need to specially thank Jayne Missel, our research study coordinator. Without her I could not have gathered data from healthy volunteer or clinical patients. Usually it is very hard to recruit subjects to do contrast-enhanced perfusion study. In addition, she acted like a big mom in our group and she always treated me as her family member.

Thanks to all of my colleague in the big MR groups at UVA. Advanced imaging fellows, Dr. Peter W. Shaw, Dr. Jorge A. Gonzalez and Dr. Pelbreton C. Balfour, they helped consent potential clinical patients to test my pulse sequence. I would like to thank Xiaoying Cai, Sophia Cui and Dr. Daniel Auger from Epstein's lab, and it was my pleasure to discuss project progress and cool stuff. I want to also thank Mattew Van Houten, Jonathan Pan, Eric Holland and Alan Hauser who helped me process the quantitative perfusion data.

Table of Contents

List of Figures

List of Tables

Chapter 1: Introduction

1.1   Coronary Arterial Disease

Coronary artery disease (CAD), also known as ischemic heart disease, is the most common type of heart disease in the United States. According to the Heart Disease and Stroke Statistics-2016 update report from the American Heart Association, an estimated 15.5 million Americans greater than 20 years of age have CAD and it is responsible for 1 in every 7 deaths in the United States in 2013[14]. Projections show that by 2030, the prevalence of CAD will increase an additional 18% from 2013 estimates[14].

The estimated direct and indirect cost of heart disease from 2011 to 2012 was $207.3 billion. CAD was the 2nd most expensive hospital primary discharge diagnosis in 2011, accounting for $10.4 billion. This cost is projected to increase by 100% between 2013 and 2030[15].

Catheter-based invasive x-ray angiography, the clinical gold standard for diagnosis of CAD, is performed more than a million times per year. However, recent retrospective analysis of the CathPCI Registry of the National Cardiovascular Data Registry demonstrated that only 38% of 397,954 patients without known heart disease who underwent elective invasive angiography had obstructive CAD[16]. This implies that current strategies which are used to inform decisions regarding invasive angiography need to be substantially improved to increase the diagnostic yield of cardiac catheterization in routine clinical practice.

Fractional flow reserve (FFR), an index of the physiological significance of a coronary stenosis, is defined as the ratio of maximal blood flow in a stenotic artery to normal maximal flow[17]. Typically, a normal coronary artery has an FFR value of 1.0. An FFR value of less than 0.80 can identify ischemia-causing coronary stenosis with an accuracy of more than 90%[18]. In the FAME study, investigators demonstrated that FFR guidance in addition to angiographic guidance resulted in significant reduction of the rate of composite end point of death in patients with multi-vessel CAD undergoing percutaneous coronary intervention[19]. Thus, improving the accuracy of non-invasive assessment of CAD could significantly reduce health care costs from unnecessary and expensive invasive procedures.

1.2 Myocardial Blood Flow and Myocardial Perfusion Reserve

The major vessels of coronary circulation are the left main coronary artery that divides into left anterior descending artery (LAD) and circumflex artery (LCx), and the right coronary artery (RCA). The left and right coronary arteries and their branches lie on the outer surface of the heart and are referred to as the epicardial coronary arteries. These arteries distribute blood flow to different regions of the heart muscle as shown in Figure 1.1.
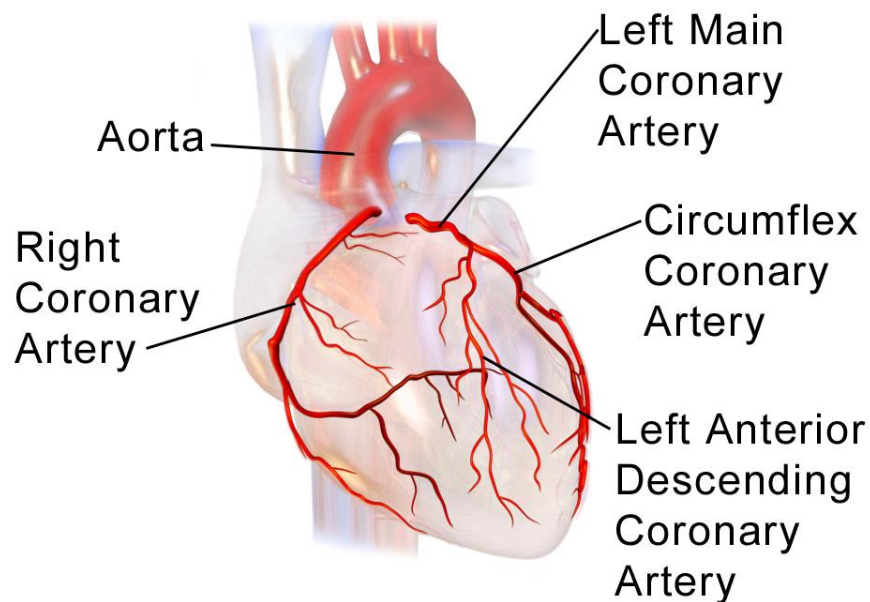
Figure 1.1 Illustration of coronary arteries. (Adapted from Wikipedia[20]:

https://en.wikipedia.org/wiki/Coronary_circulation#/media/File:Blausen_0256_CoronaryArteries_

02.png)

Myocardial blood flow is tightly coupled to oxygen demand. In non-diseased coronary vessels, whenever cardiac activity and oxygen consumption increases, there is an increase in blood flow that is nearly proportionate to the increase in oxygen consumption[21]. The endothelial cells that form the inner surface of coronary arteries dilate and constrict to modulate blood flow in response to physiologic triggers. In atherosclerosis[22], fatty or calcified plaques form on the endothelial surface of the artery, resulting in a luminal narrowing and a decrease in blood flow. This process results in coronary artery disease. Figure 1.2 shows a normal artery and a lipid plaque causing reduced myocardial blood flow.

Normal Artery   Narrowing of Artery

Lipid deposit of plaque
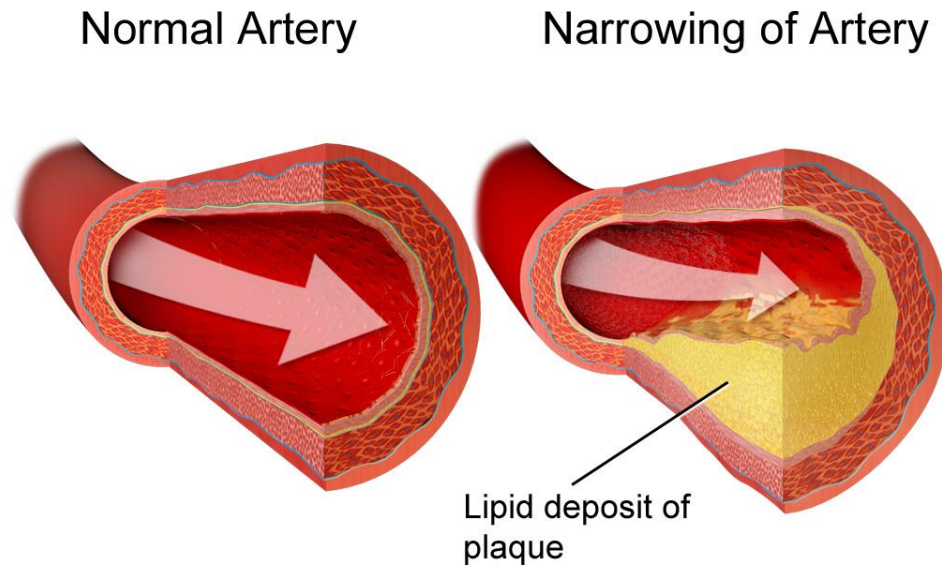
Figure 1.2 Normal artery and narrowing of artery caused by lipid deposit of plaque (Adapted

from Wikipedia[20,23]:

https://en.wikipedia.org/wiki/Coronary_artery_disease#/media/File:Blausen_0259_CoronaryArte

ryDisease_02.png)

Progressive ischemic coronary artery disease results in collateral flow through parallel vasculature and the growth of new vessels. Therefore, resting blood flow is not reduced until there is at least 85% stenosis of the artery[24]. However, under vasodilator stimulus, maximal coronary flow has been shown to decrease with stenosis of > 50%[24] (Figure 1.3). Because perfusion is affected early in the ischemic cascade, assessments of coronary perfusion reserve under stress have a higher sensitivity in detecting flow-limiting stenosis than analysis of stress-induced wall motion abnormalities. Myocardial perfusion reserve (MPR), which is the ratio of the stress flow and rest flow, inversely correlates with stenosis severity, and provides an assessment of the functional impact of increasing stenosis severity.
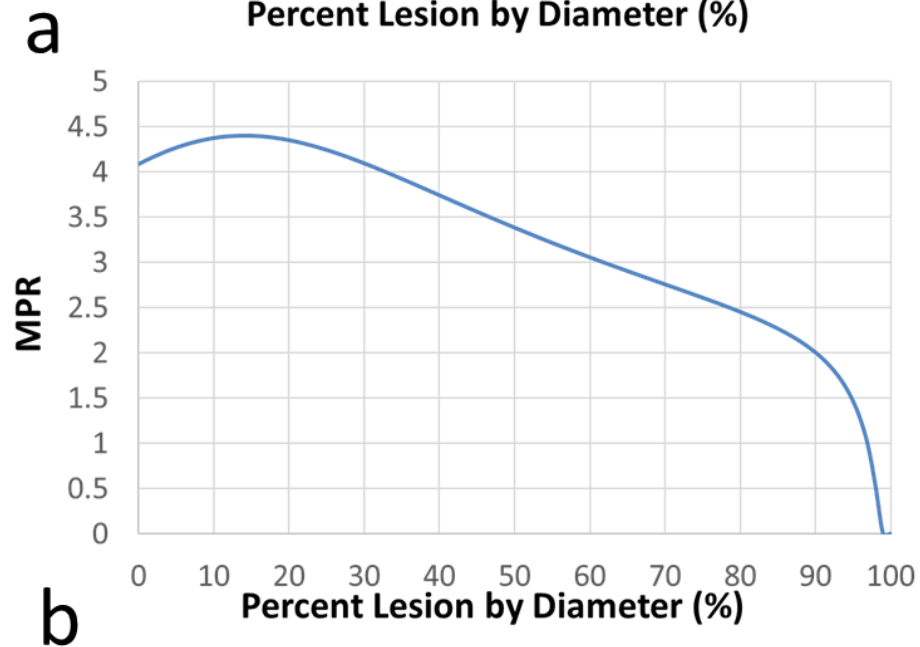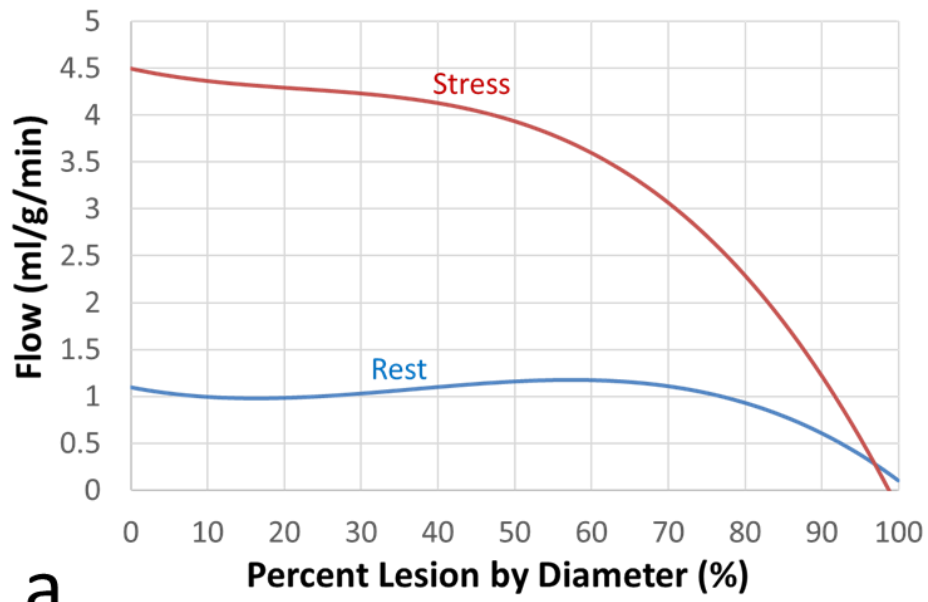
Figure 1.3 a) Relationship of the myocardial blood flow at rest and stress with percent lesion of the artery (stenosis), generated based on equation in the paper of Gould et al[24] and b) relationship of the MPR with stenosis level.

1.3 Non-invasive Assessment of Myocardial Perfusion

Multiple imaging modalities including single-photon emission tomography (SPECT), positron emission tomography (PET), myocardial contrast echocardiography (MCE), cardiac MRI (CMR) and cardiac computed tomography (CT) have been used to non-invasively assess myocardial perfusion in patients with known or suspected CAD. Each imaging modality has its own advantages and limitations.

SPECT myocardial perfusion imaging (MPI) is the most common stress test performed in the US, accounting for over 80% of the stress tests performed. Based on the flow or metabolism dependent selective uptake of a radioactive tracer by functional myocardial tissue[25]. SPECT MPI has been extensively studied and validated. Its advantages include compatibility with multiple stress modalities, and a relatively high SNR with longer data collecting time. However, it also has a number of limitations including the use of ionizing radiation, poor spatial resolution, and sensitivity to motion and attenuation artifacts. Furthermore, conventional SPECT MPI techniques only detect obstructive CAD by identifying regional differences in relative myocardial perfusion[26]. Due to the poor spatial resolution, SPECT cannot reliably detect the diffuse perfusion abnormalities in microvascular disease (MVD)[27].

PET MRI utilizes radiolabeled tracers to detect emitted photons to map a particular physiological process[28]. It allows accurate measurement of myocardial perfusion, absolute myocardial blood flow and function at stress and rest over a period of approximately 30 minutes. The spatial resolution is improved compared with SPECT and lower radiation doses are required. However, the use of PET MPI is still limited by the

higher costs and needs for a cyclotron to generate the radiotracers. Multiple studies have shown similar or superior diagnostic accuracy for PET compared to SPECT[29,30].

MCE utilizes gas-filled microbubbles to assess myocardial perfusion. During a steady state continuous infusion of microbubbles, a high energy ultrasound beam destroys the microbubbles and the rate of microbubble replenishment within the ultrasound beam is measured which represents the mean red blood cell velocity[31]. MCE has advantages of no ionizing radiation and relatively low cost. However, this technique is limited by poor reproducibility, sensitivity to respiratory motion and acoustic windows. In addition, there is no FDA-approved contrast agents for clinical MCE perfusion.

CMR MPI is based on the first-pass of a bolus of gadolinium-DTPA contrast agents to assess myocardial perfusion. CMR has the advantages of non-ionizing radiation, flexible imaging plane orientation, excellent soft tissue contrast and higher spatial resolution. The higher spatial resolution can resolve transmural differences in myocardial perfusion which could potentially help differentiate MVD from obstructive CAD. Of note , PET and CMR have higher accuracy for detecting CAD than SPECT[32].

CT MPI is based on the injection of iodinated contrast agent to measure the absorption of x-ray to match the concentration of iodine[33]. The CT MPI can achieve very high spatial resolution in short acquisition time. However, the image quality of CT is inversely related to the heart rate which limits its use for stress test. In addition, high dose of ionizing radiation is the main disadvantage of assessing perfusion with CT.

1.4 Quantitative Assessment of Myocardial Perfusion

Quantifying the myocardial ischemic burden (MIB) has important implications because only patients with greater than 10% ischemic myocardium can benefit from revascularization[7]. The rate of death or heart attack with or without revascularization correlates with the MIB in the COURAGE trial[8].

Currently, PET MPI is the only clinically available technique for absolute quantification of myocardial perfusion. Quantitative PET MPI can assess impaired microvascular function which has important prognostic utility. In a study of 2783 patients with known or suspected CAD, an MPR <1.5 was associated with a 5.6-fold risk of cardiac death at 3 years as compared to the highest tertile of MPR, and provided significant reclassification of intermediate-risk patients[34]. Even after accounting for the burden of atherosclerosis by coronary angiography, a reduced MPR by PET was independently associated with adverse cardiovascular outcomes, and patients with low MPR had similar event rates to those with significant obstructive CAD[35]. Diabetic patients with impaired MPR but without obstructive CAD have high cardiac event rates (2.8%/year) comparable to patients with known CAD, whereas diabetics with preserved MPR had low event rates, demonstrating the significance of altered microvascular performance among diabetics[34]. Abnormal MPR has also been demonstrated in metabolic syndrome which is associated with MVD[36]. Even though quantitative PET provides important prognostic utility, the presence of impaired MPR has significant limitations for differentiating between obstructive CAD and MVD. A recent study demonstrated that although preserved global MPR excludes multi-vessel disease, it is only 36% specific for detecting 3-vessel CAD due to the high prevalence of MVD which can also cause a diffusely reduced MPR[37].

1.5 Quantitative CMR Myocardial Perfusion Imaging

CMR is the application of MRI to the cardiovascular system to accurately assess the cardiac morphology, function, perfusion and myocardial viability[38] with an overall capacity unmatched by any other single imaging modality.

While CMR is not currently used clinically for quantitative MPR assessment, it has a number of potential advantages over PET for this application including, lack of ionizing radiation, greater availability, lack of need for an on-site cyclotron or generator, and higher spatial resolution to resolve transmural differences in myocardial perfusion which could potentially help differentiate MVD from obstructive CAD.

Quantification of myocardial perfusion using CMR has been an active research area in the past 2 decades. Quantitative CMR is performed both at stress and rest to calculate absolute MBF (ml/min/g) and MPR. The most common quantitative perfusion analysis techniques include: two-compartment modeling[39], Fermi function modeling[40], model-independent analysis[41] and Patlak plot analysis[42]. Pack et al compared these four methods in 20 human subjects[43] and found that rest perfusion estimates were not significantly different between all four analysis methods, however, stress flow from Fermi models were significantly 25% higher than the other three methods. MPR values with the models were not significantly different, indicating that any of these techniques could be used for MPR measurements. Our group previously demonstrated a stepwise decrease in MPR by quantitative CMR perfusion as the severity of coronary stenosis increases, and that quantitative but not visual analysis detected a larger MIB in patients with 3-vessel CAD as compared to those with single-vessel disease[44].

1.6 Spiral Trajectory

Non-Cartesian trajectories such as spiral or radial trajectories have recently been applied to first-pass myocardial perfusion imaging[45-48]. Non-Cartesian pulse sequences have attractive features such as high efficiency in traversing k-space, isotropic resolution and point-spread functions, and the lack of discrete ghosting resulting from motion. In this dissertation, the slew-limited spiral gradient trajectories were created using the optimal design of Meyer et al[49]. The k-space trajectory is defined as follow:

$$k(t) = A\tau(t)e^{i\omega\tau(t)} \tag{1.1}$$

where $\tau(t)$ is designed function of time. An algorithm that maximizes $\tau(t)$, and arbitrary function of time, for each subsequent k-space step subject to the above constraints is repeated until a desired number of gradient points are achieved.

The potential drawbacks of spiral trajectories include sensitivity to off-resonance and concomitant field gradients that can result in blurring and signal loss and to inconsistent data artifacts when the signal intensity varies between interleaves due to non-equilibrium magnetization. However, by carefully choosing the spiral trajectory using shorter readout spiral and performing semi-automatic or automatic off-resonance correction[50,51], the artifacts can be significantly reduced.

1.7 Accelerated Imaging

Parallel imaging techniques, such as SENSE[52], GRAPPA[53], and SPIRiT[54], have been widely used in MRI applications. Taking advantage of multiple receiver coils, the data acquisition can be accelerated because data obtained from each coil are acquired in parallel and each coil image is weighted differently by the spatial sensitivity of its coil.

These methods differ by the way how the sensitivity information is used[54], either explicitly (SENSE) or implicitly (GRAPPA and SPIRiT). When the sensitivities are known, SENSE is the optimal solution[55]. Among these methods, SPIRiT is based on self-consistency with the calibration and acquisition data. The general concept of SPIRiT is shown in Figure 1.4. For non-Cartesian SPIRiT, which treats the reconstruction as an optimization problem. The calibration consistency equation is enforced on Cartesian grids(red). The acquisition data consistency relationship between the Cartesian missing points and the non-Cartesian acquired points is shown in blue. These define a large set of linear equations that is sufficient for reconstruction. The optimization can be written as the unconstrained Lagrangian form:

$$\underset{x}{\text{argmin}} \quad \|Dx - y\|^2 + \lambda(\epsilon)\|(G - I)x\|^2 \qquad (1.2)$$

where the operator D selects only acquired k-space locations to compare with the acquired data y. G is a series of convolution operators that convolve the entire k-space with the appropriate calibration kernels. $\lambda(\epsilon)$ is the parameter to balance the data fidelity and calibration consistency.
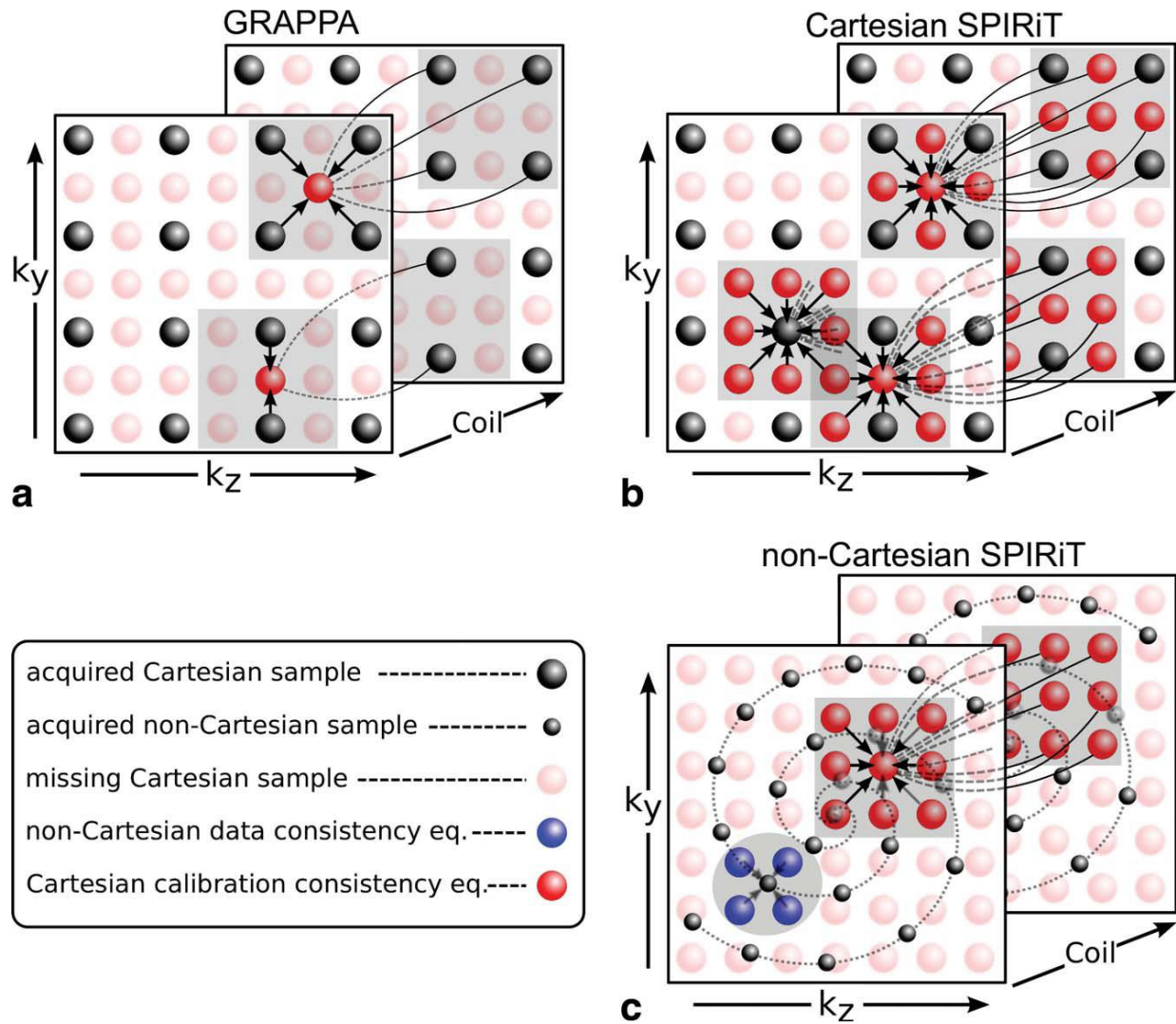
Figure 1.4 Illustration of the SPIRiT reconstruction method. (Adapted from Michael Lustig's SPIRiT[54] paper)

Recently, the compressed sensing[56] (CS) was introduced into the MR field by Lustig et al and it has dramatically changed the reconstruction and fast imaging field. By performing a CS reconstruction, much higher acceleration rates can be achieved with minimal degradation of image quality, unlike other conventional fast imaging techniques. The basic concept of CS theory is to exploit the sparsity of images to reconstruct images

using an optimization technique from a sub-Nyquist number of samples. Three major components are required for CS reconstruction: (1) the images must have a sparse representation in a transform domain, (2) the aliasing artifact due to undersampling must be incoherent and (3) a nonlinear reconstruction method must be used to enforce both sparsity of the image representation and consistency with the acquired data. The illustration of CS requirements is shown in Figure 1.4. Similar to SPIRiT reconstruction, the CS reconstruction can also be formulated as an optimization problem as follows:

$$\underset{x}{\text{argmin}} \quad \|\mathcal{F}_u x - y\|^2 + \lambda \|\psi x\|_1 \qquad\qquad (1.3)$$

Where the $\mathcal{F}_u$ is the undersampled Fourier operator to select the acquired kspace data, and ψ is the sparsifying transform.

Both the PI and CS reconstruction can be written as the optimization problem, providing the opportunity to combine these two techniques together to achieve higher acceleration for perfusion imaging by exploring the sparsity of dynamic images from multiple coils. In this dissertation, we will reconstruct images using the L1SPIRiT[57] technique which is a combination of PI and CS.
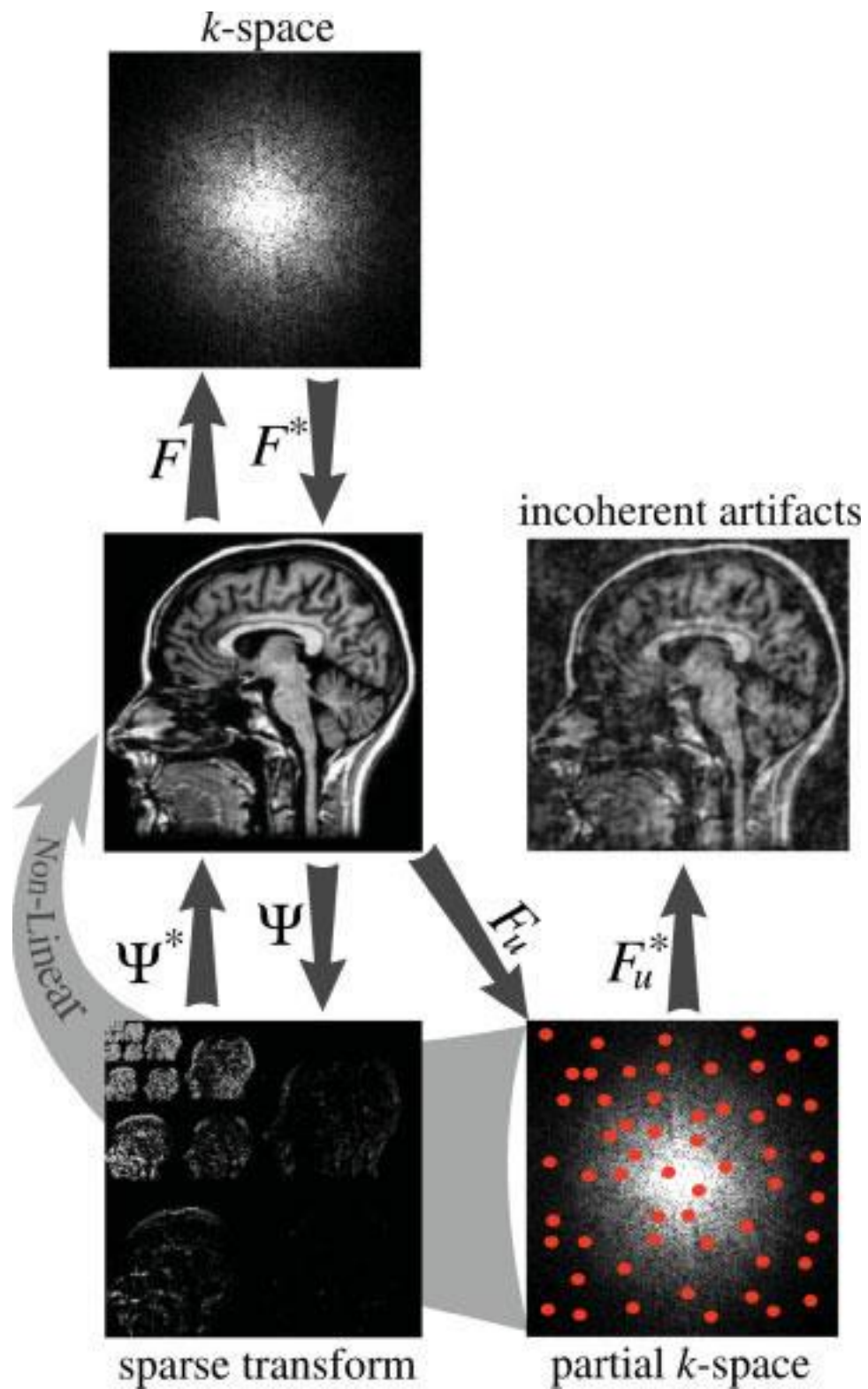
Figure 1.5 Illustration of the compressed sensing reconstruction method. (Adapted from Michael Lustig's Sparse MRI paper[58])

1.8 Challenges

Despite the potential advantages of first-pass perfusion imaging, a number of significant challenges and limitations still remain[10]. In-plane spatial resolution is typically >2-3mm, and there may only be 2-3 pixels across the myocardial wall particularly during diastole limiting accurate assessment of transmural perfusion gradients. Incomplete spatial coverage, consisting of 3-4 short axis slices, is insufficient to accurately quantify MIB. Motion-induced dark-rim artifacts (DRA) significantly reduce image quality and may impede the ability to measure endocardial perfusion which is most sensitive to myocardial ischemia[9,12].

Recent techniques such as high-resolution 2D kt-SENSE have high in-plane resolution but are limited to 3 slices[59]. 3D kt-PCA can more accurately assess MIB, but its long data-acquisition time (>225ms) results in sensitivity to cardiac and respiratory motion[60,61]. Non-Cartesian techniques (radial and spiral) have been shown to have reduced sensitivity to DRA[13,62], and may have advantages for motion compensated image reconstruction. However, 2D radial techniques have limited spatial coverage and are much less efficient than spirals, and spiral and radial 3D[63,64] techniques still require shorter temporal foot-prints to be robust for the increased heart rates present during vasodilator stress. The emerging field of CS has high potential for accelerating CMR perfusion imaging[45,65,66], but CS techniques are degraded by cardiac and respiratory motion which is common in clinical practice. We and others have developed motion-compensated CS techniques for myocardial perfusion imaging[67], but these techniques have yet to be clinically validated or combined with highly efficient trajectories.

1.9 Dissertation Goal

The goal of this dissertation is to develop whole-heart spiral perfusion sequences that allows for absolute quantification of myocardial perfusion. We hypothesize that the proposed techniques can improve detection of small perfusion abnormalities and accurately assess the extent of ischemia. This goal and hypothesis are explored in the following specific aims:

Specific Aim #1 is to develop a 2D multi-slice spiral perfusion pulse sequence with whole heart coverage. (a) Design a spiral pulse sequence to achieve whole heart coverage. (b) Characterize the performance of different spiral trajectory and k-t sampling pattern for parallel imaging and compressed sensing reconstruction. (c) Perform retrospective reconstructions to validate the spiral trajectory and k-t sampling pattern. (d) Apply the sequence in clinical subjects.

Specific Aim #2 is to develop a reduced field-of-view (FOV) whole-heart coverage single-shot spiral perfusion pulse sequence with outer volume suppression (OVS). (a) Design a 2D OVS pulse and validate its performance in phantom experiments. (b) Incorporate 2D OVS into the single-shot spiral pulse sequence. (c) Compare the rFOV single-shot perfusion sequence with normal FOV single-shot perfusion sequence in clinical patients.

Specific Aim #3 is to develop a quantitative spiral perfusion sequence with validation in phantom and clinical patients. (a) Design a quantitative dual-contrast spiral perfusion sequence to quantify myocardial blood flow. (b) Validate the sequence in

gadolinium phantom and healthy volunteers. (c) Quantify absolute myocardial perfusion in patients with suspected CAD at both rest and stress.

1.10 Dissertation Overview

This dissertation is organized as follows:

Chapter 1 provides the introduction and background of the dissertation.

Chapter 2 describes the design of a 2D interleaved order multi-slice spiral perfusion pulse sequence which achieves whole heart coverage for a heart rate of up to 125 beats per minute based on the timing and SNR considerations. The spiral trajectory and k-t sampling pattern is chosen from the retrospective reconstruction experiments. The proposed dual-density broad transition spiral trajectory with either angularly uniform or golden angle in time k-t sampling pattern is further validated in healthy volunteers and patients with suspected CAD.

Chapter 3 presents the design of a reduced FOV single-shot spiral pulse sequence. A novel 2D outer volume suppression module is developed and its performance is evaluated by numerical simulations. A spiral pulse sequence with a single excitation and spiral readout provides ultra-high temporal resolution without a loss in SNR. The proposed sequence is compared with the full FOV perfusion sequence and evaluated in clinical patents.

Chapter 4 details the design of a dual-contrast quantitative perfusion sequence which incorporates a low-resolution arterial input function (AIF) image to more accurately measure the signal intensities in the cavity. A signal modeling to convert the image

intensities to contrast agent concentration which accounts for the repeated acquisition of the center of k-space is developed and validated through phantom experiments. A full quantification pipeline is developed and implemented, and quantitative perfusion measurements are obtained in healthy volunteers and patients with known or suspected CAD.

Chapter 5 summarizes the work of this dissertation and discusses potential future directions for spiral perfusion imaging, including the outer-volume suppressed 3D stack-of-spiral imaging to get better SNR in same cardiac phase; simultaneous multi-slice acquisition to further improve the SNR for 2D imaging and multi-point AIF and tissue function techniques which could further improve the quantification accuracy.

Chapter 2: 2D whole heart coverage spiral perfusion

2.1 Introduction

First-pass contrast-enhanced myocardial perfusion MRI has proven to be a promising noninvasive technique for evaluating patients with known or suspected coronary artery disease (CAD), demonstrating excellent diagnostic and prognostic utility[2-4,68,69]. However, the technique has not yet gained widespread clinical adoption. One challenge that continues to limit its clinical use is achieving whole-heart coverage with high spatial resolution (≤2 mm) and with minimal artifacts, such as dark-rim artifact (DRA)[9]. Currently, a two-dimensional (2D) multi-slice saturation recovery (SR) prepared acquisition with parallel imaging (PI)[52,53] has been the most commonly used clinical method. With this approach, three to four short axis slices with 2–3 mm in-plane spatial resolution can be obtained per R-R interval[11]. Several investigators have used spatial-temporal acceleration techniques (k-t SENSE[70], k-t PCA[71]) to improve slice coverage and temporal/spatial resolution. 3D techniques have become available enabling whole-heart coverage but currently suffer from poor in-plane spatial resolution and a long temporal footprint resulting in increased sensitivity to cardiac motion-induced artifacts. Recently, the nonlinear reconstruction framework of Compressed Sensing (CS)[56,58] has garnered significant interest and has been applied to first-pass perfusion imaging[65,67]. By exploiting inherent data redundancy in terms of sparsity, the technique allows for the reconstruction of MR images from highly under-sampled data and may significantly shorten scan time.

Several investigators have explored utilizing temporal constraints to achieve high acceleration factors.[65,72]

Spiral or radial trajectories have recently been applied to first-pass myocardial perfusion imaging[45-48]. Non-Cartesian pulse sequences have attractive features such as high efficiency in traversing k-space, isotropic resolution and point-spread functions, and the lack of discrete ghosting resulting from motion. Non-Cartesian approaches are also compatible with PI and CS techniques, which could further reduce imaging time and improve temporal resolution. Potential drawbacks include sensitivity to off-resonance and concomitant field gradients which can result in blurring, signal loss, and sensitivity to inconsistent data artifacts when the signal intensity varies between spiral arms due to non-equilibrium magnetization. However, by carefully optimizing the spiral trajectory and reconstruction, these artifacts can be significantly mitigated. We have previously demonstrated high image quality and excellent clinical performance of spiral-based perfusion pulse sequences for the detection of obstructive CAD[69].

To design an optimal whole-heart coverage spiral pulse sequence for first-pass perfusion imaging, specific goals for resolution, timing, and signal-to-noise ratio (SNR) should be set and an acquisition strategy must be clearly defined. Our prior work has shown that by careful consideration of the spiral trajectory readout duration, flip angle (FA), and image reconstruction strategy, variable density (VD) spiral pulse sequences could produce high-quality first-pass perfusion images with minimal dark-rim and off-resonance artifacts, along with high signal-to-noise and contrast-to-noise ratios, and good delineation of resting perfusion abnormalities[13,62]. However, that sequence was still limited to three slice locations at heart rates up to 110 beats per minute (BPM). Thus, the

goal of the present study was to accelerate the spiral sequence to allow acquisition of at least eight slices covering the entire myocardium per R-R interval at heart rates up to 125 BPM using the combination of PI and CS techniques.

2.2 Methods

2.2.1 Design Consideration

To perform multi-slice 2D spiral perfusion imaging with whole-heart coverage, timing factors need to be considered including the total time available for imaging all slices at a given heart rate and the time required to image each slice. In order to determine the maximum number of first-pass perfusion slice positions that can be imaged during each heartbeat, the duration of the cardiac cycle (the R-R interval) under both resting and vasodilator stress conditions must be considered. Typically, heart rates vary between 60-90 BPM at rest, corresponding to R-R intervals of 667-1000 ms, and increases by approximately 20% under adenosine or regadenoson stress[73], some patients may have heart rates as high as 125 BPM, which corresponds to an R-R interval of only 480 ms. The second important consideration is the amount of time required to collect each spiral perfusion image. The total imaging time of saturation recovery based spiral sequence is determined by:

$$T_{total} = (T_{sat} + TS + TR * n_{arm}) * n_{slc} \hspace{2cm} (\,2.1\,)$$

$$= (T_{sat} + TS) * n_{slc} + TR * n_{arms} * n_{slc}$$

where T_{sat} is the saturation pulse duration, TS is the saturation recovery time to the first readout RF pulse, TR is the time of acquiring one spiral arm, n_{arm} is the number of spiral arms, and n_{slc} is the total number of slices. For example, a pulse sequence using our

previously developed VD trajectory[13], with the parameters $TS = 80$ ms, $TR = 9$ ms, $n_{leave} =$ 8, and 2 additional arms for field map estimation, can only support 3 slices up to a heart rate of 125 BPM. (Figure 2.1)

As seen in Equation 2.1, the total imaging time per heartbeat (T_{total}), can only be shortened by reducing the number of arms, the readout duration per arm, or saturation recovery time. For a slew-limited spiral with a fixed spatial resolution, fixed variable density sampling pattern, and fixed total readout duration per image, the product of the number of arms and the readout duration per arm is approximately constant[13]. As the number of spiral arms increases, the SNR is reduced as the optimal FA for a given saturation time and T_1 range decreases. Conversely, reducing the number of arms at the expense of a longer readout per spiral arm does not reduce the time to image each slice. While the TS can be reduced, this comes at the expense of SNR and reduced T_1 weighting. Thus, the most obvious way of shortening the T_{total} while maintaining the same T_1 weighting is to reduce the total number of arms by reducing the total sampling time and using parallel imaging techniques. For example, if only 2 out of 8 spirals (4x acceleration) were collected, the total readout time per image would be reduced to 18 ms instead of 72 ms. However, only 5 slices could be acquired at a heart rate of 125 BPM, as the total imaging time is dominated by the TS. For such a design, data acquisition would only occur for 18% of the R-R interval, which is very inefficient.

Therefore, the total amount of time waiting for T_1 preparation needs to be shortened. This can be achieved by acquiring multiple slices in an interleaved fashion following each saturation pulse, a concept which has previously been applied for EPI

perfusion imaging.[74,75] The total imaging time collecting multiple slices per SR preparation is given by

$$T_{total} = \left(T_{sat} + TS + TR * n_{arm} * \frac{n_{slc}}{n_{Sat}}\right) * n_{Sat}$$

$$= (T_{sat} + TS) * n_{Sat} + TR * n_{arm} * n_{slc}$$

(2.2)

where n_{Sat} is the total number of SR pulses and $\frac{n_{slc}}{n_{Sat}}$ determines the number of slices acquired during each SR pulse. The total imaging time can be dramatically reduced by using this strategy. Typically, just 2 slices per SR would meet these criteria while still reducing the total time to acquire each image by 50%, further reducing sensitivity to motion induced dark-rim artifacts as compared to a fully sampled pulse sequence. Figure 2.1 shows the supported slice numbers of the fully sampled sequence (VD-Full), 1 slice per SR of 4x sequence (VD-4x-1 Slc/SR) and 2 slices per SR of 4x sequence (VD-4x-2 Slc/SR) at heart rate ranges from 60 to 125 BPM. A 4x accelerated VD spiral pulse sequence with 2 slices per SR pulse would support 8 slices over a total temporal window of 464 ms, thus supporting whole-heart coverage while maximizing data collection efficiency. 4x acceleration (2/8 spiral arms) is the lowest possible acceleration factor which meets criteria for the chosen spatial resolution, number of spiral arms, readout duration per spiral arm, and saturation recovery time. In order to further reduce the spiral trajectory off-resonance effects, we chose to shorten the spiral readouts (5 ms) as compared to our prior design and utilize 3 arms, as described in the following section.

The above timing considerations still hold in this case.
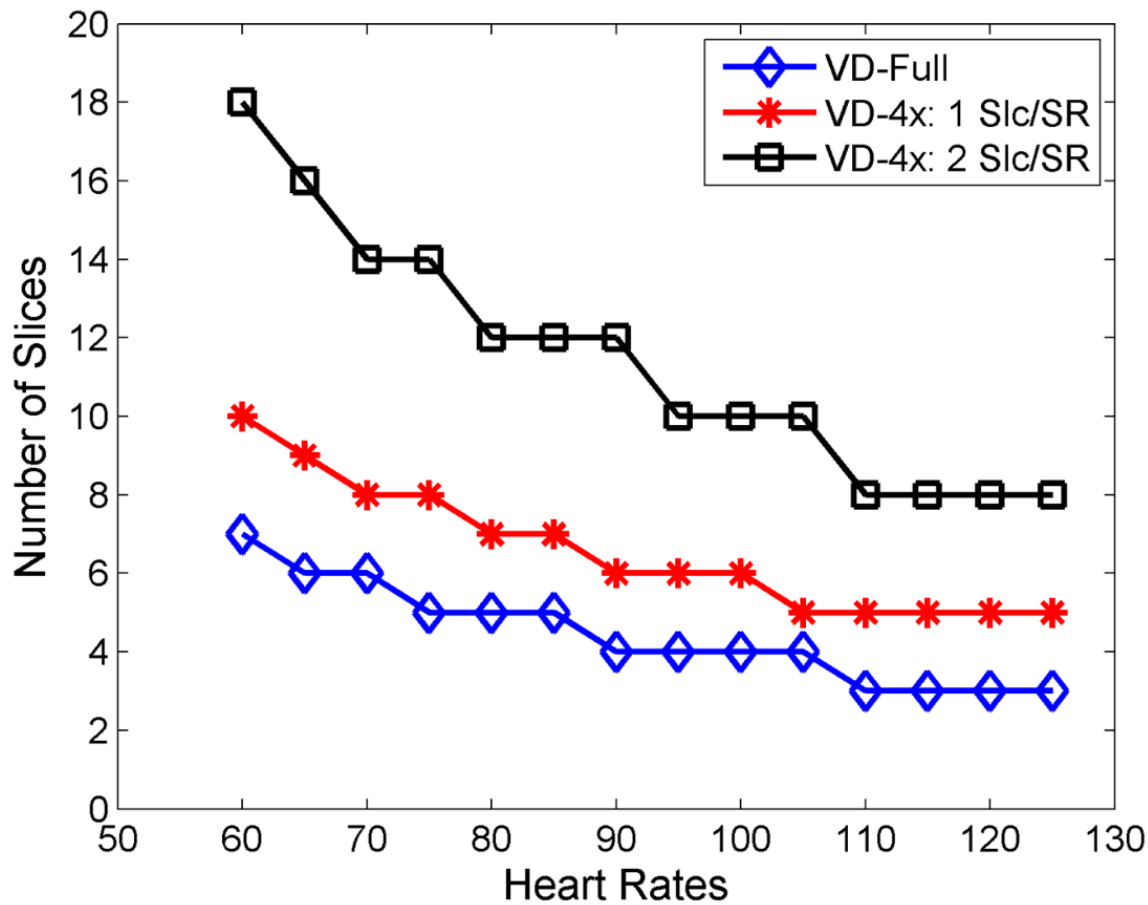
Figure 2.1 Relationship between the maximum supported slice numbers for the VD-Full sequence, VD-4x: 1Slc/SR and VD-4x: 2 Slc/SR at different heart rates. For the VD-Full sequence, only three slices are supported at the BPM of 125, while the accelerated VD-4x using 1 Slc/SR only acquires 5 slices. When two slices are imaged in one SR block, at least eight slices can be imaged at the heart rates of 125 BPM.

2.2.2 Sequential Slice Order vs Interleaved Slice Order

When more than one slice is imaged after each SR pulse, the acquisition order could be either sequential[75] or interleaved[74] as described previously. A sequential slice order has the advantage of shorter temporal window for each slice; however, each slice

would have a different effective T_1 weighting time (by 21 ms), while an interleaved acquisition order would have a longer temporal window for each individual image. However, with a slice interleaved acquisition, utilizing 3 spiral arms per image, the effective temporal resolution for each slice would be 5* TR (35 ms) which includes three spiral arms from slice 1 and two spiral arms from slice 2, which is still short enough to prevent motion-induced artifacts. Secondly, the TS times would only differ by 1 TR (7 ms), which would produce a negligible difference in apparent contrast weighting. An additional benefit of the interleaved slice order is that for a given saturation time, the effective TR (TR_{eff}) between arms for a given slice is doubled enabling a larger FA to be utilized to further improve SNR.

2.2.3 SNR Considerations

To ensure that transverse magnetization evolution is the same for each spiral arm, we have previously derived an optimal constant FA (θ_c) that exactly balances the loss in magnetization from each RF pulse[13] to the T_1 recovery of magnetization during each TR for a given TR, TS, and T_1: $\theta_c = cos^{-1}\left(\frac{E_1 - E_s}{E_1(1 - E_s)}\right)$, where $E_1 = exp(-TR/T_1)$ and $E_s = exp(-TS/T_1)$. The optimal FA for a 1 mmol/L gadolinium concentration (T_1 = 175 ms in 1.5T) with the TS = 80 ms is 21º for sequential order (TR = 7 ms) and 31º for interleaved order (TR = 14 ms).

Compared with the VD-Full sequence, the SNR of the VD-4x sequence was reduced by half due to shortening of the total readout time by a factor of 4. However, the larger FA with interleaved acquisition results in 40% greater transverse magnetization compared to a sequential acquisition. Thus, the SNR of a 4x accelerated technique

should only result in a 30% loss of SNR as compared to the non-accelerated sequence. Overall, these considerations indicate that the accelerated interleaved order 4x spiral sequence should have an acceptable SNR as compared to the fully sampled sequence. Furthermore, the use of compressed sensing should provide an increase in the visually apparent SNR of the image over that which is predicted by these theoretical considerations.

2.2.4 Spiral Trajectory Design

Slew-limited spiral gradient trajectories were created using the optimal spiral design of Meyer et al[76]. Briefly, the k-space trajectory is defined by specifying the desired number of arms, sampling time, number of points per trajectory, field of view (FOV), maximum gradient, slew rate parameters, and a function describing the relative sampling density (compared to Nyquist) as a function of time, and then computing the minimum-time gradient waveforms corresponding to the desired k-space trajectory. In order to determine the effect of spiral trajectory on the CS reconstruction, uniform density spiral (UD), variable linear density spiral (VD), and dual density spiral using a Fermi-function shape for transition region (DD) were evaluated. The dual density spiral design used the following parameterization:

$$k(n) = k_{start} - \frac{k_{start} - k_{end}}{1 + e^{-\tau(n-n_{fs})}} \qquad (2.3)$$

where k_{start} is the starting density, k_{end} is the ending density, $n_{fs} = round(npts * radius)$ is the number of points in the fully sampled center of k-space, and steepness (τ) is the parameter that determines the sharpness of the transition area.

For a fair comparison between strategies, all trajectories were designed to support the same spatial resolution. Furthermore, the duration of each arm is kept constant to achieve similar off-resonance performance for the different spiral trajectories.

Given the nature of VD spirals where the acceleration rate varies during the trajectory by design, the effective acceleration rate is defined as the corresponding constant acceleration factor required for a UD spiral trajectory to achieve the same desired FOV and maximum k-space radius (nominal spatial resolution) with the same number of arms and readout duration per arm. For instance, with the previously described design parameters, a UD sequence would have a density of 0.2x Nyquist corresponding to a 5-fold effective acceleration rate.

The spiral designs were chosen to span a wide range of trajectory parameters shown in Figure 2.2a. The UD spiral had a constant 5x under sampling factor which was advantageous from a SNR perspective, but had a coherent point-spread function (PSF), and did not fully sample low frequency high-energy data. Two VD trajectory patterns were evaluated. VD-1 had linearly decreasing density from 1x Nyquist to an under sampling density of 0.008x Nyquist at the edge of k-space. This produced very little ringing in the spatial PSF, but required a very high acceleration at the k-space edge which was least advantageous from a SNR perspective. VD-2 had less steep linearly decreasing density from 0.33x to 0.11x Nyquist and did not fully sample the center of k-space, which resulted in less non-uniform weighting of noise and a lower maximal under sampling factor as compared to VD-1. Two DD trajectory patterns were evaluated as well. The fully sampled radius was chosen to be 20% of the trajectory. In the literature the radius is typically 15-25% of the trajectory[46], and the overall trajectory is similar over this range of "radius". To

evaluate the effects of the transition region between the two k-space densities, we used either a sharp transition (τ =0.08) which required a final ending density of 0.18x Nyquist, or a broad transition (τ =0.02) which required a slightly lower final ending density of 0.13x Nyquist. Of note, while specific choices of τ and radius were chosen, small variations in these parameters did not significantly impact the general appearance of the spiral trajectories. Detailed information regarding the trajectories is shown in Table 2.1 and Figure 2.2a and 2.2b.

Table 2. 1 Spiral trajectories parameters

	UD	VD-1	VD-2	DD-1	DD-2
Number of spiral arms	3	3	3	3	3
Readout duration per arm (ms)	5.12	5.12	5.12	5.12	5.12
FOV (mm)	340	340	340	340	340
Starting density	0.2	1	0.33	1	1
Ending density	0.2	0.008	0.11	0.18	0.13
Fully sample k-space center (radius)*	N/A	N/A	N/A	20%	20%
Trajectory steepness (τ)*	N/A	N/A	N/A	0.08	0.02
Resolution (mm)	2.05	2.06	2.05	2.05	2.06

* Fully sampled k-space center and trajectory steepness is only used for dual density trajectories to determine the transition shape from starting density to ending density.
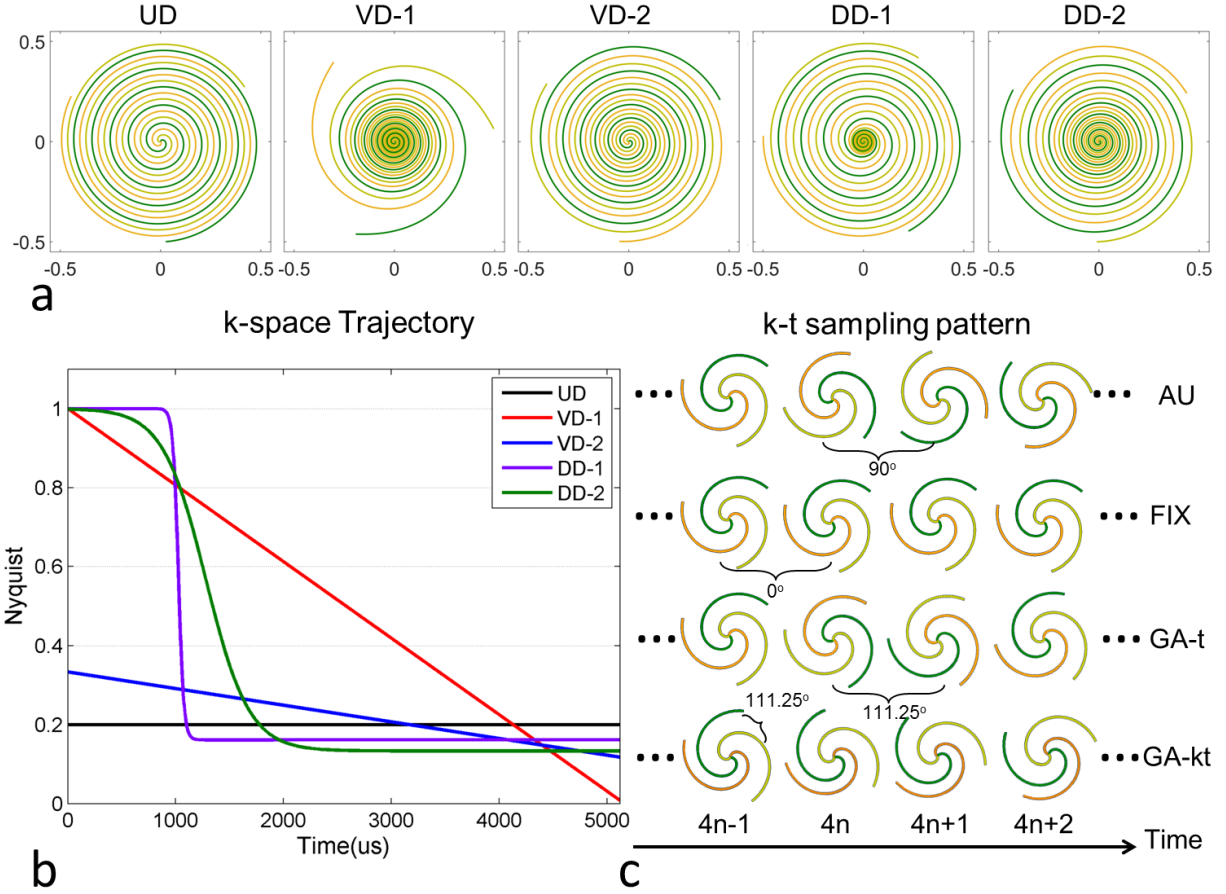
Figure 2.2 Combinations of k-space trajectories (a,b) and k-t sampling patterns (c). Five spiral trajectories include uniform density (UD), variable density from 1x Nyq to 0.008x Nyq (VD-1), variable density from 0.33x Nyq to 0.11x Nyq (VD-2), dual density with sharp transition (DD-1) and dual density with broad transition (DD-2). Four k-t sampling patterns include Angularly uniform (AU): within a heartbeat, three spirals were uniformly distributed and between heartbeats the sampling pattern was rotated by 90⁰ with a period of 4; Fixed (FIX): three spirals were fixed both within and between heartbeats; Golden angle rotation in time (GA-t): three spirals were uniformly distributed within heartbeat and rotated by a golden angle (111.25⁰) between heartbeats and Golden angle rotation in both k-space and time (GA-kt): each spiral was continuously rotated by golden angle within and between heartbeats.

29

2.2.5 k-t Sampling Pattern

For CS reconstruction the temporal k-t sampling pattern has to be considered. The small number of spiral arms for our proposed spiral pulse sequence limits the flexibility of the sampling pattern for each acquisition. A previous study showed that a sampling pattern employing rotations of angularly-uniformly spaced arms provided better image quality compared to randomly selected arms when temporal-difference sparsity was exploited[77]. As this pattern violates the concept of incoherent sampling in the temporal dimension which is advocated for compressed sensing, we evaluated the golden angle spiral sampling scheme[78]. As shown in Figure 2.2c, 4 types of k-t sampling patterns were evaluated in the retrospective simulation experiments: 1) angularly uniform (AU): within a heartbeat, 3 spirals were uniformly distributed and between heartbeats the sampling pattern was rotated by 90⁰ with a period of 4; 2) Fixed (FIX): 3 spirals were fixed both within and between heartbeats; 3) Golden angle in time (GA-t): 3 spirals were uniformly distributed within a heartbeat and rotated by a golden angle (111.25⁰) between heartbeats; 4) Golden angle in k-space and time (GA-kt): each spiral was continuously rotated by golden angle within and between heartbeats.

2.2.6 Pulse Sequence Design

The pulse sequence is shown schematically in Figure 2.3. A non-selective saturation with an adiabatic BIR-4 pulse[79] is used for T_1-weighting preparation. Before data acquisition, a spectrally selective fat-saturation pulse is applied. Then, 3 spirals for each image are obtained in the interleaved order for 2 different slice locations separately to create the perfusion image. Therefore, 2 slices are acquired in one SR block, and SR blocks are repeated until all the slices are imaged.
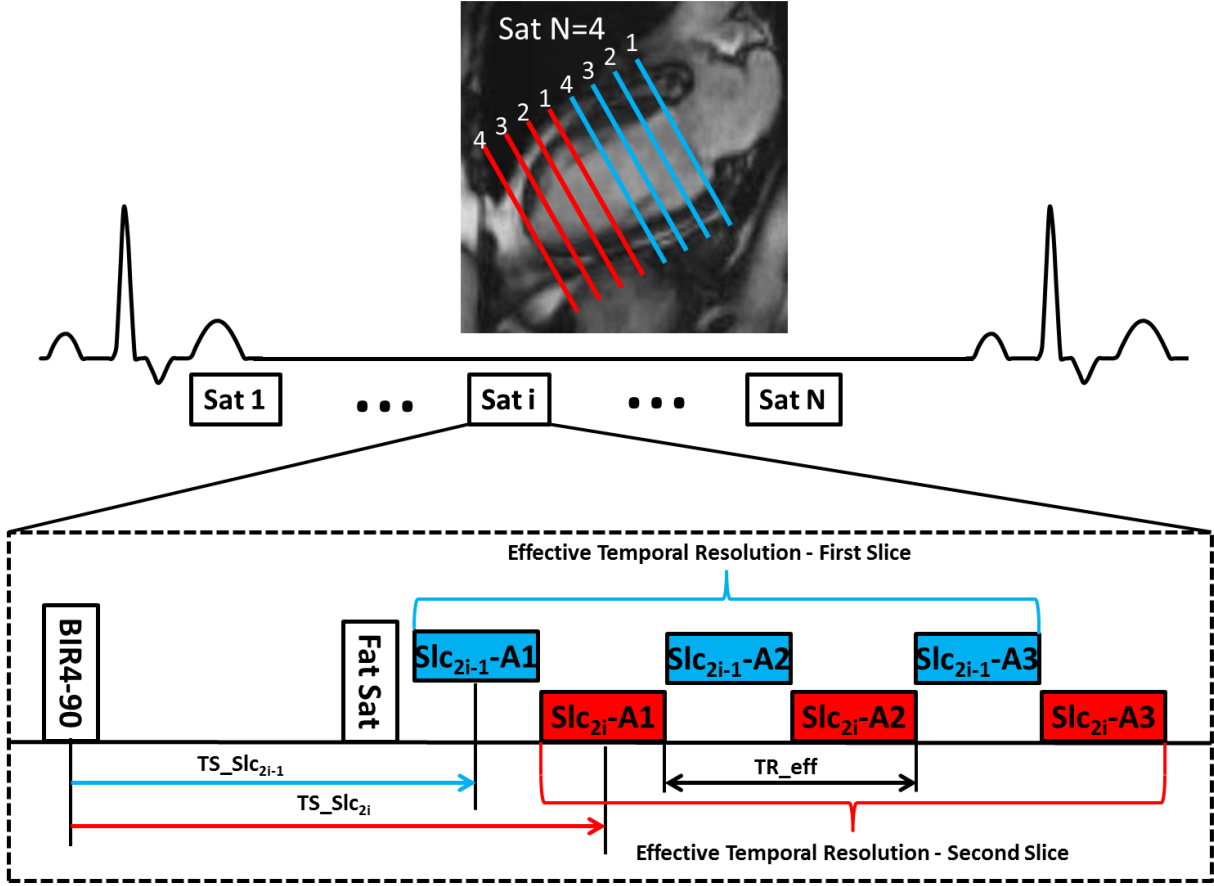
Figure 2.3 Pulse sequence schematic for the whole-heart coverage SR first-pass spiral perfusion imaging. At each SR sequence block, following the BIR4 SR pulse, a fat saturation pulse is applied and then followed by interleaved spiral imaging at two slice locations. Each slice is sampled by three interleaved spiral readouts (boxes) each with a TR of 7 ms. Due to the slice interleaving, the effective temporal resolution of each slice is 5*TR (35 ms), and the TS times differ by 1 TR (7 ms).

2.2.7 Image Reconstruction

For a 2x acceleration factor non-Cartesian PI techniques such as SPIRiT or non-Cartesian SENSE perform well for spiral perfusion imaging[80,81], however their performance is inadequate at acceleration factors of 4-5x. At higher acceleration, additional prior information must be exploited to achieve high quality reconstructions. We

have previously demonstrated that L1-SPIRiT using temporal finite difference as the sparsifying transform performed well at a 4x acceleration factor for this application[80,82]. Therefore, images in this study were reconstructed using the combination of PI and CS techniques, L1-SPIRiT[54,82,83]. The reconstruction problem could be formulated as:

$$minimize \quad \ell_1(\Psi x)$$
$$s.t. \quad SDFx = y, Gx = x$$

(2.4)

where F is a Fourier operator which transfers the data from image domain to k-space domain, D is the inverse gridding operator that transfers the Cartesian grid to spiral trajectory, S is the subsampling operator that chooses only acquired spiral k-space data out of the entire k-space trajectory, y is the acquired spiral k-space data, and G is an image-space SPIRiT operator that represents the k-space self-consistency convolutions in the image domain. The calibration kernel is estimated from gridding of the fully sampled k-space center using non-uniform FFT (NUFFT)[84]. Ψ is the finite time difference transform that operates on each individual coil separately to achieve sparsity in the temporal domain of image time series.

The above equation can be reformulated as the unconstrained Lagrangian form:

$$\underset{x}{\text{argmin}} \quad \|SDFx - y\|^2 + \lambda_1\|(G - I)x\|^2 + \lambda_2\|\Psi x\|_1$$

(2.5)

where λ_1 and λ_2 are parameters that balance the data acquisition consistency with calibration consistency and sparsity.

The SPIRiT calibration kernel G needs to be derived from the fully sampled, aliasing free data. Either an upfront pre-scan or temporal averaging of the under-sampled

data could generate alias free images for calibration. In practice, we typically acquire fully sampled proton density images over the first 4 heart beats of the acquisition to perform calibration. This strategy results in high SNR and high spatial resolution training data without variation in signal intensity resulting from imaging during the first pass of the contrast agent.

The image reconstruction was implemented in Matlab (The MathWorks, Natick, MA). The image-based non-Cartesian reconstruction used Fessler's NUFFT code[84]. The nonlinear iterative conjugated gradient descent algorithm with backtracking line search was used to solve the optimization problem. The absolute value function was approximated by a smooth function as described by Lustig et al[58].

2.2.8 Retrospective Study

L1-SPIRiT reconstruction performance for the 5 spiral trajectories (UD, VD-1, VD-2, DD-1, DD-2) described above and 4 different k-t sampling patterns (AU, FIX, GA-t and GA-kt) was quantitatively assessed using data from 25 multi-coil fully-sampled first-pass spiral perfusion images from previously published clinical study of adenosine stress CMR including 16 rest and 9 stress data sets[69]. The acquisition protocol and technical details of the sequence were described previously and include the following parameters: saturation recovery time of 80 ms echo time, 1 ms; repetition time, 9 ms; slice thickness, 10 mm; flip angle, 30°, field of view, 320 mm^2; 8 spiral interleaves; 6.1 ms readout duration per spiral arm; and nominal spatial resolution of 2 mm[13]. Inverse gridding was performed by taking the complex image data from each coil at each time point and resampling it onto the specific non-uniformly sampled spiral k-space trajectory using reverse NUFFT[84]. Image reconstructions of the different combinations of trajectories and sampling patterns

described above were performed using L1-SPIRiT with the goal of quantitatively evaluating the reconstruction performance compared to the fully-sampled "ground-truth" datasets.

Image quality was assessed across the whole image and in the heart region using root mean square error (RMSE) and structural similarity index (SSIM), which is a comprehensive measurement of the similarity between two images, and includes measurement of structure, intensity and contrast, representing human perception more closely[85]. The mean SSIM is defined by:

$$SSIM(x, y) = \frac{1}{N} \sum_{i=1}^{N} \frac{(2\mu_{xi}\mu_{yi} + c_{1i})(2\sigma_{xiyi} + c_{2i})}{(\mu_{xi}^2 + \mu_{yi}^2 + c_{1i})(\sigma_{xi}^2 + \sigma_{yi}^2 + c_{2i})} \qquad (2.6)$$

where μ_{xi}, μ_{yi} and σ_{xi}, σ_{yi} are the mean and variance of images x and y at time frame i, σ_{xiyi} is the covariance of x_i and y_i at time frame i, c_{1i} and c_{2i} are variables which stabilize the division with a weak denominator between x_i and y_i, and are selected as described by Wang et al[85].

The RMSE and SSIM from the 25 simulation datasets were analyzed using a blocked two-way ANOVA factorial design to determine the best combination of the evaluated spiral trajectories and k-t sampling patterns. The model included the 2-way interactions between trajectory and sampling pattern and a p-value <0.05 was considered significant.

In addition, signal-intensity time courses were evaluated to compare the temporal fidelity between the reconstructed images and ground truth images, using 3 different

manually defined regions of interest (ROI): left ventricular blood pool (LV), right ventricular blood pool (RV) and myocardium.

2.2.9 Prospective Study

Based on the results from the retrospective study of the spiral trajectories and k-t sampling pattern analysis, the DD-2 spiral trajectory with AU and GA-t sampling strategies were evaluated prospectively in a total of 34 subjects. Resting first-pass perfusion was performed in 24 subjects undergoing clinically ordered CMR studies using the DD-2 trajectory with either GA-t (N=8) or AU (N=16). Additionally, 2 normal subjects were imaged at rest using the DD-2 sampling pattern with both of the k-t sampling patterns (AU and GA-t) to allow for direct comparison between these two candidate sampling patterns. In these studies, the same dose of contrast 0.075mmol/kg Gd-DTPA (Bayer Pharmaceuticals) was used for each injection, and the two acquisitions were separated by a 20 minute period to allow for contrast washout. As part of an ongoing clinical evaluation of the spiral perfusion sequences, 8 subjects were imaged at rest and stress during a 3 minute infusion of 140 mcg/kg/min of adenosine (Astellas Pharmaceuticals) using the AU temporal pattern. Written informed consent was obtained from all subjects, and imaging studies were performed under institutional review board (IRB) approved protocols. Imaging was performed on a 1.5T MR Scanner (Magnetom Avanto, Siemens Healthcare). The Siemens body matrix and spine matrix phased-array coils were used in triple mode yielding between twelve and eighteen effective coil channels depending on the size and positioning of the patient. The 8 studies performed under stress utilized a 32-channel phased-array receiver coil. Four proton density images were acquired at the beginning of data acquisition for calibration purpose. Fifty perfusion images covering the

35

whole heart were obtained during injection of 0.075 mmol/kg Gd-DTPA via a peripheral IV at a rate of 4mL/s. Other pulse sequence parameters were as follows: TS 80 ms, TE 1.0 ms, 5 ms spiral, 3 spirals per slice, effective TR 14 ms, FA 30º, 8 to 10 slices to cover the whole heart, 2 slices per saturation, FOV 340mm^2, and in-plane resolution around 2mm.

Perfusion images were reconstructed using the proposed L1-SPIRiT method. The reconstruction parameters $\lambda_1 = 0.01$ and $\lambda_2 = 0.05$ were chosen based on an analysis of the SSIM and RMSE metrics as compared to the fully sampled ground truth data and the parameters were fixed for all datasets. Image quality was graded on a 5-point scale (1-excellent, 5-poor) independently by two cardiologists. Scores from the two reviewers were analyzed using the Wilcoxon signed rank test. Image quality of the GA-t and AU k-t sampling strategies was analyzed using the Mann-Whitney U test.

2.3 Results

2.3.1 Simulation

Figure 2.4 shows the PSF of the five evaluated k-space trajectories with 5 ms RO per arm. The UD trajectory has several very high side lobes with a peak amplitude of 8% of the main lobe. This trajectory has the least incoherent sampling pattern and is the worst case scenario for a CS type reconstruction. The VD-1 trajectory has the most incoherent side lobe energy distribution, which is good for CS type reconstruction, however the side lobe peaks are relatively high (around 5% of the main lobe), which would be unfavorable for a PI type reconstruction. The VD-2 trajectory has a similar PSF with VD-1 with the exception that there is no fully sampled region in the trajectory for calibration. In contrast

to the VD trajectories, the DD has fully sampled regions in the k-space center; the broad transition trajectory DD-2 is a good trade-off solution between incoherency for CS reconstruction and calibration for PI reconstruction. Notably, the PSF only describes the spatial pattern resulting from the given trajectory at a single time point, and may not fully characterize the incoherence of the sampling pattern. However, the analysis shows that the different trajectories result in different PSF which could impact the performance of the reconstruction technique.
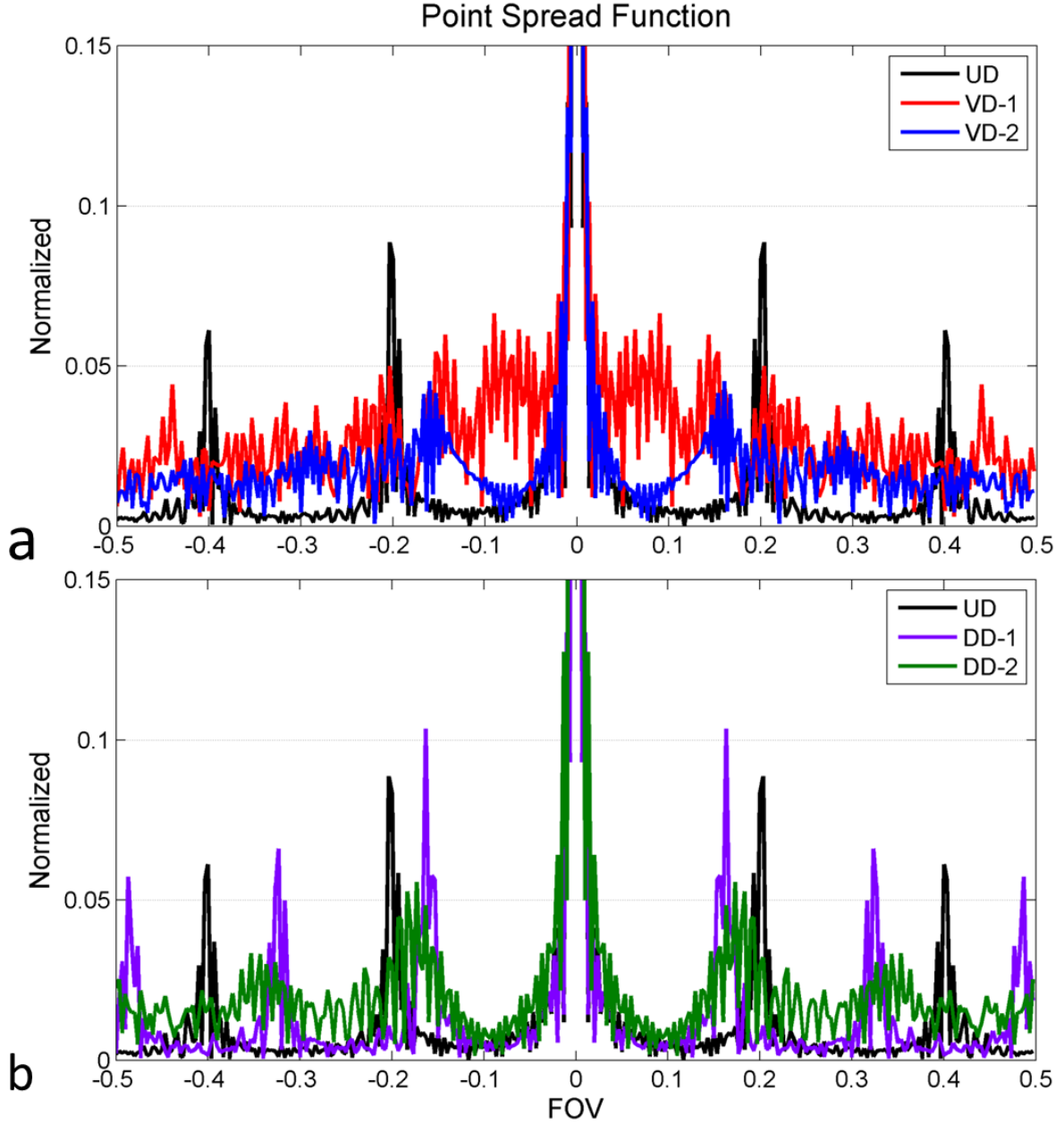
Figure 2.4 Point spread function of the k-space trajectories. The VD-1, DD-1, and DD-2 trajectories have the fully sampled k-space center which could be used for calibration kernel training. UD trajectory has strong coherent side lobes and DD-1 has a similar coherent side lobe distribution. a: VD-1 trajectory has the most incoherent PSF but the side lobe energy is around 5% of the main lobe. b: DD-2 trajectory is the trade-off between the fully sampled center calibration and incoherent side lobe distribution.

Figure 2.5 summarizes the RMSE and SSIM results from the heart region of the 25 datasets with all combinations of the trajectories and k-t sampling patterns. It is evident that all the k-t sampling patterns have reasonably small RMSE and high SSIM, except for the trajectories utilizing a fixed temporal sampling pattern. The main effects of trajectory type, k-t sampling pattern, and the interaction between trajectory and sampling pattern were all significant ($p<0.001$). When controlling for the k-t sampling pattern and interactions between trajectory and sampling pattern, DD-2 had the highest estimate for SSIM ($p<0.05$). When controlling for trajectory and the interaction between trajectory and sampling pattern, there was no significant difference between AU, GA-t and GA-kt, however, these patterns were all better than FIX ($p<0.05$). When considering the individual combinations of trajectory and k-t sampling pattern, DD-2 with AU, DD-2 with GA-t, VD-2 with AU, VD-2 with GA-t and DD-1 with GA-kt (stars indicated in Figure 2.5b) formed the group with the highest SSIM values with no significant difference in SSIM within the group. The DD-2 trajectory with AU and GA-t temporal sampling pattern had the smallest point estimates for RMSE, the highest SSIM, and a fully sampled k-space center for calibration, therefore were chosen for prospective evaluation. Similar results in RMSE and SSIM analysis were found over the entire image. The UD trajectory reconstructions frequently had residual coherent aliasing resulting in higher RMSE and SSIM than the other trajectories.
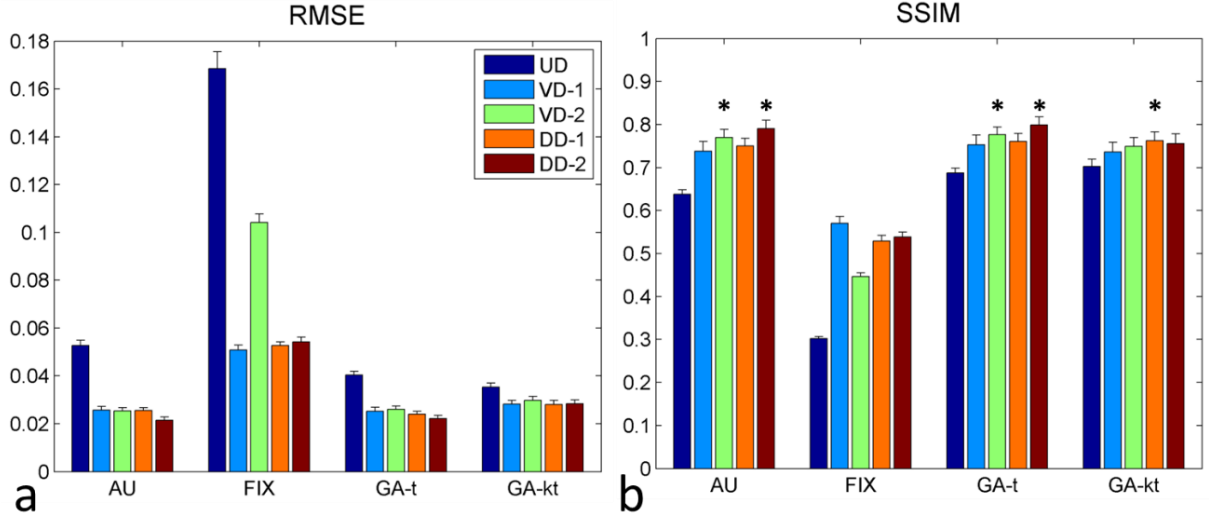
Figure 2.5 Quantitative analysis of the performance of combination of spiral trajectories (UD, VD-1, VD-2, DD-1, and DD-2) and k-t sampling patterns (AU, FIX, GA-t, and GA-kt) using L1- SPIRiT reconstruction in 25 datasets (standard error is shown as the error bar). Average root mean square error (RMSE) (a) and structural similarity (SSIM) (b) were compared with the ground truth reference images. The fixed k-t sampling pattern had the largest RMSE and smallest SSIM while other sampling patterns had similar performance. Stars indicated in (b) show the combinations of trajectory and k-t sampling patterns with an SSIM in the highest group of SSIM value as compared to other strategies (P<0.05). Within this group there was no statistical difference between the combinations. The DD-2 trajectory with AU and GA in time temporal sampling patterns had the lowest point estimates of RMSE and the highest point estimates of SSIM.

Figure 2.6 illustrates the representative temporal profile of the LV, RV and myocardium from a retrospective simulation dataset. All 5 trajectories using AU temporal sampling pattern were compared against the ground truth (GT). From the temporal profile, all of the trajectories demonstrate close correspondence with the GT with minimal temporal blurring in the myocardium. There is a minor loss of temporal fidelity at the arrival

of contrast to the RV and LV, but the rest of the upslope and peak closely approximate the fully sampled GT.
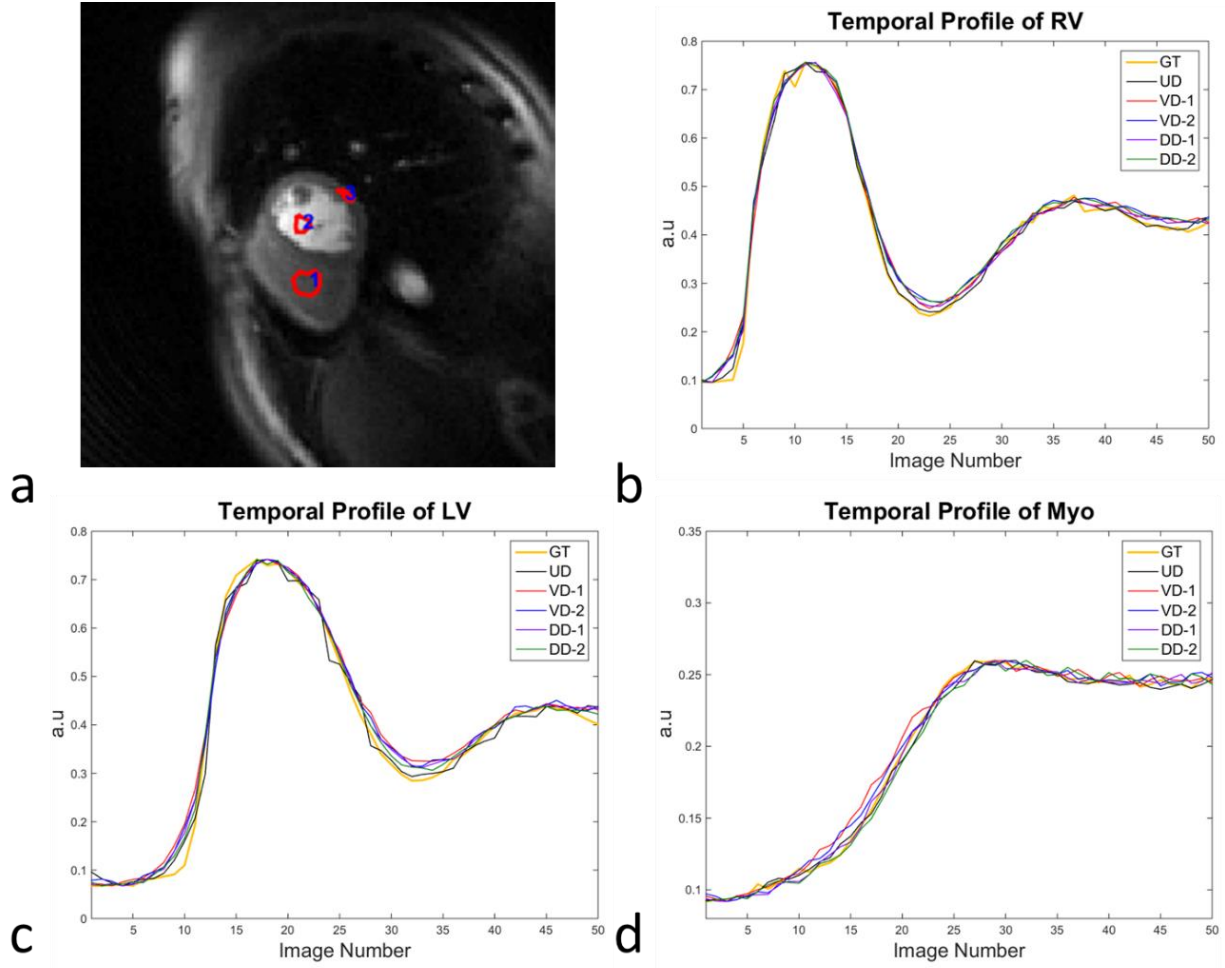
Figure 2.6 Temporal profile of the RV (b), LV (c), and myocardium (d) from one retrospective simulation dataset (a) with five trajectories and AU temporal sampling pattern compared with "ground truth" (GT).

2.3.2 Human Studies

Figure 2.7 shows the direct comparison of the rest perfusion images from the retrospective simulation experiment using DD-2 trajectory with the top two k-t sampling

patterns, AU temporal sampling pattern (a) and GA-t (b), from the same subject in two

gadolinium injections. Both of the two k-t sampling patterns demonstrated good image

quality and minimal image artifacts.
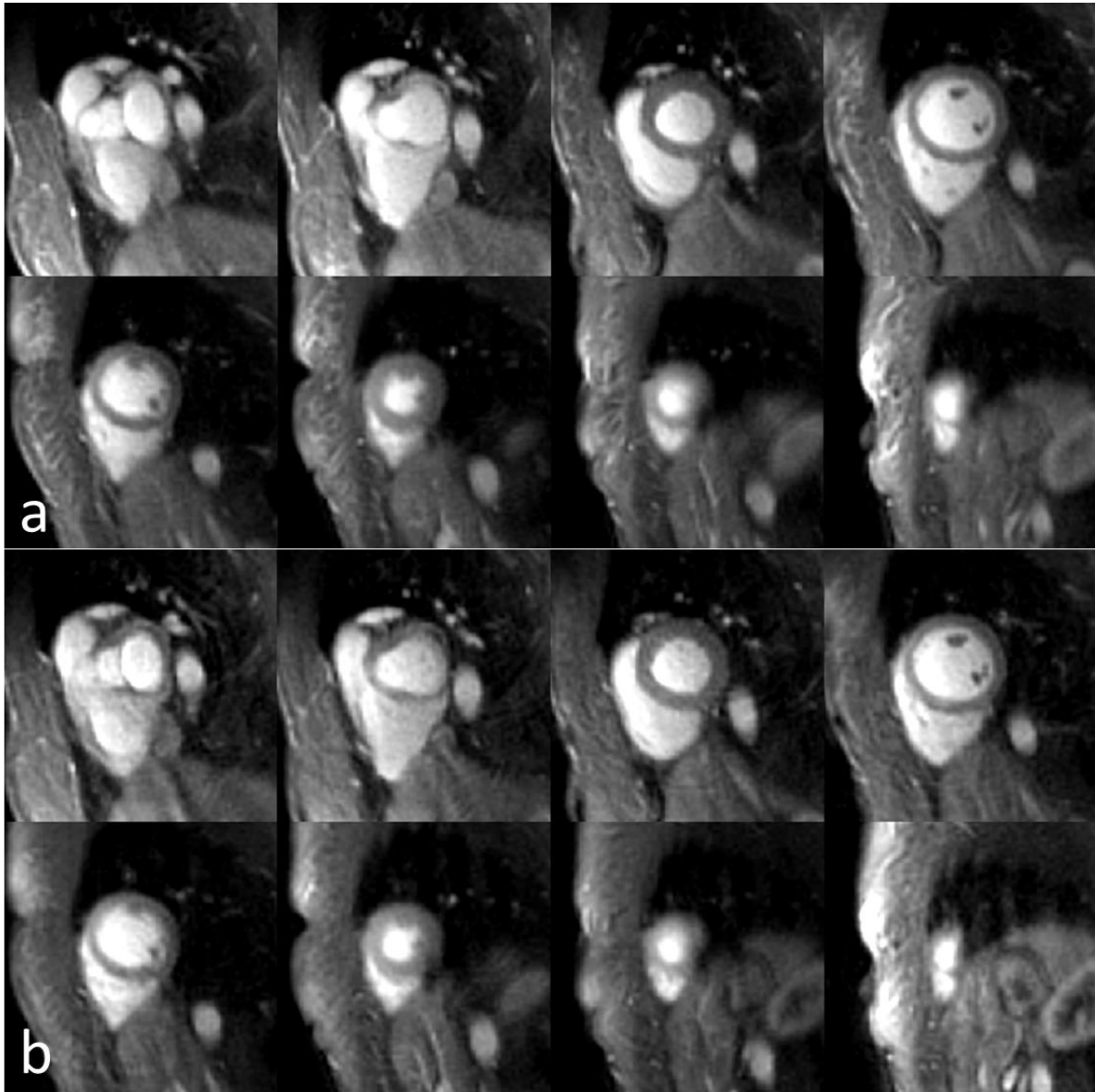
Figure 2.7 Whole-heart coverage resting perfusion images at a middle time frame from the same

volunteer using the DD-2 trajectory with AU temporal sampling pattern (a) and GA in time (b).

Both of the two k-t sampling patterns showed good image quality and minimal artifacts.

Figure 2.8(a) illustrates the image quality of whole-heart coverage first-pass perfusion images at the middle time frame from a healthy volunteer using the DD-2 with AU temporal sampling pattern. The images demonstrate high SNR and image quality with minimal residual aliasing outside the heart regions. Figure 2.8(b) shows the time-intensity curves of the LV cavity from a mid-ventricular slice and the time-intensity curves from each myocardial segment averaged across slices 3-10.
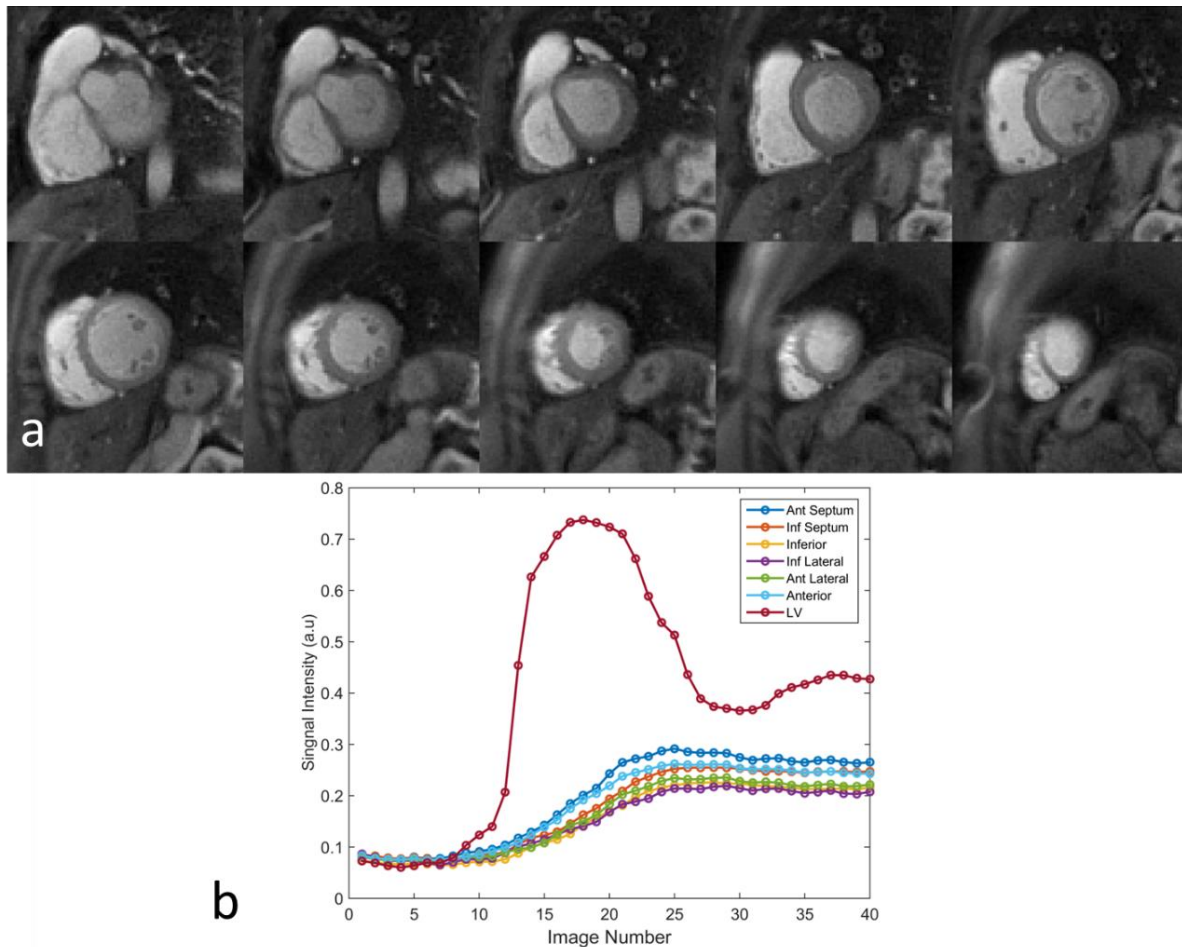
Figure 2.8 Example images demonstrate whole-heart coverage (10 slices) rest perfusion imaging (a) from a clinical study using the DD-2 trajectory and AU temporal sampling pattern. Time

intensity curves from LV cavity of middle ventricular slice and six averaged segments of the myocardium across the whole heart from slice 3 to 10 (b).

2.3.3 Clinical Evaluation

Figure 2.9 shows the whole-heart coverage perfusion images during adenosine stress (a) and at rest (b) from a patient undergoing adenosine stress imaging as part of a clinical research study. There are inducible perfusion abnormalities in left circumflex artery (LCx) and right coronary artery (RCA) territories. There was no evidence of infarction on the late gadolinium enhancement images. At cardiac catheterization, the patient had a high grade stenosis in the LCx (c) and a total occlusion of the RCA (d).
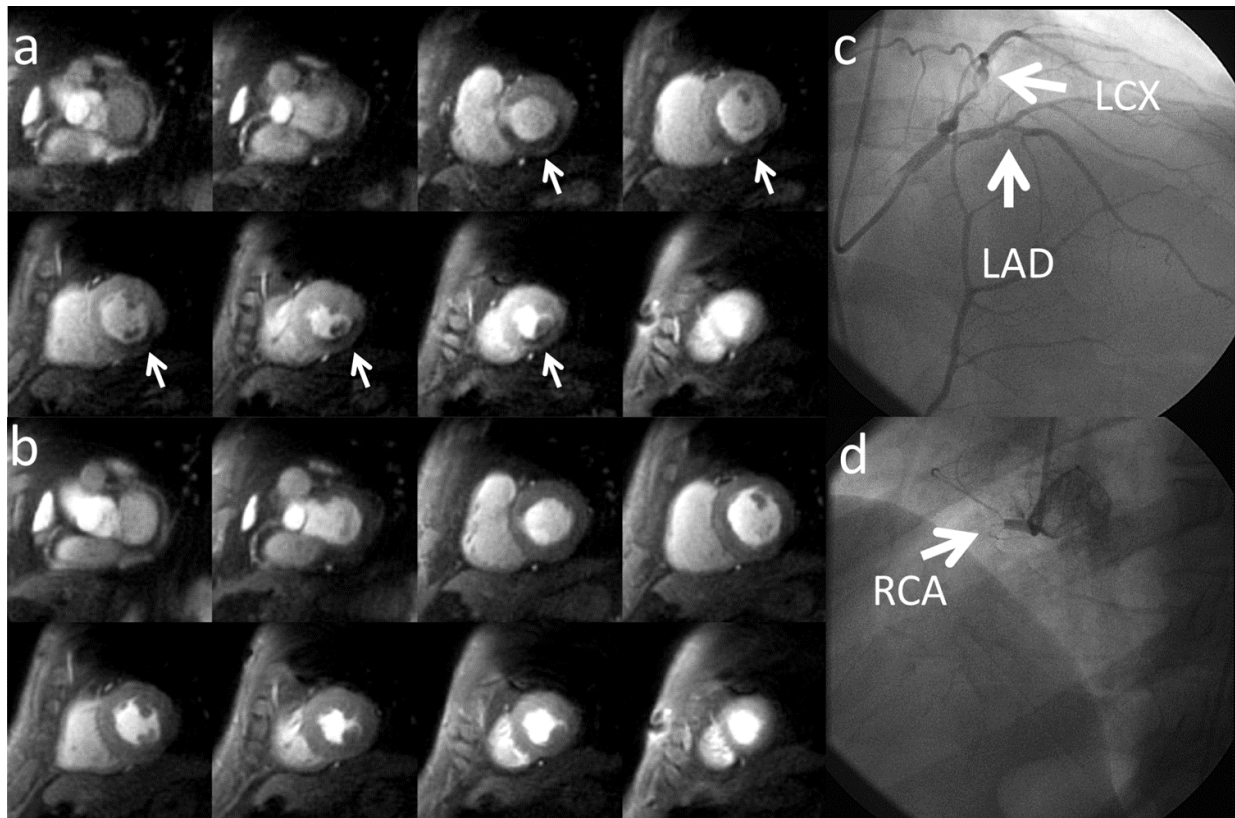
Figure 2.9 Whole-heart perfusion images obtained during adenosine stress (a) and at rest (b) from a suspected CAD patient undergoing adenosine stress imaging as part of a clinical research

study. There are inducible perfusion abnormalities in left circumflex artery (LCx) and right coronary artery (RCA) territories. At cardiac catheterization, the patient had a high grade stenosis in the LCx (c) and an occluded RCA (d).

The average image quality scores (1-excellent, 5-poor) from 16 cases using the AU sampling pattern were 2.18 ± 0.75 and 1.63 ± 0.72 from two cardiologists. There was no statistical difference between the GA-t and AU sampling strategies (p = 0.74 for cardiologist 1 and p = 0.13 for cardiologist 2) showing that either technique works well for the given spiral k-space trajectory.

2.4 Discussion

The goal of this study was to determine the best set of parameters for an interleaved spiral pulse sequence and reconstruction technique for high-resolution whole-heart perfusion imaging which is a prerequisite to a formal clinical evaluation of the technique. Fundamentally, this is a practical design study, and not a full optimization study, given the tremendous flexibility in possible spiral trajectory designs, k-t sampling strategies and reconstruction methods. We demonstrated that accelerated spiral pulse sequences with the combination of PI and CS can achieve high-quality first-pass perfusion images with whole-heart coverage (8 slices) and high in-plane resolution (2mm) at heart rates up to 125 BPM. Conventional clinical cardiac pulse sequences for first-pass perfusion are limited to 3 to 4 noncontiguous slices through the left ventricle. Achieving whole-heart coverage has a number of potential advantages. Firstly, it enables more accurate volumetric quantification of myocardial ischemic burden[86]. This is clinically relevant as studies have demonstrated that patients with a larger ischemic burden are more likely to benefit from revascularization either by cardiac stenting or coronary artery

bypass surgery[8]. Secondly, it eliminates the need for the imaging physician or technologist to carefully plan the appropriate slice locations for the perfusion images. This reduces the time necessary to choose the appropriate slice locations for imaging, and avoids selecting slices that are too apical or basal. Finally, whole-heart coverage ensures that there is no under-sampling of ischemic myocardium in the small number of imaged slices. Recent studies have demonstrated the advantages of 3D coverage[86]. A rapid-multi-slice approach enables higher-in plane spatial resolution and reduces the temporal footprint of the images, reducing cardiac motion-induced artifacts, and represents an alternative strategy for whole-heart coverage which may be more robust to DRA.

We evaluated the effects of spiral trajectory and k-t sampling patterns through simulation and prospective evaluation. We demonstrated that for a spiral reconstruction using L1-SPIRiT with finite-difference in time as the sparsifying transform a dual-density trajectory with a broad transition region (DD-2) provides a good balance between adequately sampling the low spatial frequencies and providing a spatially incoherent aliasing pattern while capturing sufficient energy in k-space to avoid high energy, low-frequency aliasing artifacts. The simulation used the same image datasets down-sampled onto the candidate k-space trajectories to directly compare the effects of k-space trajectory and k-t sampling pattern. Contrary to our original hypothesis, both AU and GA-t trajectories resulted in similar image quality, at least for the DD-2 trajectory and the L1-SPIRiT with finite-difference in time reconstruction.

Choosing a spiral trajectory for a combined PI and CS reconstruction requires trade-offs between factors which could affect each type of reconstruction differently. For CS based techniques a relatively incoherent sampling pattern is a necessity and

adequate sampling of the low spatial frequency reduces high-energy low-frequency aliasing and generally improves image reconstruction as compared to completely random under-sampling strategies. We demonstrate through simulation and imaging experiments that DD-2, which is a dual density spiral with a broad transition, appears to provide a reasonable trade-off for a reconstruction utilizing both PI and CS.

Regarding the k-t sampling pattern, a fixed temporal pattern which is adequate for PI does not work well for an L1-SPIRiT reconstruction as it is completely coherent in the temporal domain. However, for the evaluated spiral pulse sequences, reconstruction performance between the AU, GA-t and GA-kt temporal sampling strategies was similar. The lack of difference between GA-t and GA-kt could be related to the spiral design which has 3 spiral arms that are spaced 120° apart from each other which is very close to the golden angle 111.25°. We found that the L1-SPIRiT reconstruction performance is more dependent on the particular spiral k-space trajectory pattern rather than the k-t sampling pattern. The prospective study which directly compared AU and GA-t strategies for the DD-2 trajectory in the same subjects confirmed this assertion, resulting in similar image reconstruction performance for both k-t sampling strategies.

Strictly speaking, the conclusions regarding the choice of trajectory and temporal sampling pattern apply to the L1-SPIRiT reconstruction using temporal finite difference as the sparsifying transform. We chose to use temporal finite difference as it is generally robust and errors from respiratory motion typically only affect a small temporal extent of the data series. To assess generalizability of the results we have also performed a preliminary analysis using kt-SLR[66] with only a temporal TV term (i.e. no spatial TV). The results with respect to the choice of k-space trajectory were similar to what we reported

for L1-SPIRiT in this manuscript and images were of similar quality. With respect to temporal sampling strategy, the results for golden-angle-in-time were superior to those using the angularly uniform temporal strategy as expected.

Preservation of the temporal dynamics of the perfusion image data is essential for quantification of myocardial perfusion. Reconstruction techniques that rely on the k-t correlation of the data have the potential for affecting the fidelity of the temporal information. We show in simulation and retrospective down-sampling studies that although we are using a finite-difference in time as sparsifying transform, the temporal dynamics are preserved in the myocardium for the L1-SPIRiT based reconstruction. There is a minor loss of temporal fidelity at the time of contrast arrival at the RV and LV cavity which is due to the very high temporal-frequency content when the contrast first appears in the cavities.

This study has a few limitations. In the retrospective analysis, we utilized SSIM and RMSE as quantitative metrics for assessing image reconstruction performance. However, these parameters may not be sensitive to subtle changes in temporal dynamics and do not directly address performance for clinical detection of CAD. We chose the minimal regularization parameter for the L1 term which adequately removed aliasing to minimize losses in temporal fidelity. For 2D spiral perfusion imaging, where the SNR is limited due to heart rate constraints, non-Cartesian PI techniques work well at 2-3x acceleration factors, but perform poorly at higher acceleration factors[80]. For perfusion studies which only acquire 3-4 slices per heart-beat, non-Cartesian PI alone at 2x acceleration may be preferable since each image is reconstructed separately and is thus robust to respiratory motion and the reconstruction does not suffer from any temporal blurring[81]. For more

highly accelerated techniques required to achieve 2D whole heart coverage, we have found that reconstruction techniques which exploit prior knowledge are necessary. We did not perform a formal comparison between different reconstruction techniques which is a limitation of this paper. As most of the prospective studies were acquired during a routine clinical examination, we were only able to obtain resting perfusion images with a single pulse sequence precluding the direct comparison of spiral and Cartesian pulse sequences in the same subject. However, it does provide a real-world evaluation of the performance of the accelerated-spiral approach in patients with CAD. Resting perfusion images demonstrate both feasibility of the technique and high image quality. The example case from our ongoing study of whole-heart spiral perfusion provides preliminary evidence of the utility of the proposed pulse sequence for detecting obstructive CAD with an inducible perfusion defect matching the location of obstructive CAD by cardiac catheterization. An additional limitation is that similar to other techniques that rely on correlations in k-t space, the L1-SPIRiT reconstruction is affected by respiratory motion, and severe respiratory motion degrades image quality. We chose finite-difference in time for the L1 term, as respiratory motion artifacts which usually occur near the end of the breath-hold, tend to be localized to only this portion of the data acquisition. We have recently demonstrated a technique based on rigid-registration of the heart region[87] which improved robustness to motion. Ongoing efforts by our group and others have developed reconstruction techniques which utilize registration techniques to overcome this limitation with promising initial results.[67,88] Further clinical studies and direct comparison to existing techniques will be necessary to demonstrate the potential utility of whole-heart coverage spiral pulse sequences for this challenging application.

2.5 Conclusion

We demonstrate the successful application of whole-heart coverage first-pass myocardial perfusion imaging using accelerated spirals with optimized trajectories and k-t sampling patterns. With this technique we can acquire 8 short axis slices using a spiral trajectory designed with a nominal in-plane resolution of 2 mm at heart rates up to 125 BPM. Future clinical validation studies in patients with known CAD at rest and adenosine stress will be essential to further assess and optimize performance of these sequences.

Chapter 3: Reduced FOV single-shot spiral perfusion

3.1 Introduction

The Nyquist sampling theorem requires a k-space sampling finer than $\Delta k = 1/FOV$ to support the desired FOV without spatial aliasing artifacts. For CMR imaging this typically means that a FOV larger than the patient's chest must be imaged to avoid aliasing artifacts. However, if the region of interest (ROI) only occupies a small region of the FOV, this strategy is inefficient. Conventional contrast-enhanced first-pass perfusion studies typically use a FOV of 300-400 mm depending on the patient's body size. However, the heart is easily encompassed by a FOV of 80-120 mm in the short-axis view. By using a reduced or restricted FOV (rFOV) imaging technique, k-space can be sampled more coarsely resulting in improved sampling efficiency. The rFOV can be achieved using outer volume suppression (OVS) techniques[89]. Usually OVS techniques employ a spatial preparation sequence to saturate the signal outside the. Modern MRI scanners oversample k-space and employ anti-aliasing filter in the readout direction, therefore OVS only needs to be applied in the phase-encoding direction. Multiple studies[90-93] have shown the successful applications by utilizing OVS to achieve high efficiency and rapid imaging. For spiral imaging, where the readout direction is continually changing, a traditional anti-aliasing filter cannot be utilized and the full extent of the object must be supported in all directions. Multiple regional saturations would need to be applied in multiple directions to support the circular FOV. This strategy would be challenging for myocardial perfusion

imaging where only a short period of time is available for the application of such saturation pulses. Furthermore it would require placement of the different saturation pulses which would be time consuming for the MRI technician. Thus, for spiral imaging, a circular rFOV design would be advantageous.

Myocardial perfusion imaging requires rapid data acquisition. Typically this is achieved using rapid FLASH[94], EPI[95], or SSFP[96] readouts following a saturation recovery preparation. These readout strategies, when combined with Cartesian or radial sampling, require multiple RF excitations to acquire the data needed for each perfusion image. In the case of FLASH acquisition, this requires a short TR, which necessitates the use of relatively low flip angles. Spiral trajectories have the potential to acquire a complete image with a single RF excitation. This single excitation approach provides very high temporal resolution and sampling efficiency, but also requires highly accelerated spiral trajectories with an associated SNR penalty. We propose that incorporating OVS pre-saturation with single-shot excitation spiral imaging can reduce the acceleration rates necessary, thus balancing the SNR loss and providing robust perfusion imaging. The goal of this study is to develop an OVS design suitable for a single-shot rFOV spiral perfusion sequence. The resulting sequence will be used to achieve whole heart coverage with high spatiotemporal resolution with comparison with standard full FOV spiral perfusion images in clinical patients.

3.2 Methods

3.2.1 Designed Consideration

We have previously shown that first-pass myocardial perfusion imaging using accelerated spirals with an optimized trajectory and k-t sampling pattern can produce high quality 2D perfusion images with whole-heart coverage at the heart rates up to 125 BPM[57]. This technique uses multiple spiral interleaves with effective acceleration factor of 5 to achieve whole heart coverage with 8 slices and in-plane resolution of 2 mm by supporting 340 mm² FOV. The temporal resolution of each perfusion image is 35 ms. We propose that the delay time between saturation and imaging can be used to add OVS preparation to increase the k-space sampling efficiency. The reduction in the required FOV can be used to support the same in-plane resolution as a full FOV sequence with a single-shot excitation spiral readout, greatly improving the temporal resolution.

3.2.2 Single-shot Excitation and SNR Consideration

The balance between spatial resolution, temporal resolution, and SNR can be expressed as follows:

$$SNR \propto \eta * \delta_{xyz} * \sqrt{T_{total}} * f(\rho, T_1, T_2) \qquad (3.1)$$

where η is the SNR efficiency of variable-density spiral trajectory, δ_{xyz} is the spatial resolution, T_{total} is the total readout time for specific slice and $f(\rho, T_1, T_2)$ is the pulse sequence dependent function to determine the signal amplitude at readout. If the spatial resolution is maintained the same for both multi-shot spirals and single-shot spiral, the single-shot will have lower SNR due to the shorter readout time. However, a higher 90°

flip angle (FA) could be used to compensate for the loss of SNR because longitudinal magnetization does not need to be preserved for additional RF excitations and readouts. For example, in the optimized multi-shot spirals technique, 3 spirals with each with a 5 ms readout duration (15ms total readout duration)and 31º FA is used to exactly balances the loss in magnetization from each RF pulse[13]. The reduction in SNR from a single-shot excitation spiral with an 8 ms readout $\sqrt{8}/\sqrt{15}$) is offset by the larger 90º FA (sin(90º)/sin(31º)), resulting in a relative SNR increase of 42% increase as compared to the multi-shot spirals. The use of variable-density trajectories results in lower SNR in images given the same spatial resolution and scan time[97]. Highly accelerated single-shot spiral (12x Nyq) is required to achieve 2 mm in-plane resolution for FOV of 340 mm^2, which will result in 20% SNR loss and unstable for the reconstruction pipeline using combination of compressed sensing and parallel imaging technique. In addition, the temporal resolution is shortened by 77.2% (8 ms versus 35 ms).

3.2.3 rFOV Design

A rapid, B1-robust 2D OVS technique[92] is implemented to enable imaging of a reduced FOV that only includes the heart. The OVS preparation (Fig. 3.1a) consists of a non-selective tip-down, followed by spatially selective tip-back and a spoiler. A 4 ms adiabatic BIR-4[98] tip-down pulse is used for non-selective excitation, and a 2.2 ms jinc-shaped 2D spiral spatial selective[99] pulse with a time-bandwidth product of 4 is used to tip back spins within a 100 mm cylindrical rFOV. A 2 ms spoiler gradient is used to dephase residual transverse magnetization. The spatial profile of the 2D spiral tip-back pulse is shown in Figure 3.1b and 3.1c. For the rFOV = 100 mm design, the stopband is

around ±400 mm, which is large enough to suppress the signals outside of the heart to prevent spatial aliasing.
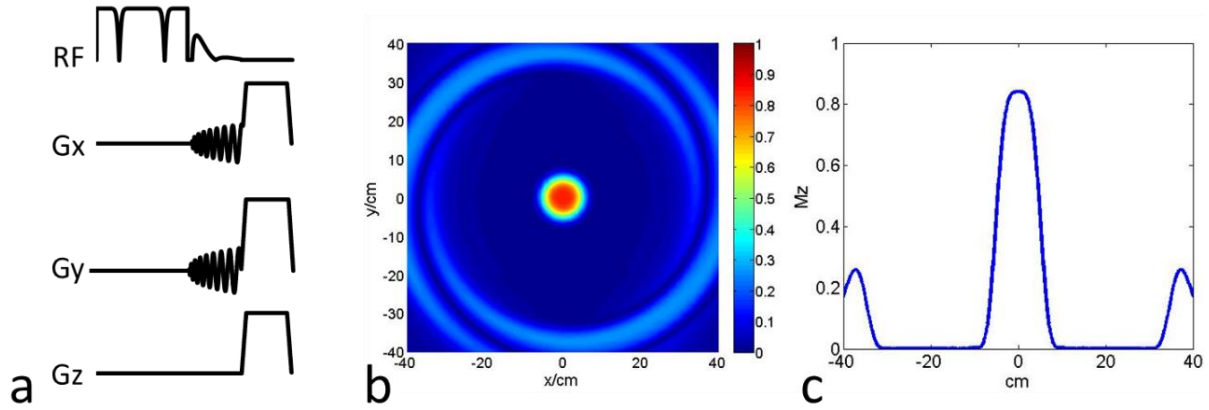
Figure 3.1 a: Diagram of the 2D OVS pulse sequence, which is consisted of a non-selective adiabatic BIR-4 tip-down pulse, 2D spiral spatial selective tip-back pulse and the spoiler to crush the residual signal. b: 2D spatial profile of the rFOV = 100 mm design. c: 1D spatial profile cross the 2D profile center to show the stopband is around ±400 mm.

Figure 3.2 shows the simulated performance of the OVS module across the B1 scale factors (a) and resonance frequency offsets (b). The OVS pulse is insensitive to the off-resonance effect due to adiabatic excitation and short tip-back spiral pulse. However, the OVS performance is poorer with lower B1 scale factors, reaching 75% efficiency at a B1 scale factor of 0.6.
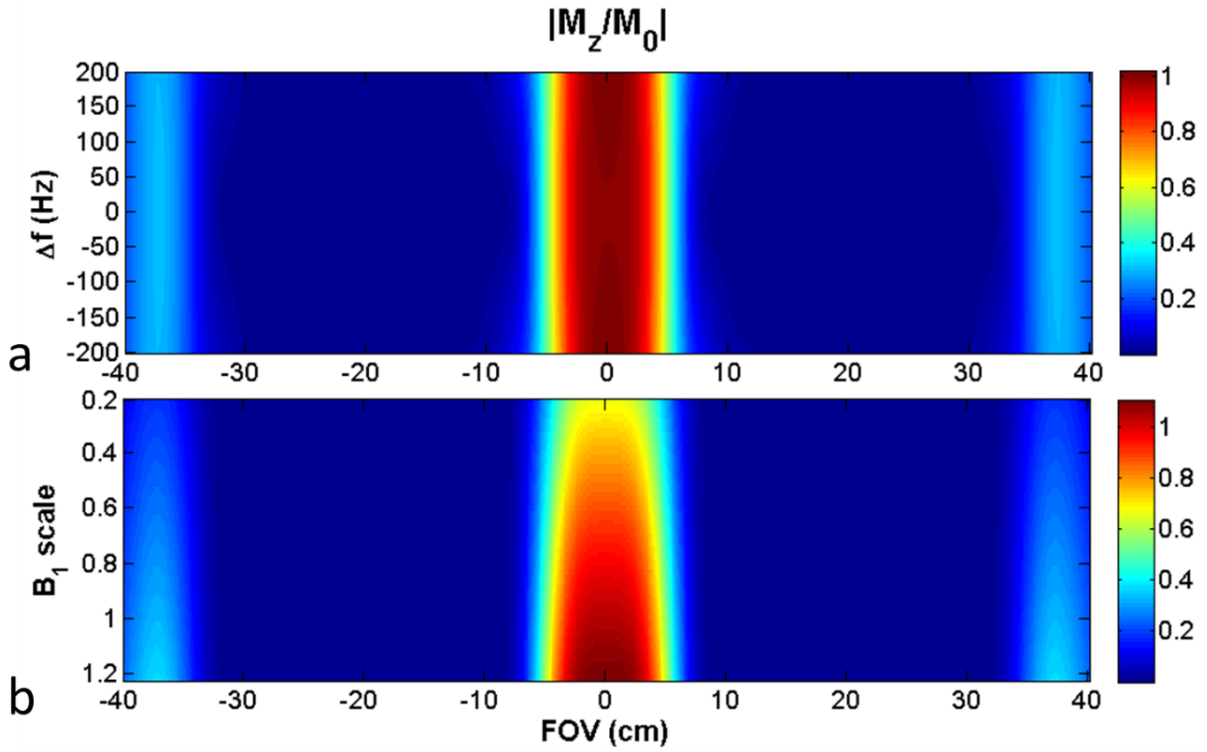
Figure 3.2 Simulated performance of the OVS by varying the B1 scale (a) and off resonance (b)

3.2.4 Pulse Sequence Design

The pulse sequence is shown schematically in Figure 3.3a. Non-selective saturation with an adiabatic BIR-4 pulse is applied for T_1-weighted preparation. A spectrally selective fat-saturation (SPAIR) pulse is used to achieve fat suppression, followed by the OVS module to suppress signals from outside the heart. Single-shot excitation spiral readouts are acquired in an interleaved order for 2 different slice locations separately to produce T_1-weighted images for perfusion. Therefore, 2 slices are acquired in one SR block, and SR blocks are repeated until all the slices are imaged. The single-shot spiral trajectory is presented in Figure 3.3b. It is an 8 ms spiral using a Fermi-shape dual density design, with 20% center fully sampled and a broad transition to reach the ending density of 0.15x Nyquist, achieve 2mm resolution at a reduced FOV of 170 mm.

The corresponding point spread function (PSF) is shown in Figure 3.3c, and this spiral trajectory has relative incoherent and a noise-like side lobe distribution well suited to CS reconstruction. The spiral is rotated by a golden angle (111.25⁰) in time to further provide incoherence in the temporal domain.
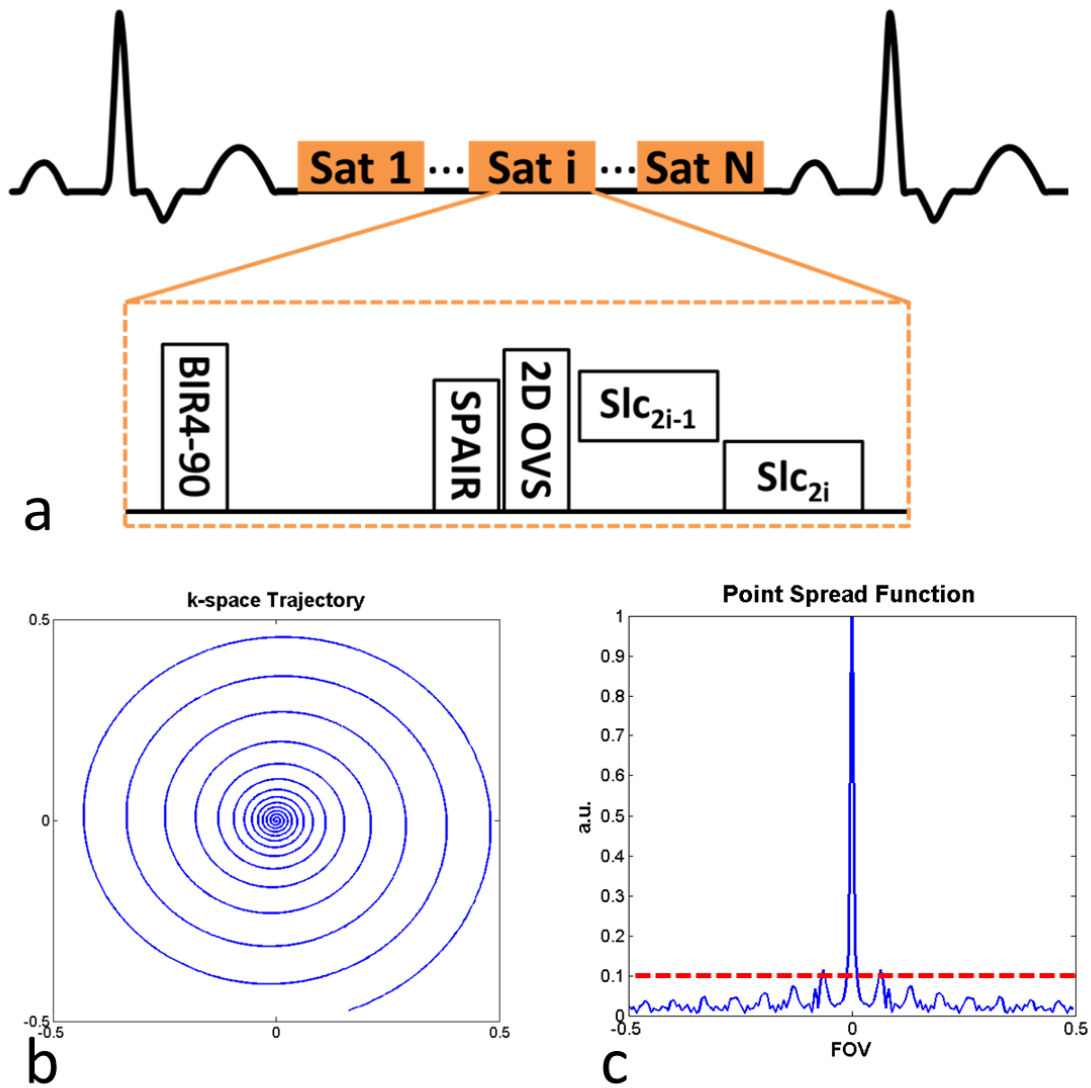
Figure 3.3 (a) Schematic of the single-shot spiral perfusion with 2D OVS pulse sequence. (b) k-space trajectory of the single-shot spiral with Fermi-shape dual density design and (c) corresponding point spread function to show the incoherent sampling pattern.

57

3.2.5 Image Reconstruction

Block low-rank sparsity with motion-guidance (BLOSM)[67] combined with SENSE[52] was implemented to reconstruct the under-sampled perfusion images through optimization of:

$$minimize_{\mathbf{m},\mathcal{R}} \ \|\Phi_{\mathcal{R}}\mathbf{m}\|_{p*}$$

$$\text{s.t.} \ \|\mathcal{F}_u\mathbf{Sm} - \mathbf{d}\|_2 < \mathcal{E} \qquad\qquad (\ 3.2\ )$$

where $\mathbf{m}$ represents the estimated perfusion images, $\mathbf{d}$ is the acquired undersampled k-space data, and $\mathcal{F}_u$ is the undersampled non-uniform Fourier transform, which only takes values at the k-space positions where $\mathbf{d}$ are acquired. $\mathbf{S}$ is coil sensitivity map. $\Phi_{\mathcal{R}}$ represents the operator for block tracking and creation of rearranged clusters, after $\mathbf{m}$ is divided into blocks which are tracked using displacement maps $\mathcal{R}$. $\|*\|_{p*}$ is a joint Schatten p-norm that exploits the regional low rank property. An iterative soft-thresholding (IST) algorithm[100] was adopted to solve this optimization problem. The image reconstruction was implemented in MATLAB (R2013b, the MathWorks, Natick, MA).

3.2.6 Human Studies

To compare the performance of the full FOV and rFOV perfusion sequence, resting first-pass perfusion was performed in 16 subjects (8 for each sequence) undergoing clinically ordered CMR studies. Written informed consent was obtained from all subjects, and imaging studies were performed under institutional review board (IRB) approved protocols. Imaging was performed on a 1.5T MRI scanner (MAGNETOM Avanto, Siemens Medical Solutions, Erlangen, Germany). Perfusion imaging was performed

using 0.075mmol/kg Gd-DTPA (Bayer AG, Leverkusen, Germany) injected intravenously at a rate of 4mL/s followed by 25 mL of saline flush at 4mL/s. A 32-channel cardiac phased-array receiver coil (Invivo Corporation, Best, The Netherlands) was used for signal reception. Imaging protocols for the full FOV and rFOV sequence were shown in Table 3.1. Common sequence parameters included: echo time (TE) 1.0 ms, repetition time (TR) 9 ms, saturation recovery time (SRT) 80 ms, FA 90⁰, temporal resolution 8ms each slice, 2 slices per saturation, and 8 slices covering the whole left ventricle.

Table 3. 1 Sequence parameters for full FOV and rFOV sequence.

	Full FOV	rFOV
FOV (mm)	340	170
Resolution (mm)	2.01	2.01
Starting density	1.2	1.2
Ending density	0.08	0.15
Fully sample k-space center	20%	20%
Sample size	8	8

3.2.7 Image Analysis

Perfusion images were reconstructed by proposed BLOSM algorithm. Image quality was graded on a 5-point scale (1-excellent, 5-poor) independently by two experienced cardiologists blinded to acquisition method. Statistical analysis on image scores from the two reviewers were analyzed using the Wilcoxon signed rank tests. Image quality of the full FOV and rFOV sequence was analyzed using the Mann-Whitney U test.

3.3 Results

Figure 3.4 shows a phantom experiment of OVS performance. A full FOV image is shown in Fig. 3.4a, and the rFOV used for b and c is indicated with a yellow box. Direct reduction of the FOV (Fig. 3.4b) results in spatial aliasing, which is suppressed with application of OVS preparation (Fig. 3.4c).
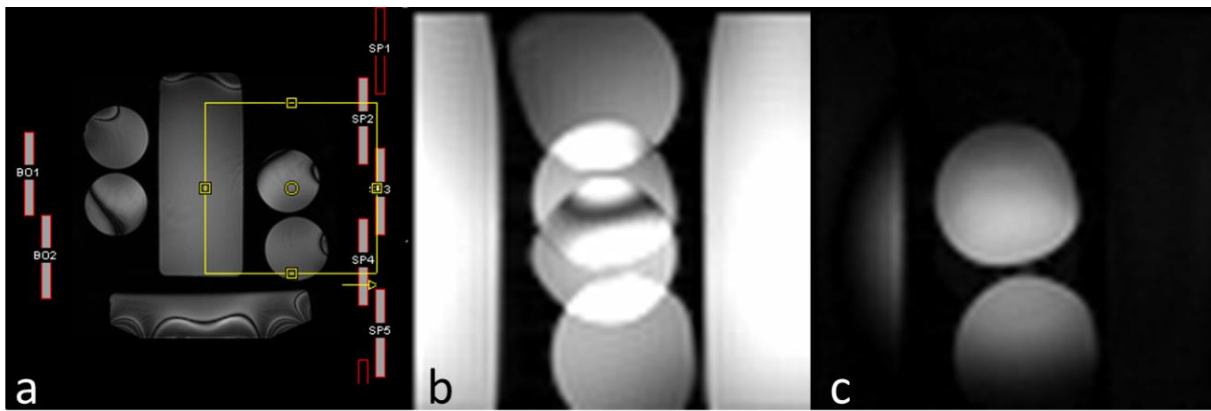
Figure 3.4 A phantom experiment setup is shown with a full FOV with a reduced FOV indicated with a yellow box. Reduced FOV images are shown without (b) and with (c) OVS preparation

Figure 3.5 shows direct reconstruction with zero padding (dc/zp) (a) and BLOSM (c) images from 12x accelerated spiral with FOV 340 mm without OVS and dc/zp (b) and BLOSM (d) from 6x accelerated spiral with rFOV 170 mm. The images in (b) and (d) were shown in the FOV 340 to present the OVS performance. The OVS performed well by limiting signal to the heart region. Without OVS, the aliasing was not completely removed due to the very high accelerated factor needed to support a full FOV.
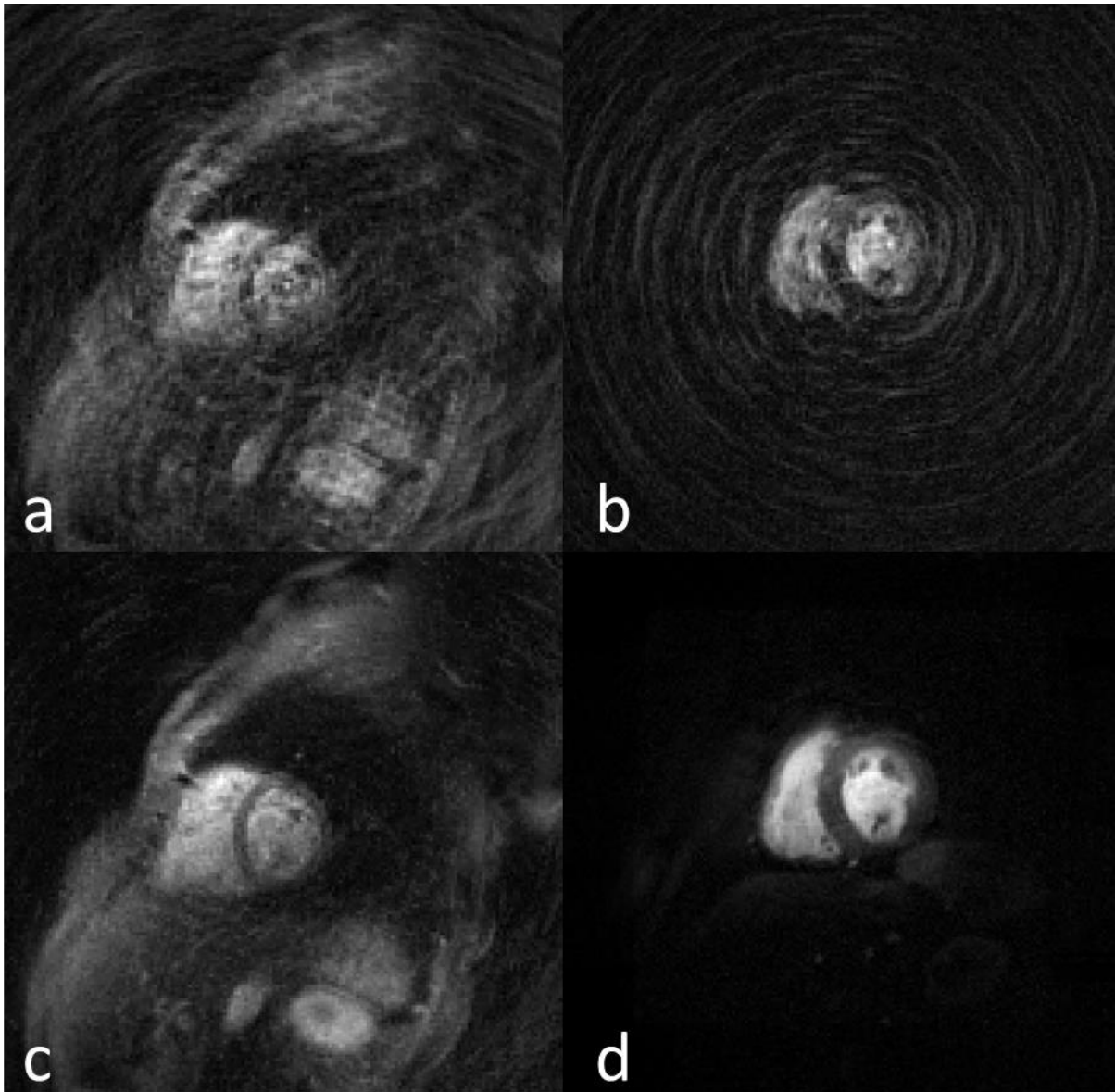
Figure 3.5 Full FOV of 340mm without OVS (a,c) and rFOV of 170mm with OVS (b,d) shown in 340 mm FOV perfusion images. Top row shows the directly gridding images with zero padding from the under-sampled data. Bottom row shows the BLOSM reconstructed images.

Figure 3.6 illustrates the image quality of whole-heart coverage first-pass perfusion images at the middle time frame from a subject using rFOV of 170 mm. The images

demonstrate high SNR and image quality with minimal residual aliasing outside the heart regions.
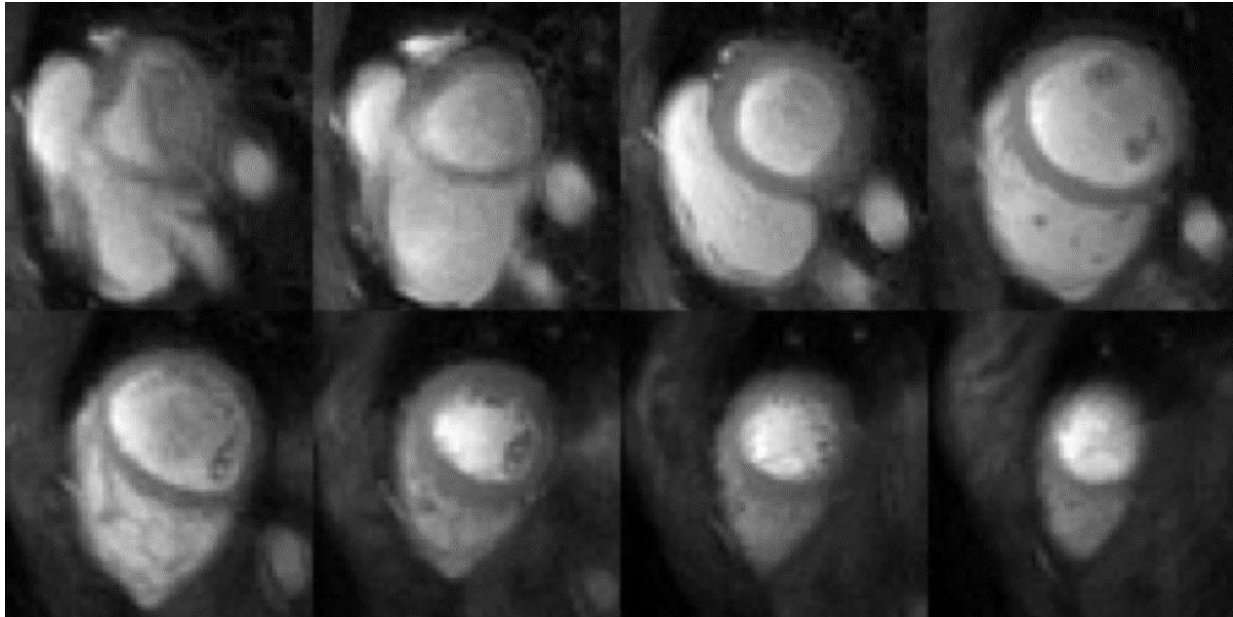
Figure 3.6 Example images demonstrate whole-heart coverage rest perfusion imaging from a clinical subject using rFOV of 170 mm.

Figure 3.7 shows rFOV single-shot spiral perfusion images covering the whole heart from a patient with known CAD. A subendocardial perfusion defect in the anterior and lateral walls corresponded to a region of focal scarring on LGE images. Given the temporal footprint of 8 ms, fine details of the cardiac trabeculations and papillary muscles are evident which are typically not well visualized due to temporal blurring with other perfusion techniques.
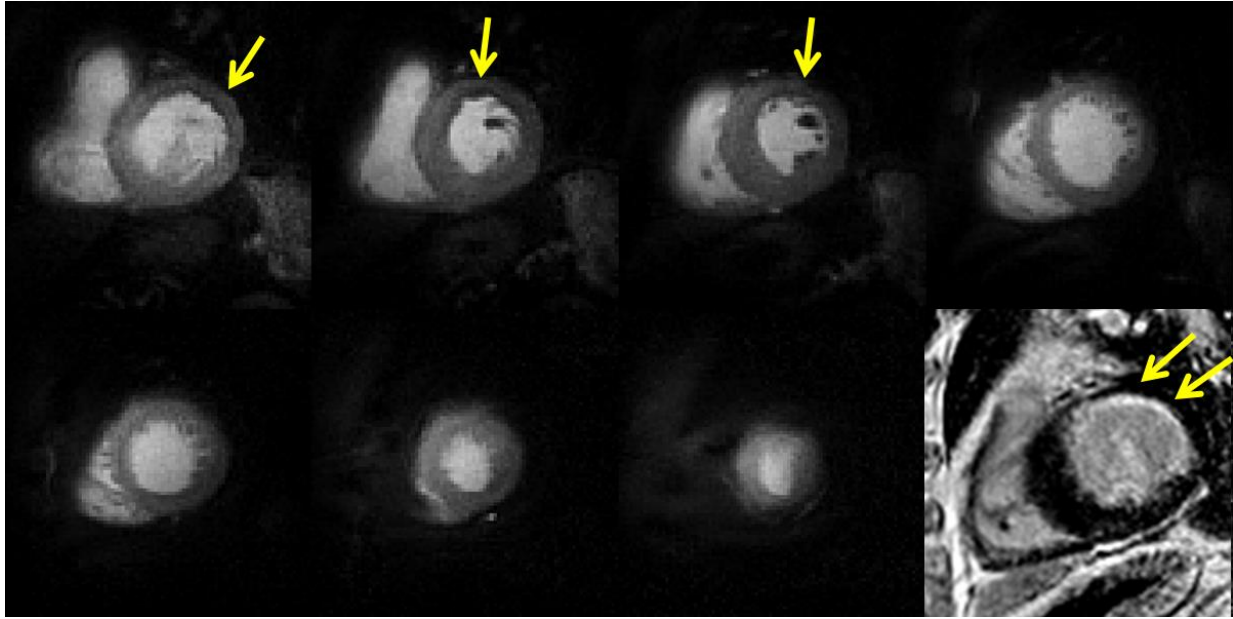
Figure 3.7 rFOV(170mm) single-shot perfusion and positive LGE images of a CAD patient

Average image quality scores (1-excellent, 5-poor) from full FOV cases (N =8) and rFOV cases (N = 8) were 3.1 ± 0.64 and 2.3 ± 0.46 (p = 0.02) from cardiologist 1, and 2.5 ± 0.54 and 1.8 ± 0.47 (p = 0.04) from cardiologist 2. Both of the two cardiologists favor the rFOV image quality compared to the full FOV images.

Table 3. 2 Image quality graded by two cardiologists (1-excellent; 5-poor)

	Full FOV (N=8)	rFOV (N=8)
Cardiologist 1	3.1 ± 0.64	2.3 ± 0.46*
Cardiologist 2	2.5 ± 0.54	1.8 ± 0.47*

* p < 0.05

3.4 Discussion

In this study, reduced FOV spiral perfusion imaging is achieved by fast 2D OVS preparation. Instead of supporting the full FOV, the rFOV covering the ROI can either

63

greatly shorten the scan time or increase the spatial-temporal resolution using the same amount of scan time. It provides more flexible image planning for technicians compared to utilizing conventional multiple saturation bands. The rFOV performance is dominated by the OVS module. In our design, the adiabatic BIR4 pulse was used to tip-down all spins first and the 2D spiral pulse was applied to tip-back the spins within the ROI. Based on the B_0 and B_1 inhomogeneity simulation, the OVS module was not sensitive to the B_0 due to the short duration of the pulse. However, it was sensitive to the B_1 inhomogeneity. This design will result in good OVS performance outside the ROI, but within the ROI, the tip-back performance is B_1 dependent and it will cause signal loss if the B_1 is extremely low. Potential solution is using the hard pulse to tip-down the spins instead of using adiabatic pulse, but it cannot guarantee good OVS performance outside the ROI. The application is not limited to perfusion imaging, the rFOV can be transferred to other applications when the imaging ROI is much smaller than the object size such as liver or kidney imaging.

The single-shot excitation leverages the perfusion imaging into a new stage where the imaging speed is ultra-fast, even less than 10 ms per slice. Among the most three popular trajectories, Cartesian, radial and spiral, the single-shot excitation is the unique only for spiral trajectory. It provides the possibility to do the whole heart coverage systolic perfusion imaging or continuous acquisition imaging with whole heart coverage. Systolic data acquisition is likely to be more robust in patients with atrial fibrillation, the most common cardiac arrhythmia, with a prevalence of 9% in elderly people (>65 years) with cardiovascular disease[101]. In addition, the myocardium is much thicker at the systole than at diastole. Meanwhile, with the ultrafast acquisition, it also becomes feasible to perform

the exercise stress test imaging with high spatial resolution and whole heart coverage. Usually during the exercise stress, maximum predicted heart rate is estimated to be 220 minus age[102] BPM, which means the corresponding R-R interval is at the range of 300 to 400 ms. It will be great challenge for conventional whole heart coverage first-pass perfusion sequence. However, in our design, if 4 slices with rFOV using single-shot excitation are acquired in one SR preparation, to achieve the whole heart coverage of 8 slices, it only takes total time of 240 ms, which can support any heart rate in the exercise stress imaging.

The SNR loss of the single-shot excitation due to the shorter readout time is balanced back by utilizing larger flip angle. This allows us to achieve the ultra-high temporal resolution without scarifying the original image SNR, resulting similar image quality with multi-shots spirals. However, the relative longer spiral per arm (8 ms single-shot vs 5 ms multiple-shots) will potentially suffer from the off-resonance artifact. Therefore, automatic off-resonance correction methods[50] are extremely helpful for the single-shot excitation pulses.

Two slices perfusion images were acquired after the OVS module within one SR preparation in this study. The first slice was sampled immediately after the OVS which would get signal totally nulled outside the ROI. However, the second slice was acquired 10 ms after the OVS module and the magnetization outside the ROI would recover by $M_0(1 - e^{-\frac{10}{T_1}})$, for that fat or small T_1 value tissue, the recovery could be over 5% of the total magnetization. Example images of the different OVS performance is shown in Figure 3.8. The basal slices were sampled immediately after the OVS which resulted in perfect

nulling. However, the apical slices were acquired later where the signal outside the heart were recovering. Potential solution of this problem is to tune the tip-down and tip-back pulse to be greater than 90°. By doing this, there is no effect of the spin within the ROI, however, for the spins outside the ROI, the initial magnetization after the OVS is a little bit negative, the FA of the tip-down and tip-back pulse can be chosen as the zero-across point in the recovery curve to achieve similar OVS performance for both of the slices.
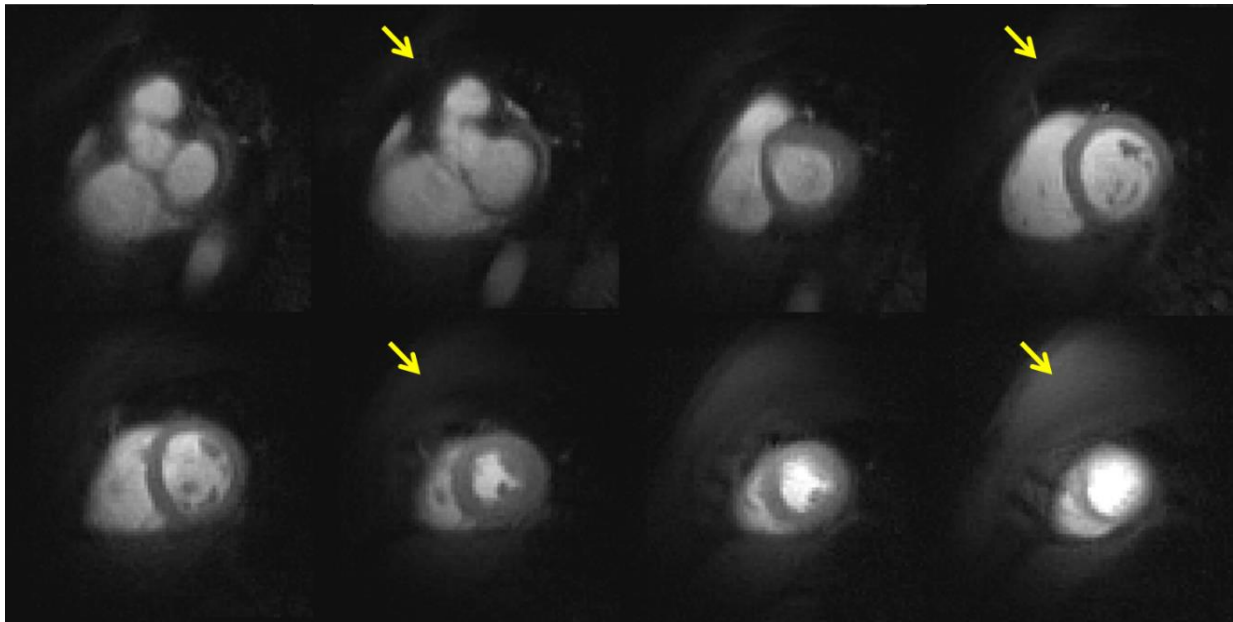
Figure 3.8 Example perfusion images of rFOV to show the different OVS performance of two slices acquired in one SR preparation. Top row images are sampled immediately after the OVS, and bottom row images are acquired after 10 ms of OVS.

This study has some limitations. As most of the prospective studies were acquired during a routine clinical examination, we were only able to obtain resting perfusion images with a single pulse sequence precluding the direct comparison of full FOV and rFOV pulse sequences in the same subject. However, it does provide a real-world evaluation of the performance of the accelerated-spiral approach in patients with suspect CAD. Resting

perfusion images demonstrate both feasibility of the technique and high image quality. We did not compare different CS reconstruction methods, but BLSOM has already qualitatively proved to be a robust motion compensated CS method. The OVS design can be further optimized to achieve similar rFOV performance for different slice locations.

3.5 Conclusion

In this chapter, we proposed and validated a 2D OVS sequence module and incorporate it into a single-shot excitation spiral perfusion sequence with reduced FOV. This enabled less aggressive acceleration with very high temporal resolution (8 ms per slice) that supported the high heart rates found during in exercise stress cases. Future clinical validation studies in patients with known CAD at rest and adenosine stress will be essential to further assess and optimize performance of these sequences.

Chapter 4: Quantitative spiral perfusion

4.1 Introduction

Qualitative stress myocardial perfusion imaging using CMR has been demonstrated robust diagnostic and prognostic performance in multiple studies[103,104]. High resolution quantification of myocardial blood flow (MBF) with whole heart coverage has the potential to provide unique information to improve the diagnosis of 3 vessel disease and microvascular disease in comparison to simple qualitative evaluation[105-107]. A direct comparison of quantitative versus qualitative CMR perfusion was conducted by Patel et al in patients with suspected myocardial ischemia using QCA as the comparative standard[44]. Although overall there was no significant difference in accuracy for the diagnosis of CAD, the quantitative method differentiated single vessel disease from multi-vessel disease which has important implications for assessment of prognosis and therapeutic decision making.

To perform quantification of myocardial perfusion, an accurate measurement of the arterial input function (AIF) is needed. The AIF can be derived from the signal intensity-time curve in the left ventricular (LV) cavity. However, specific measures need to be taken to accurately derive the contrast agent concentration from the signal intensity data. Possible solutions to avoid arterial signal saturation include: 1) use lower contrast agent dosage; 2) dual-bolus approach, which involves determining the AIF from a low concentration pre- bolus[108] and 3) dual-contrast sequence, which involves determining the AIF from a low-T1 weighted image during the single-high contrast bolus[109,110]. Usually,

utilizing lower contrast dosage method resulted in lower SNR and CNR perfusion images. Dual-bolus and dual-contrast sequences are the most widely used methods to characterize the MBF.

The dual-bolus method allows the use of high concentrations of contrast for myocardial tissue analysis, but a lower concentration bolus to maintain the linearity of the LV signal intensity[10]. This method has been validated in an animal model against microsphere blood flow, and has shown good correlations across a range of low, normal, and hyperemic MBF[108]. In order to scale the data from the low-dose AIF acquisition to the high-dose myocardial acquisition, the AIF time intensity curves is multiplied by the ratio of the contrast agent concentrations of the two boluses.

The dual-contrast method usually involves low-resolution dynamic imaging of the enhancement in the LV with short saturation recovery time, in addition to high-resolution imaging of myocardial enhancement with long saturation recovery time[111]. The AIF is acquired with a short saturation recovery time resulting in "low" T1 weighting which improves the linearity of the signal-intensity versus R1 relationship at higher contrast concentrations. The dual-contrast quantitative myocardial perfusion is sensitive to systematic errors due to the non-linear relationship between contrast agent concentration and MR signal. However, it is more clinically feasible, as the dual-bolus technique is more complicated to perform in routine practice.

The demand of avoiding arterial signal saturation requires imaging AIF with lower T1 weighting as fast as possible. Spiral trajectories have high efficiency in traversing k-space, which enables rapid acquisition of the AIF to avoid signal saturation. However,

spiral trajectories have not been applied to quantitative perfusion imaging.. Based on high quality and high spatio-temporal resolution perfusion imaging with whole heart coverage produced by the spiral trajectory as demonstrated in previous chapters, the goal of this aim is to develop a quantitative dual-contrast spiral perfusion sequence and validate the technique in healthy volunteers and patients with known or suspected CAD.

4.2 Methods

4.2.1 Dual Contrast Pulse Sequence Design

Our previously optimized spiral pulse sequence was modified to acquire proton density (PD) and AIF images for quantification as shown in Figure 4.1. The high resolution PD images were collected in the first 4 heart beats without a saturation pulse. The low resolution AIF was acquired during the saturation recovery time (SRT) of the first myocardial perfusion image, thus adding no additional imaging time to the sequence.
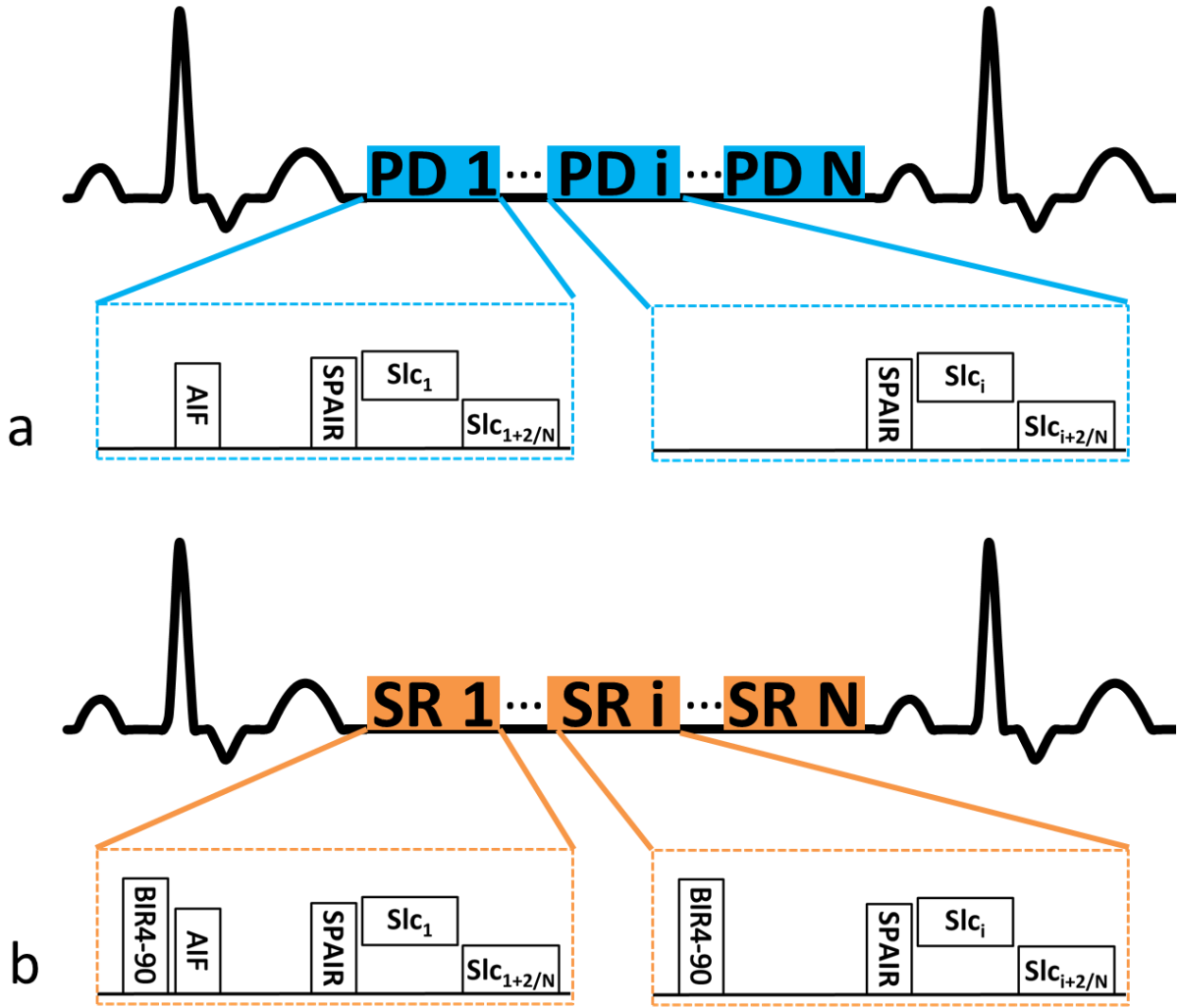
Figure 4.1 Schematic of the spiral absolute quantification sequence with whole heart coverage. Proton density images are collected in first 4 heart beats without saturation pulse (a). T1 weight perfusion images are acquired with BIR4 saturation pulse(b).

4.2.2 Signal Modeling

Quantitative assessment of myocardial perfusion is based on modeling of the contrast agent kinetics in the myocardium. Three major steps are needed to accurately convert the image pixel intensities to myocardial blood flow: 1) Conversion of the image intensity $S(t)$ to T1 values $T(t)$; 2) Conversion of the T1 values $T(t)$ to contrast agent

concentration $C(t)$; 3) Determination of absolute myocardial bold flow via Fermi function deconvolution of the contrast agent concentration curves in the myocardium and cavity.

A supplementary PD weighted image was used to correct the receive coil inhomogeneity profile and normalize signal observations directly via a PD weighted image using following equation:

$$S(x, y, t) = \frac{I(x, y, t)}{I_{PD}(x, y)} \cdot \frac{\sin(\alpha_{PD})}{\sin(\alpha_{T1})}$$

(4.1)

where α_{PD} and α_{T1} represent the imaging flip angles for PD and T1 weighted images, respectively.

Contrast agent concentration can be estimated from the normalized signal using the Bloch equation signal model[111]. Considering that the spiral sequence samples the center of k-space on each interleave, and samples each k-space radius at a similar time on each interleaf, at the same time for each trajectory, we modeled the Bloch equation as follows:

$$S(t) = \frac{\sum_{n=1}^{N} \left\{ \left(1 - (1-f)e^{-\frac{TD}{T(t)}} \right) \cdot \left[e^{-\frac{TR}{T(t)}} \cdot \cos(\alpha_{T1}) \right]^{n-1} + \left(1 - e^{-\frac{TR}{T(t)}} \right) \cdot \frac{1 - \left[e^{-\frac{TR}{T(t)}} \cdot \cos(\alpha_{T1}) \right]^{n-1}}{1 - e^{-\frac{TR}{T(t)}} \cdot \cos(\alpha_{T1})} \right\}}{\sum_{n=1}^{N} \left\{ \left[e^{-\frac{TR}{T(t)}} \cdot \cos(\alpha_{PD}) \right]^{n-1} + \left(1 - e^{-\frac{TR}{T(t)}} \right) \cdot \frac{1 - \left[e^{-\frac{TR}{T(t)}} \cdot \cos(\alpha_{PD}) \right]^{n-1}}{1 - e^{-\frac{TR}{T(t)}} \cdot \cos(\alpha_{PD})} \right\}}$$

(4.2)

where N is the number of imaging RF pulses of flip angle α_{T1}, TR is repetition time, TD is the delay between saturation and readout. $1 - f$ denotes the saturation efficiency of the pulse.

Then contrast agent concentration $C(t)$ is related to the T1 values $T(t)$ through:

$$\frac{1}{T(t)} = \frac{1}{T_0} + \varsigma \cdot C(t) \tag{4.3}$$

where T_0 is the baseline T1 value before any contrast agent has entered the region of interest, and ς is the relaxivity of the contrast agent at the system field intensity which is 3.8 L/mmol/sec for Magnevist Gd at 1.5T.

Based on the central volume principle, the relationship between the AIF and TF is defined as follow:

$$TF(t) = AIF(t) \otimes R(t) \tag{4.4}$$

Myocardial flow will be determined using standard Fermi function model[40] for constrained deconvolution of the tissue function with the AIF as follow:

$$R(t) = \frac{F}{1 + \exp(k \cdot (t - t_{T0} - \tau))} \tag{4.5}$$

where t_{T0} is the tissue contrast agent arrival time, F is the rate of flow, k is the decay rate due to contrast agent washout, and τ characterizes the Fermi function shoulder width. We are interested in $R(t = t_{T0})$ which represents the blood flow.

4.2.3 Processing Pipeline

Figure 4.2 summarizes the general signal processing pipeline from the acquisition of raw data to the determination of pixel-wise maps of MBF. The acquired undersampled raw k-space data were reconstructed using the L1-SPIRiT method described in Chapter

2 to obtain alias free perfusion images. Then, perfusion images were aligned to the middle time frame template image using the Advanced Normalization Tools (ANTS) registration toolbox[112] if there was any motion in the image series. Short axis ROIs were drawn on the registered perfusion images to divide the myocardium into 6 segments (anterior, anteroseptal, inferoseptal, inferior, inferlateral and anterolateral) for each slice position. The signal intensities were converted into gadolinium concentration-time curves as described above. Lastly, MBF values were determined using pixel-wise and segmental analysis..
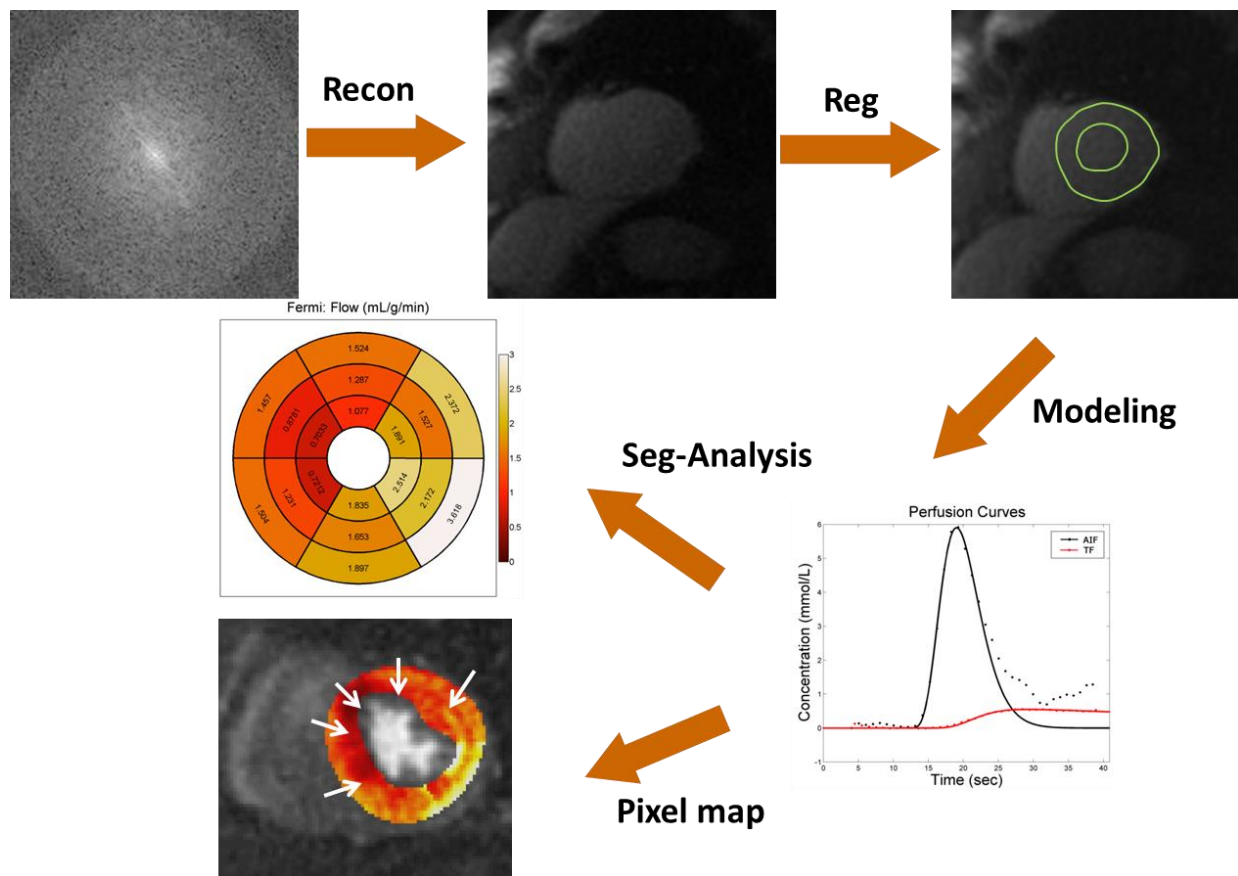
Figure 4.2 Spiral perfusion quantification processing pipeline. The undersampled raw k-space data was first reconstructed by CS methods and then image registration was performed to align all the perfusion images together. Short axis ROIs were drawn in the registered images to further

perform signal modeling to convert the image intensities to concentration curve. Segment or pixel map of MBF was calculated through Fermi deconvolution.

4.2.4 Phantom Validation

As the accurate determination of gadolinium concentration from T1 is essential for quantification of perfusion, T1 measurement were validated in a phantom with 10 tubes of differing gadolinium concentrations in the expected range for the LV cavity and the myocardium (0.10 mmol/L to 10 mmol/L). The dual-contrast sequence was used to estimate the T1 values. We assessed the linearity of the relationship between derived and actual gadolinium concentrations by plotting the measured R1 for each phantom versus the actual gadolinium concentration. The standard inversion recovery spin echo (IR-SE) sequence was used as the ground truth for the T1 values of each phantom. . Parameters of IR-SE sequence included: FOV 320 mm, matrix size 96x128, slice thickness 20 mm, TR 10000 ms, TE 8.4 ms, bandwidth 19.3 kHz, 30 inversion times from 25 ms to 5000 ms. Saturation efficiency was calculated using single-shot spiral gradient echo sequence with 1 ms TE, 3000 ms TR, 90° flip angle without a saturation pulse and with 2 saturation recovery times 10 and 20 ms.

4.2.5 Human Studies

The spiral dual-contrast sequence with whole heart coverage was evaluated in both healthy volunteers (N = 7) and patients with known or suspect CAD who were scheduled to undergo invasive angiography for evaluation of angina chest pain (N =7). All subjects were first imaged at stress during a 3 minutes infusion of 140 mcg/kg/min of adenosine (Astellas Pharmaceuticals). The rest perfusion imaging was separated by 10

minutes and the dose of contrast 0.075 mmol/kg Gd-DTPA (Bayer Pharmaceuticals) via a peripheral IV at a rate of 4ml/s was utilized for perfusion measurement. Late gadolinium enhancement images were obtained to detect myocardial infarction. Imaging was performed on a 1.5T MR Scanner (Magnetom Avanto, Siemens Healthcare) using 32 channel phased array coil. Written informed consent was obtained from all subjects, and imaging studies were performed under institutional review board (IRB) approved protocols. All patients with known or suspected CAD underwent coronary angiography. The perfusion imaging protocol consisted of the acquisition of PD images during the first 4 heart-beats followed by saturation-recovery prepared perfusion images over the next 50-70 heart beats depending on the patient's heart rate.. Other pulse sequence parameters were as follows: TS 80 ms, TE 1.0 ms, 5 ms spiral and 3 spirals per slice, effective TR 14 ms, FA 30º, 8 slices to cover the whole heart, 2 slices per saturation, FOV 340mm^2, in-plane resolution around 2 mm. AIF images were acquired with a single-shot spiral acquisition using a 45º FA with the following parameters: in-plane resolution 6.95 mm, TS 10 ms.

4.2.6 Image Analysis

The perfusion images from the healthy volunteers and CAD patients with known or suspected CAD were processed using the pipeline described above to quantify stress and resting MBF. Myocardial perfusion reserve (MPR), the ratio of stress flow to rest flow, was obtained for each myocardial segment for each slice. Segments with an MPR ≤ 1.5 were classified as ischemic. MPR was determined on a per-territory basis to compare with coronary angiography. For qualitative analysis, 2 cardiologists with experience in CMR perfusion imaging and blinded to patient data reviewed the perfusion images and

76

reported perfusion defects in each myocardial segment. Analysis of accuracy was done on a per patient and per vessel basis.

4.3 Results

4.3.1 Phantom

Figure 4.3 shows the gadolinium phantom with concentration range from 0 to 10 mmol/L. The T1 values were calculated within the drawn ROI for each tube. Table 4.1 showed the T1 values of gadolinium phantom from the IR-SE sequence.
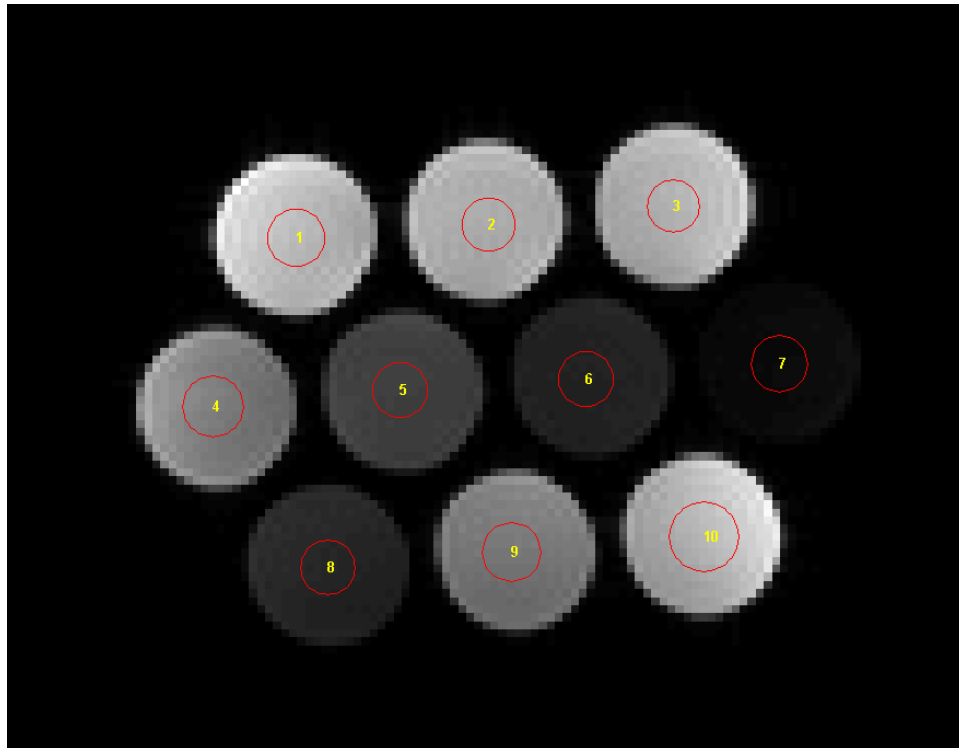
Figure 4.3 Gadolinium phantom with concentration range from 0 to 10 mmol/L. The 10 tubes have concentrations of 0 (saline), 0.1, 0.25, 0.5, 0.75, 1.0, 1.5, 2, 5, 10 mmol/L Gd respectively.

Table 4. 1 Gadolinium phantom concentration and T1 values from IR-SE sequence

Tube #	Conc. (mmol/L)	T1 (ms)
1	Saline	2579.14 ± 9.74
2	0.10	1184.60 ± 3.43
3	0.25	637.21 ± 1.77
4	0.50	359.79 ± 1.23
5	0.75	251.86 ± 0.75
6	1.00	189.70 ± 0.89
7	1.50	135.91 ± 0.51
8	2.00	103.94 ± 0.70
9	5.00	41.62 ± 0.17
10	10.00	22.07 ± 0.21

Figure 4.4 shows the relationship between the gadolinium concentration and the R1 values estimated from the AIF, TF and IR-SE images using the measured saturation efficiency 96.5%. The R1 estimation of TF and AIF is overestimated by about 3% as compared to the ground truth.
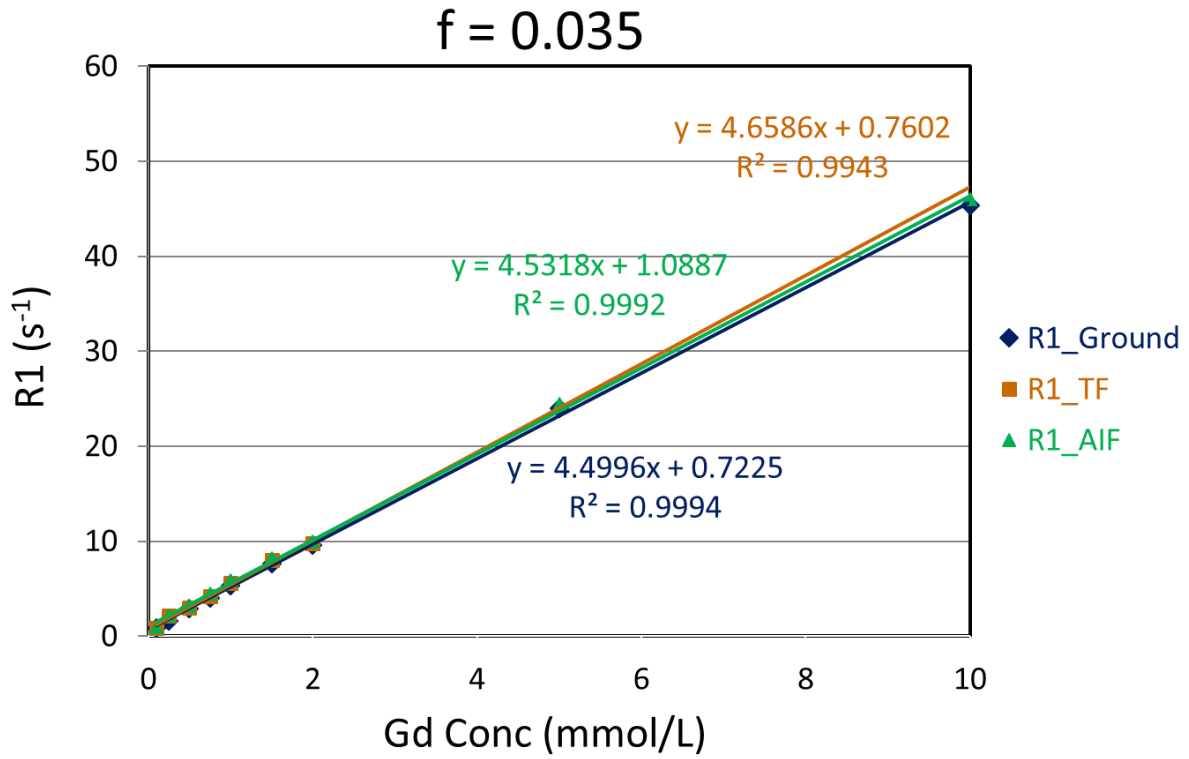
Figure 4.4 Relationship between the Gd concentration and R1 values estimated from AIF, TF and ground truth.

4.3.2 Healthy Volunteers

Figure 4.5 (a) showed the tissue function (TF) and AIF tracer concentration curves. AIF and TF images at different time points indicated on the time-concentration curves were presented in Figure 4.5 (b). The first time point showed the PD images. Both the PD and perfusion images from AIF and TF resulted in high SNR and quality.
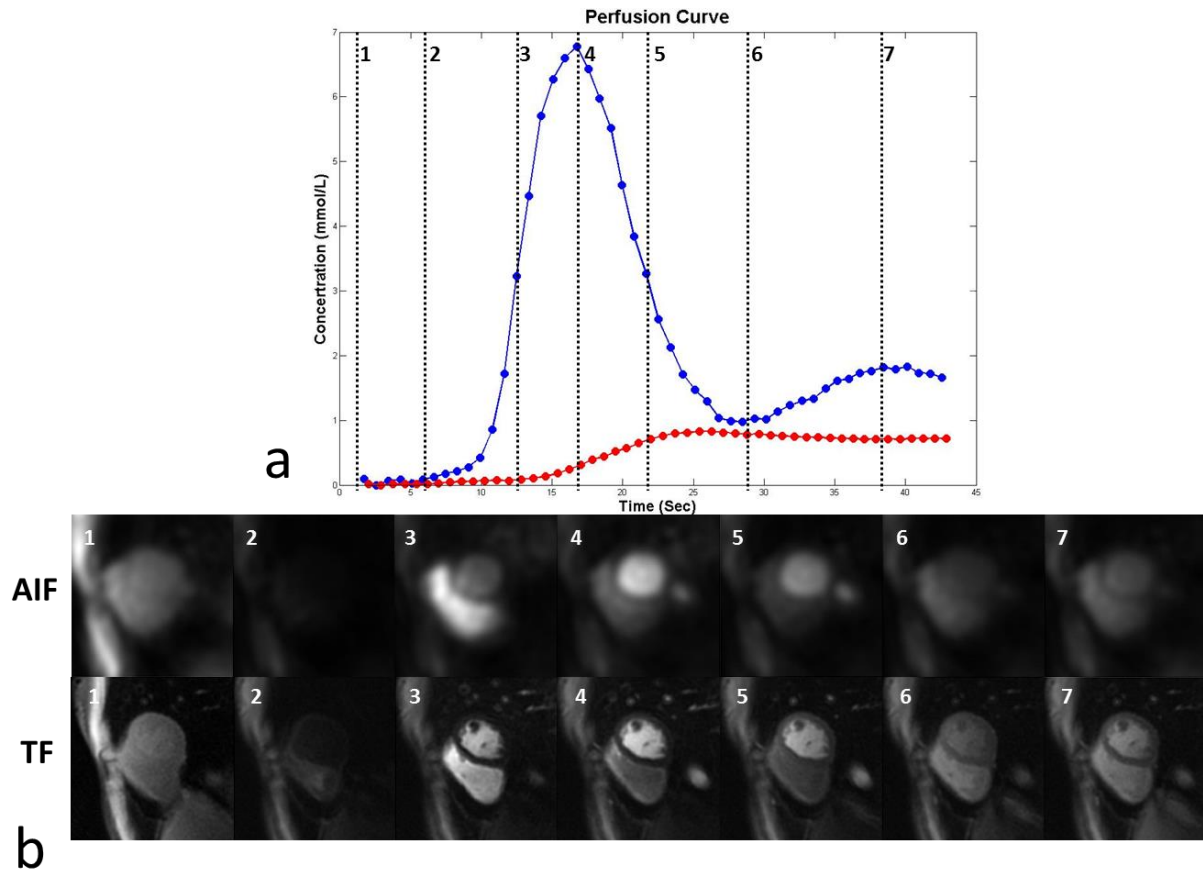
Figure 4.5 Example tissue function and AIF tracer concentration curves (a) and the perfusion images at multiple time points(b) from a healthy volunteer.

Example first-pass perfusion images from a healthy volunteer at stress and rest with whole heart coverage are shown in Figure 4.6, demonstrating excellent image quality with minimum artifacts. These images are calculated through modeling to get the stress MBF, rest MBF and MPR for further analysis. Pixelwise and bull-eye segment

quantification is show in Figure 4.7.
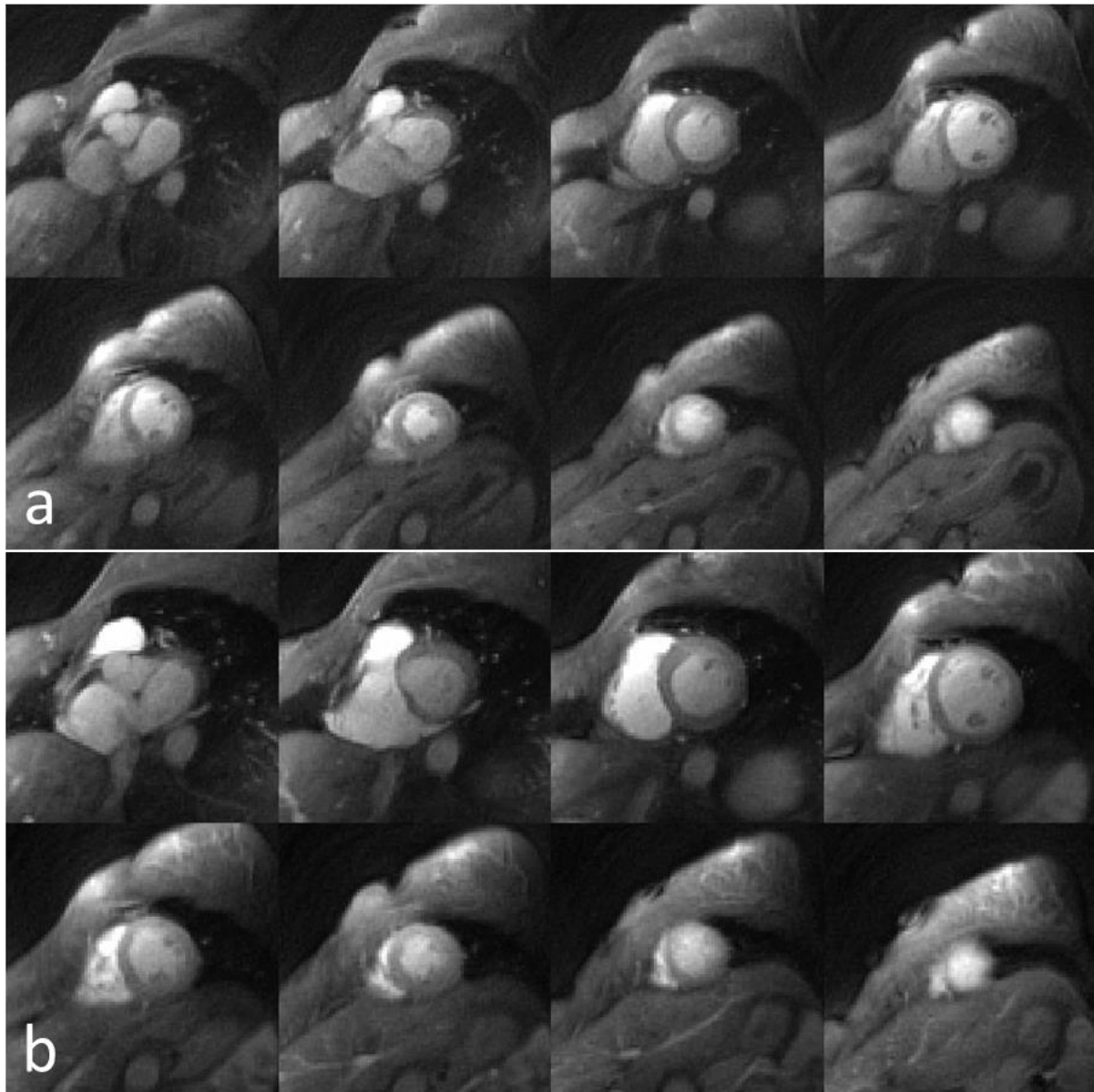
Figure 4.6 Example perfusion images from one healthy volunteer at stress (a) and at rest (b).
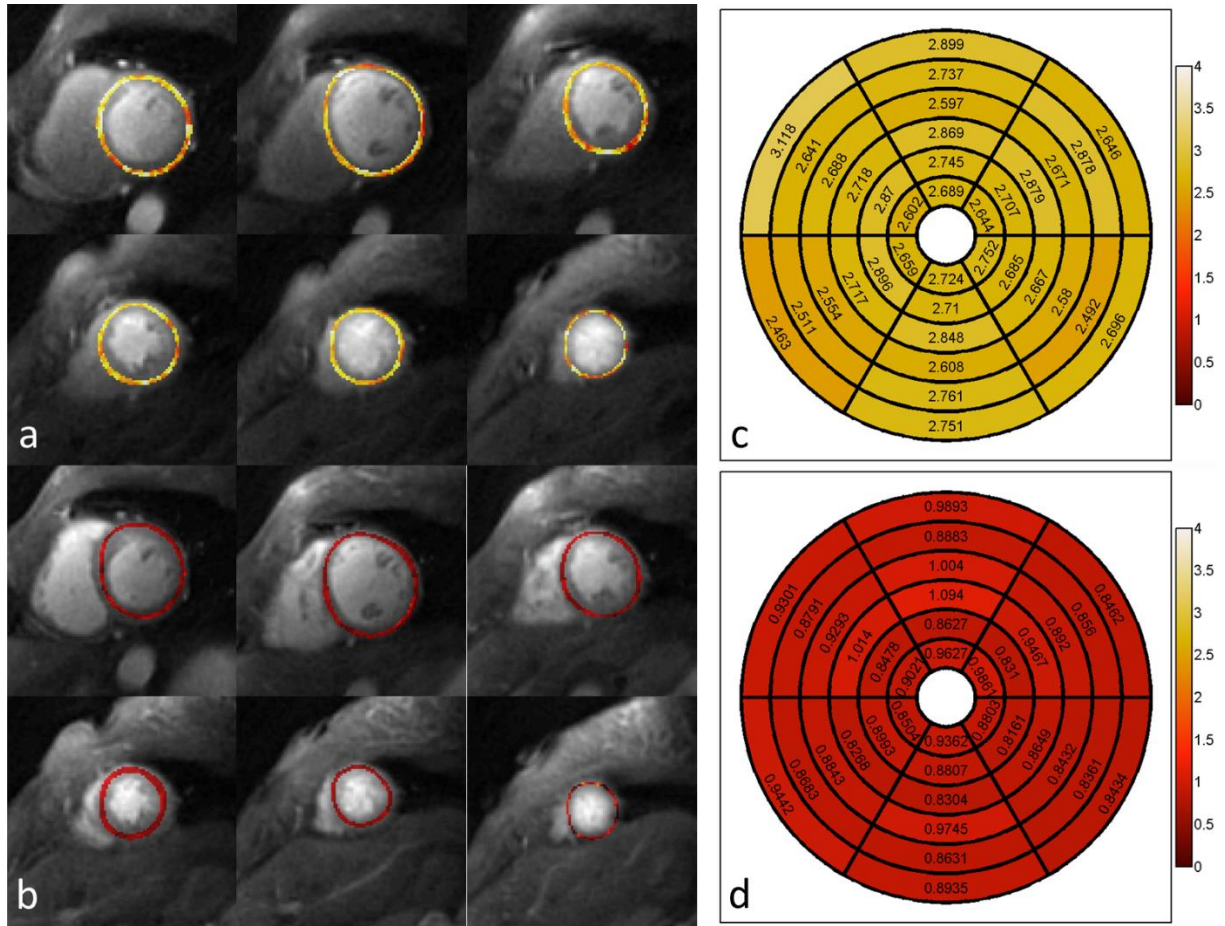
Figure 4.7 Pixelwise MBF map at stress (a) and rest (b) as well as the bull-eye segment plot at stress (c) and rest (d).

Figure 4.8 presents the distribution of the stress MBF, rest MBF and MPR from the healthy volunteer group. The mean resting MBF was 0.88 ± 0.16 mL/min/g across the 7 subjects. of the mean stress MBF was 2.71 ± 0.43 mL/min/g with larger variation, which is caused by the subject dependent response to vasodilator. The mean MPR is around 3.1 ± 0.56 for healthy volunteer group. The greater variation in stress perfusion values is likely caused by differences in the subject's response to adenosine.
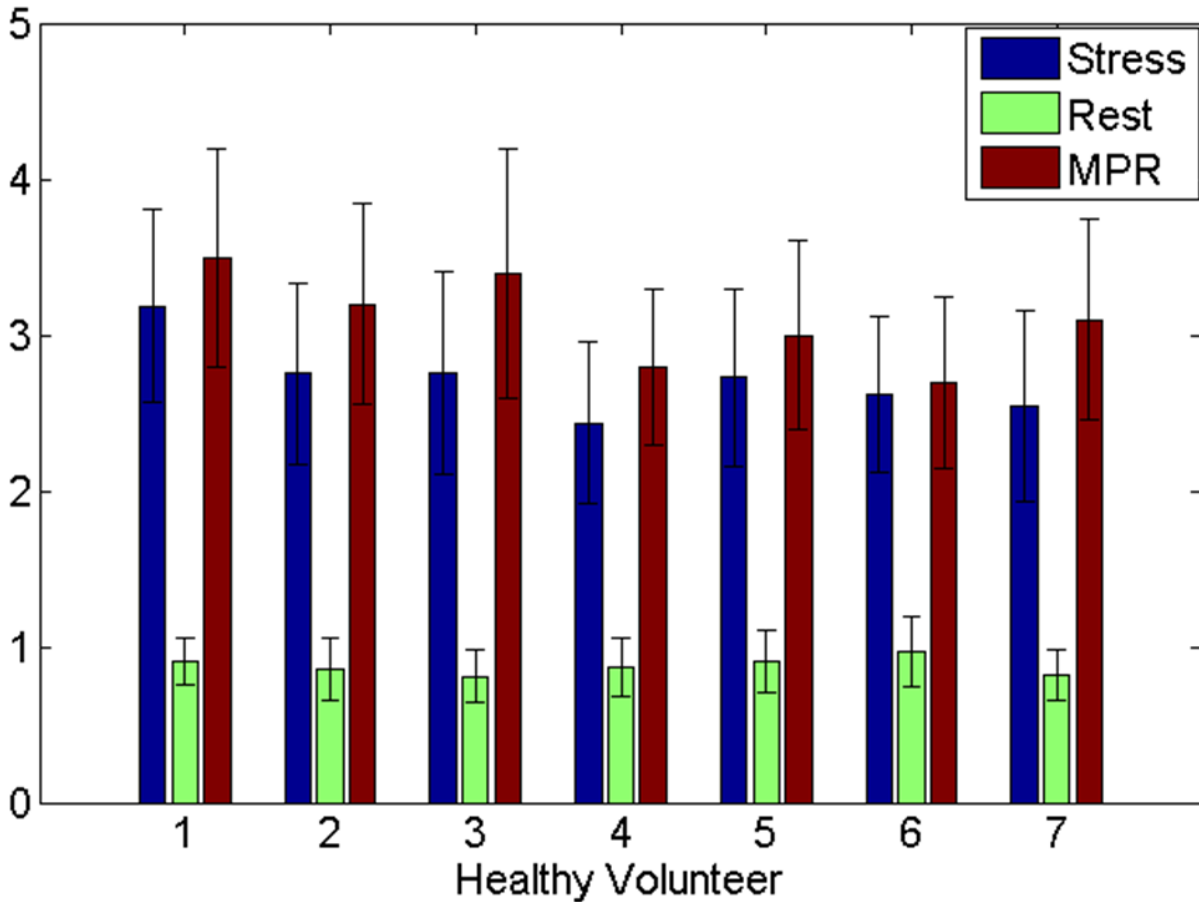
Figure 4.8 Distribution of the stress flow, rest flow and MPR from the healthy volunteer group. The mean rest flow across all healthy volunteer is 0.88 ± 0.16 mL/min/g, mean stress flow is 2.71 ± 0.43 mL/min/g and mean MPR is 3.1 ± 0.56.

4.3.3 CAD Patients

Figure 4.9 shows an example case of a suspected CAD patient undergoing quantitative spiral perfusion imaging. Stress perfusion images in (a) show a perfusion defect in anteroseptal regions of middle and apical slices with normal resting flow in (b).Quantitative stress MBF in (c) is less than 1 mL/min/g in the anteroseptal region and the mean MBF in remote regions is 3.5 ± 0.42 mL/min/g. The rest MBF in (d) is

homogeneous across all the segments and the mean MBF is around 0.92 ± 0.21 mL/min/g. The severely reduced perfusion in the anteroseptum was consistent with occlusion of the mid LAD seen on coronary angiography.
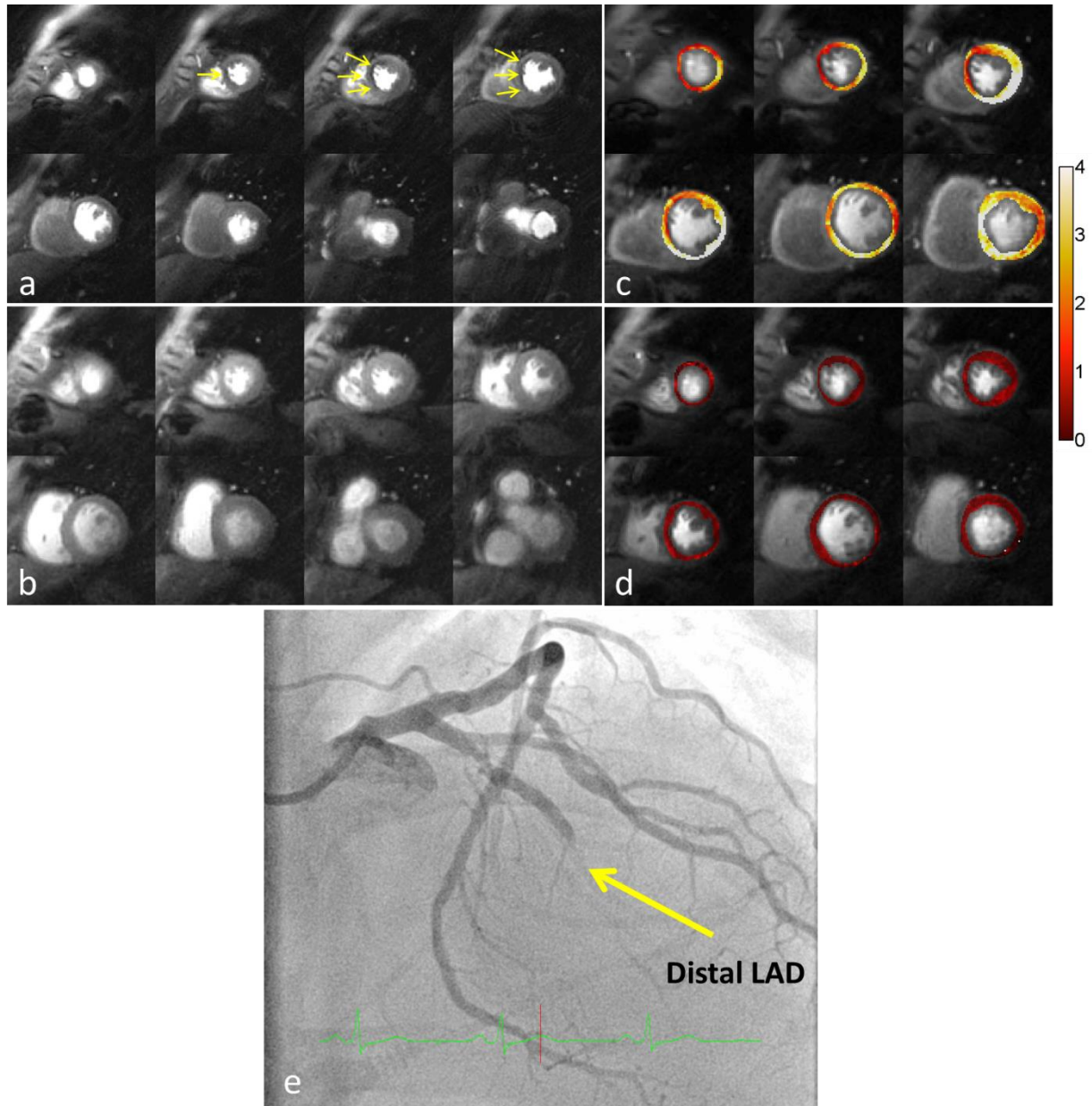
Figure 4.9 Example case of quantitative perfusion from a CAD patient. a: Stress perfusion images show the perfusion defects in anteroseptal regions in middle and apical slices. b: Rest perfusion

images show normal flow. c: Stress MBF map from the middle 4 slices. d: Rest MBF map from the middle 4 slices. e: Coronary angiography shows the stenosis in the distal LAD territory matched with the quantitative perfusion analysis.

Figure 4.10 shows another example case from a patient with CAD. The stress perfusion images demonstrate large area of perfusion defect in inferior myocardial across the whole myocardium in (a). The MBF map at stress in (b) shows the greatly reduced flow in inferior regions with the stress flow as low as 0.8 mL/min/g compared with the remote region's flow of 2 mL/min/g. At rest in (c), this patient had a mean MBF of 0.89 ± 0.18 mL/min/g. The detailed bull-eye segmental flow at stress and rest as well as the MPR is shown in (d). In addition, the reduced endo/epi ratios in the inferior and lateral walls is observed at stress. This patient's catheterization results show high grade stenosis in the LCx and a total occlusion of the RCA which is well matched with the quantitative perfusion analysis.
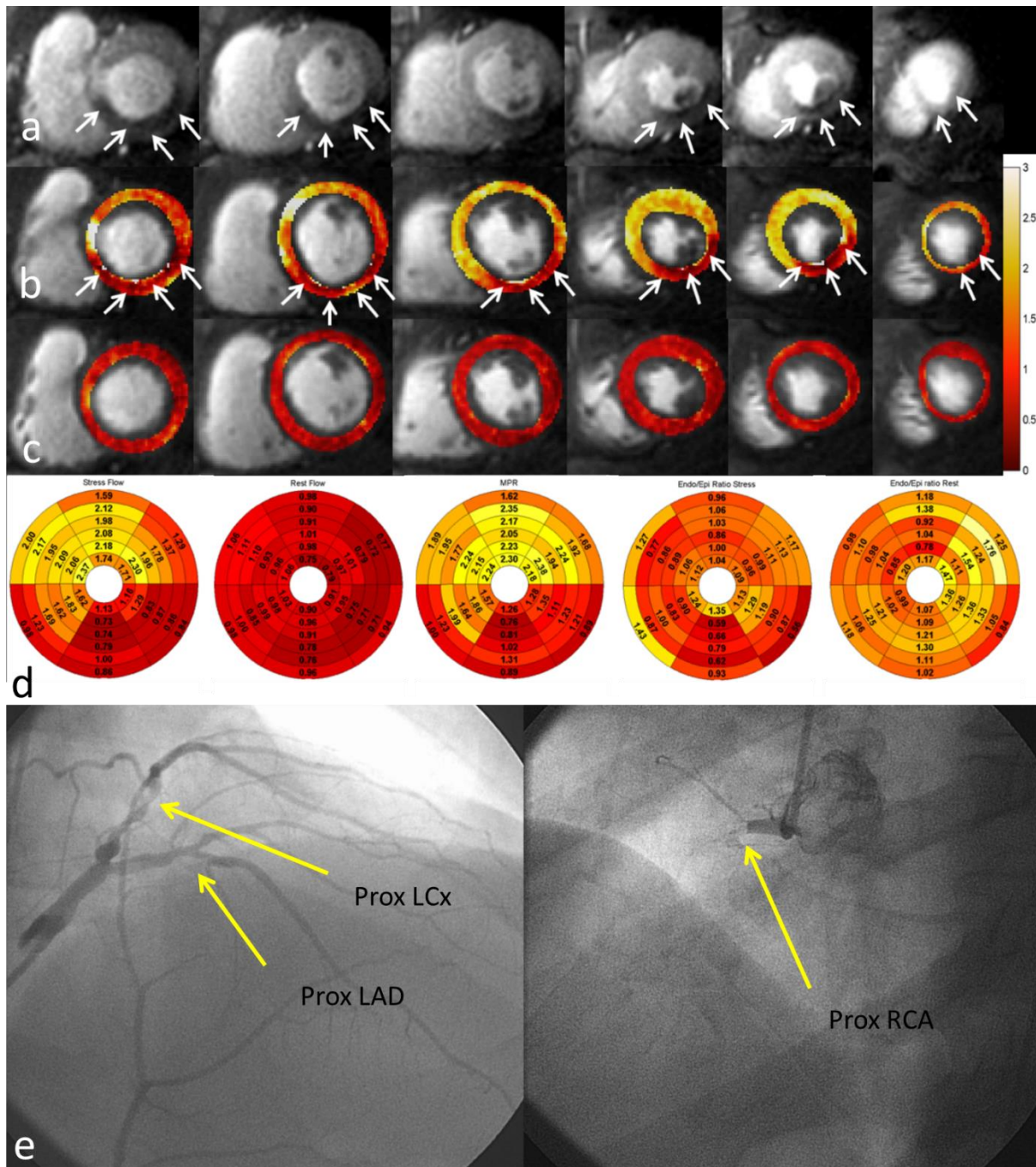
Figure 4.10 Example case of quantitative perfusion from another CAD patient. a: Stress

perfusion images show the perfusion defect in the inferior myocardial across all the slices. b:

Stress MBF map. c: Rest MBF map. d: Bull-eye plot to summarize the stress MBF, rest MBF

and MPR on a segmental analysis. e: Coronary angiography shows high grade stenosis in the LCx and a total occlusion of the RCA matched with the quantitative perfusion analysis.

On a per patient basis, quantitative perfusion was correct in 6/7 patients and visual analysis was correct in 7/7 patients. On a per vessel analysis, quantification was correct for 18/21 arteries while visual analysis was correct in 16/21 coronary territories. The one subject who was missed by quantitative analysis had abnormal perfusion in all 3 territories, and the patient was found to have diffuse non-obstructive CAD at coronary angiography. In this case, the reduced perfusion likely indicated microvascular dysfunction, which can cause diffuse perfusion abnormalities seen by quantitative analysis.

4.4 Discussion

In this study, a dual-contrast spiral trajectory quantitative sequence was developed by acquiring proton density images for normalization and low-resolution AIF images to accurately measure the AIF contrast concentrations in addition to the standard whole-heart perfusion images. The sequence was validated in a gadolinium phantom, healthy volunteer and patients with known or suspected CAD, resulting in high quality, accurate perfusion flow measurements.

The signal modeling using spiral trajectory is based on single point T1 measurement theory. From the phantom experiment, the estimation of R1 values using spiral sequence maintained good linearity with the gadolinium concentration which is essential for blood flow quantification. However, the single point measurement relied on strong assumptions regarding the fidelity of the pulse sequence and system.

Healthy volunteer perfusion experiments at stress and rest demonstrates the robust assessment of MBF using dual-contrast sequence technique. Generally, a MPR of 3.1 can be observed in healthy volunteer group. The variation in the stress MBF might account for the subject dependent response to vasodilators. The quantitative perfusion imaging technique provides user independent assessment of myocardium compared with visual analysis of perfusion images.

The study has several limitations. Single-point T1 measurement (based on the Bloch simulation of the PD and saturation weighted signal intensities) does not accurately measure T1 over the large range of possible T1 values in the myocardium. Multi-point T1 measurements could potentially improve accuracy and requires further study.. The sample size of human study for both healthy volunteers and CAD patients is small. We cannot draw firm conclusions regarding the MBF or MPR cut-off values to diagnose CAD. This study is also limited by the lack of in-vivo validation of MBF, either comparing with the PET imaging or using animal model with microsphere is essential to validate the accuracy of MBF measurement in vivo. We are currently evaluating spiral perfusion pulse sequences in animal models of myocardial perfusion with microsphere validation.

4.5 Conclusion

We have demonstrated the application of spiral quantitative dual-contrast sequence in phantoms, healthy volunteers and patients with known or suspected CAD. This technique can produce high quality perfusion images for clinical use. Quantitative assessment of myocardial perfusion detected abnormal segments in better agreement with coronary angiography on a segmental basis, consistent with the concept that

quantitative assessment more accurately reflects ischemic burden in multi-vessel disease.

In the setting of microvascular disease, quantitative analysis may show reduced perfusion

in the absence of obstructive coronary artery disease as was seen in one of our subjects.

Further analysis will be needed to see if features such as the endocardial to epicardial

perfusion gradient could better differentiate obstructive CAD from microvascular disease.

Additional studies, including more subjects and appropriate age matching, are clearly

warranted to fully assess the potential of this technique.

Chapter 5: Conclusion and future work

5.1 Overview of Findings

Most of the work presented in this dissertation is related to the pulse sequence development. We first designed and evaluated two-dimensional (2D) L1-SPIRiT accelerated spiral pulse sequences for first-pass myocardial perfusion imaging with whole heart coverage capable of measuring eight slices at 2 mm in-plane resolution at heart rates up to 125 beats per minute. Combinations of five different spiral trajectories and four k-t sampling patterns were retrospectively simulated in 25 fully sampled datasets and reconstructed with L1-SPIRiT to determine the best combination of parameters. Two candidate sequences were prospectively evaluated in 34 human subjects to assess in vivo performance. We found that a dual density spiral trajectory with a broad transition region with either angularly uniform or golden angle in time k-t sampling pattern had the largest structural similarity and smallest root mean square error from the retrospective simulation, and the L1-SPIRiT reconstruction preserved the temporal dynamics. In vivo data demonstrated that both of the sampling patterns could produce high quality perfusion images with whole heart coverage.

Considering the fact that imaging efficiency is always low when the true ROI is smaller than the supporting FOV, we designed the 2D OVS pulse to only prepare an ROI around the heart to improve the imaging efficiency. The OVS module was incorporated into the single-shot excitation perfusion sequence to achieve ultra-high temporal resolution. The OVS module was simulated across a range of B0 and B1 values to assess

the effects of field inhomogeneity on the saturation performance. The rFOV single-shot excitation perfusion technique was validated in human studies to compare with normal full FOV imaging technique. rFOV technique generated higher quality perfusion images than full FOV imaging methods.

Furthermore, we designed a quantitative dual-contrast spiral sequence by additionally acquiring AIF and PD images. We proposed a signal model to convert the images intensities to myocardial blood flow values and we introduced a generalized processing pipeline to obtain the quantitative perfusion measurement from the raw k-space data. The sequence was further validated in phantoms, healthy volunteers and patients with known or suspected CAD and demonstrated that high quality and accurate blood flow measurements could be obtained. The quantitative method was compared with qualitative assessment and the quantitative technique provided user-independent and more accurate assessment among the CAD patients group.

5.2 Future Directions

5.2.1 3D rFOV perfusion

3D CMR perfusion imaging enables whole ventricular coverage at the same cardiac cycle permitting quantification of ischemic burden of patients being evaluated for coronary artery disease. Current 3D techniques have limited spatial-temporal resolution. Taking the advantage of the reduced FOV technique in this dissertation, we can develop an efficient outer-volume suppressed 3D Stack-of-Spiral perfusion sequence with motion-guided compressed sensing reconstruction which can acquire 20 partitions with 2mm in-plane, and 4 mm through-plane resolution with a temporal foot print of 180ms. Figure 5.1

shows a preliminary result of perfusion images at a single time frame during first-pass of contrast from one healthy volunteer using 3D rFOV technique. 2x sinc-interpolation of the 2x2x4 mm dataset, 40 slices with isotropic 2 mm resolution can be displayed (Figure 5.1 a) enabling isotropic visualization of perfusion in short and long axis image orientations (Figure 5.1 b).
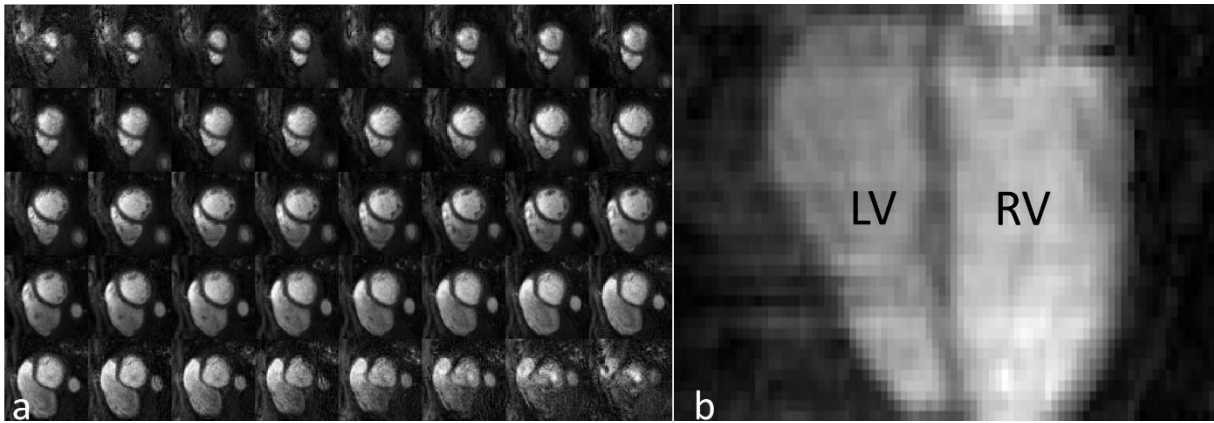
Figure 5.1 a) 40 slices of 2×2×2mm resolution with 180 ms temporal footprint. b) Long axis view perfusion images from isotropic resolution images of a).

5.2.2 Simultaneous multi-slice (SMS) acquisition

There has been recent interest in SMS as a way to increase coverage for 2D multi-slice imaging and promising preliminary results have been demonstrated for Cartesian[113] and radial imaging[114]. Multiple slices can be excited simultaneously (SMS), however the images from the slices are superimposed on each other, but can be separated using parallel imaging techniques. To improve image reconstruction by reducing overlap of image data from multiple slices, the CAIPHIRINHA technique can be used to linearly phase shift data enabling higher PI acceleration[115]. Spiral trajectories permit flexible kspace sampling density, and undersampling artifacts result in an incoherent aliasing

pattern, however the conventional CAIPHIRINHA approach is not applicable. We propose an approach where the phase of one slice is modulated by angles that sum to 2π across n excitations, and the excitation phase is incremented by the golden-angle between heartbeats. To test this idea, we retrospectively performed a reconstruction of data using the proposed scheme. Using spirals that densely sample the center of k-space, there is nearly complete destructive interference of the data from the interfering slice (Figure 5.2 c,h), and the residual aliasing pattern varies in time. By using an L1-SPIRIT reconstruction each image can separately be reconstructed with nearly perfect recovery of data from each slice (Figure 5.2 e,j). SMS will increase the number of slices by 2-4x without any significant SNR penalty or loss in image quality.
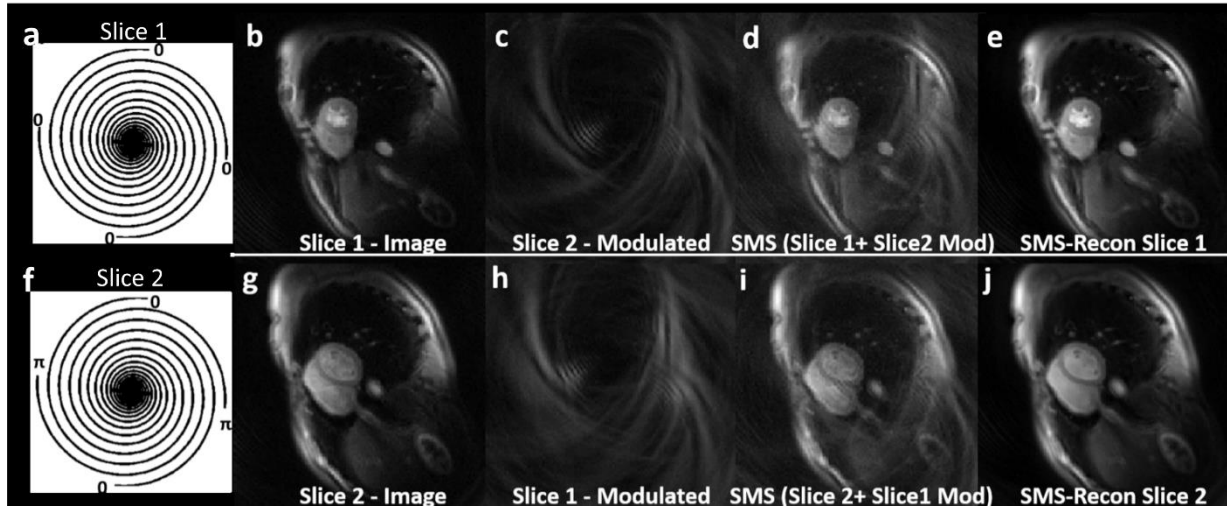
Figure 5.2 SMS reconstruction experiment: (a,f) show phase of trajectories for each of the excited slices, (b,g) are the independent images from each slice. (c,h) show the interference of each slice, on the other slice which only consists of an incoherent aliasing artifact. Thus (d,i) direct reconstruction of the data show minimal interference of the data from each slice on the other slice. L1-SPIRIT easily recovers images each slice with no SNR loss in (e,j). Aliasing in (c,h) will be improved with OVS.

5.2.3 Multiple-point AIF estimation

Current first-pass quantitative perfusion techniques are based on a theory-based signal calibration with single-point T1 measurement. Considering the fact that first-pass perfusion imaging is a relative low SNR technique and is estimating T1 over a large range especially in the LV cavity, the single-point T1 measurement has limited accuracy and precision.. Furthermore, this technique is dependent on the assumption that confounding factors such as the saturation efficiency, slice profile etc. do not have a significant impact on T1 measurement. One possible solution for this problem is instead of doing single-point T1 measurement, multiple-point measurement can be implemented to acquire low resolution AIF images with different TS values to improve the measurement accuracy of AIF, therefore, to improve the accuracy of MBF estimation. Furthermore, multiple echo time of AIF images can also be acquired to compensate the T2* effect especially for the peak of concentration in cavity during first-pass.

5.3 Collaborations and Contributions

The work in this dissertation includes many contributions from collaborators. I would like to thank them for their efforts here.

The basic spiral trajectory gradient generation code, and system calibration is based on work over a number of years from Dr. Meyer's lab. Dr. Salerno had implemented the original spiral perfusion pulse sequence based Dr. Meyer's gradient design that provided the starting point for this dissertation. I further extended the spiral pulse sequence to support a variety of spiral trajectory designs and k-t sampling patterns. I implemented the modifications to support the acquisition of the AIF and PD images for

quantitative perfusion imaging. I further modified this code to support reduced FOV and single-shot spiral perfusion image acquisition. The online reconstruction pipeline in the scanner called "IceGrid" was also developed by Dr. Meyer's lab, and I modified that to meet our needs to perform quantitative perfusion imaging. I developed the off-line reconstruction pipeline including implementation of L1-SPIRIT and registration techniques based on ANTs. The application of the BLOSM technique used in Chapter 3 was implemented in collaboration with Dr. Xiao Chen and the Dr. Epstein's lab. I had important discussions and exchange of ideas with Dr. Li Zhao in developing the rFOV pulse, and he gave me a lot of helpful feedback to improve the pulse.

The whole dissertation was supervised by my advisor Dr. Michael Salerno, but I independently implemented the techniques used in this dissertation. Multiple paper and conference abstracts have published during my Ph.D., and detailed information can be found in Appendix.

Appendix

First-authored Journal Publications

1. **Yang Y**, Kramer CM, Shaw PW, Meyer CH, Salerno M. First-pass myocardial perfusion imaging with whole-heart coverage using L1-SPIRiT accelerated variable density spiral trajectories. Magnetic Resonance in Medicine 2015. DOI: 10.1002/mrm.26014

Co-authored Journal Publications

1. Chen X, Salerno M, **Yang Y**, Epstein FH. Motion-compensated compressed sensing for dynamic contrast-enhanced MRI using regional spatiotemporal sparsity and region tracking: Block low-rank sparsity with motion-guidance (BLOSM). Magnetic Resonance in Medicine 2013.

2. Salerno M, Taylor A, **Yang Y**, Kuruvilla S, Ragosta M, Meyer CH, Kramer CM. Adenosine Stress Cardiovascular Magnetic Resonance With Variable Density Spiral Pulse Sequences Accurately Detects Coronary Artery Disease: Initial Clinical Evaluation. Circulation: Cardiovascular Imaging 2014:CIRCIMAGING. 113.001584.

3. Salerno M, Janardhanan R, Jiji RS, Brooks J, Adenaw N, Mehta B, **Yang Y**, Antkowiak P, Kramer CM, Epstein FH. Comparison of methods for determining the partition coefficient of gadolinium in the myocardium using T1 mapping. Journal of Magnetic Resonance Imaging 2013;38(1):217-224.

4. Yap PT, Chen Y, An H, **Yang Y**, Gilmore JH, Lin W, Shen D. SPHERE: SPherical Harmonic Elastic REgistration of HARDI data. Neuroimage 2011;55(2):545-56.

First-authored Conference Publications

1. **Yang Y**, Zhao L, Chen X, Chow K, Shaw PW, Gonzalez JA, Epstein FH, Meyer CH, Kramer CM, Salerno M. Reduced field-of-view stack-of-spirals enables high spatiotemporal resolution 3D perfusion imaging. Journal of Cardiovascular Magnetic Resonance 2016;18(Suppl 1): P325

2. **Yang Y**, Zhao L, Chen X, Shaw P, Gonzalez J, Epstein FH, Meyer CH, Kramer CM, Salerno M. Reduced Field-Of-View Single-Shot Spiral Perfusion Imaging. Proc Intl Soc Mag Reson Med 2015;23:1005

3. **Yang Y**, Shaw P, Gonzalez JA, Kramer CM, Salerno M. Single breath-hold 3D LGE using stack of spiral trajectory. Journal of Cardiovascular Magnetic Resonance 2015;17 (Suppl 1):Q45

4. **Yang Y**, Chen X, Epstein FH, Meyer CH, Kuruvilla S, Kramer CM, Salerno M. Motion-corrected compressed-sensing enables robust spiral first-pass perfusion imaging with whole heart coverage. Journal of Cardiovascular Magnetic Resonance 2014;16(Suppl 1):O81.

5. **Yang Y**, Chen X, Epstein FH, Meyer CH, Kramer CM, Salerno M. 3D Whole-Heart Quantitative First-Pass Perfusion Imaging with a Stack-Of Spirals Trajectory. Proc Intl Soc Mag Reson Med 2014;22:878

6. **Yang Y**, Meyer CH, Kramer CM, Salerno M. Improved Spiral First-Pass Perfusion Imaging with Motion-Corrected Compressed Sensing. Proc Intl Soc Mag Reson Med 2014;22:4357

7. **Yang Y**, Kuruvilla S, Meyer CH, Epstein FH, Taylor AM, Kramer CM, Salerno M. High-resolution quantitative spiral perfusion for microvascular coronary dysfunction detection. Journal of Cardiovascular Magnetic Resonance 2014;16(Suppl 1):P227.

8. **Yang Y**, Feng X, Meyer CH, Kramer CM, Salerno M. First-pass myocardial perfusion imaging with whole ventricular coverage using L1-SPIRIT accelerated spiral trajectories. Journal of Cardiovascular Magnetic Resonance 2013;15(Suppl 1):P20.

9. **Yang Y**, Kuruvilla S, Meyer CH, Kramer CM, Salerno M. Quantification of myocardial perfusion with spiral pulse sequences. Journal of Cardiovascular Magnetic Resonance 2013;15(Suppl 1):E12.

10. **Yang Y**, Meyer CH, Epstein FH, Kramer CM, Salerno M. Single-Shot Spiral First-Pass Perfusion Imaging: Full Heart Coverage with High Temporal Resolution. Proc Intl Soc Mag Reson Med 2013;21:4556

11. **Yang Y**, Kuruvilla S, Meyer CH, Kramer CM, Salerno M. Whole-Heart Quantification of Myocardial Perfusion with Spiral Pulse Sequences. Proc Intl Soc Mag Reson Med 2013;21:4573

12. **Yang Y**, Meyer CH, Epstein FH, Kramer CM, Salerno M. Single-shot spiral first-pass perfusion imaging. ISMRM Workshop: Data Sampling & Image Reconstruction 2013

13. **Yang Y**, Chen X, Feng X, Wang M, Epstein FH, Meyer CM, Salerno M. Evaluation of Parallel Reconstruction Techniques for First-Pass Perfusion Imaging Using Spiral Trajectories. Proc Intl Soc Mag Reson Med 2012;20:3956

14. **Yang Y**, An H, Shi F, Gao W, Shen D, Lin W. Temporal Evolution of Brain Metabolic Substrates Differs Among Major Anatomical Lobes During the First Months of Life in Human. Proc Intl Soc Mag Reson Med 2011;19:4313

Co-authored Conference Publications

1. Shaw PW, **Yang Y**, Gonzalez JA, Kuruvilla S, Gottbrecht M, Epstein FH, Gan L, Keeley EC, Kramer CM, Salerno M. Extracellular volume by CMR is associated with serum biomarkers of extracellular matrix turnover and inflammation in hypertensive heart disease. Journal of Cardiovascular Magnetic Resonance 2016;18(Suppl 1): O103

2. Chow K, **Yang Y**, Salerno M. Robust free-breathing SASHA T1 mapping using high-contrast image-based registration. Journal of Cardiovascular Magnetic Resonance 2016;18(Suppl 1): P28

3. Cai X, Chen X, **Yang Y**, Salerno M, Weller D, Meyer CH, Epstein FH. Free-breathing 2D Cine DENSE with Localized Excitation Self-navigation and Motion CorrectionJournal of Cardiovascular Magnetic Resonance 2016;18(Suppl 1): P319

4. Gonzalez JA, Li Y, Shaw PW, Balfour PC, **Yang Y**, Kay J, DiMaria J, Weltman A, Salerno Michael, Meyer Craig H. Phosphocreatine recovery time constant (PCr)

at peak exercise as a potential endpoint for clinical trials in PAD. Journal of Cardiovascular Magnetic Resonance 2016;18(Suppl 1): P352

5. Shaw PW, **Yang Y**, Chow K, Gonzalez JA, Balfour PC, Meyer CH, Epstein FH, Bourque J, Salerno M, Kramer Christopher M. Quantitative CMR perfusion imaging identifies reduced flow reserve in microvascular coronary artery disease. Journal of Cardiovascular Magnetic Resonance 2016;18(Suppl 1): P79

6. Gonzalez JA, Li Y, Shaw PW, Kay J, McKenzie R, Lopez D, Sharma A, DiMaria J, **Yang Y**, Gina P. Determinants of exercise calf muscle perfusion in Peripheral Arterial Disease (PAD). Journal of Cardiovascular Magnetic Resonance 2016;18(Suppl 1): P356

7. Naresh NK, **Yang Y**, Holmes JW, Salerno M, Epstein FH. High temporal-resolution phase-contrast MRI demonstrates impaired left-ventricular diastolic relaxation in mice fed a high-fat high-sucrose diet. Journal of Cardiovascular Magnetic Resonance 2016;18(Suppl 1): P50

8. Chen X, Salerno M, Kramer CM, Mehta BB, **Yang Y**, Shaw P, Epstein FH. Prospectively Accelerated CMR First-Pass Perfusion Imaging in Patients with Suspected Heart Disease. Proc Intl Soc Mag Reson Med 2015;23:4485

9. Huang W, **Yang Y**, Chen X, Salerno M. Simple Motion Correction Strategy Reduces Respiratory-Induced Motion Artifacts for K-T Accelerated CMR Perfusion Imaging . Proc Intl Soc Mag Reson Med 2015;23:3686

10. Salerno M, **Yang Y**, Shaw P, Taylor A, Meyer CH, Epstein FH, Kramer CM. High Resolution Quantitative Spiral CMR Perfusion Imaging Demonstrates a Reduced

Endocardial to Epicardial Perfusion Gradient and Myocardial Flow Reserve in Patients with Microvascular Disease. Proc Intl Soc Mag Reson Med 2015;23:4484

11. Shaw P, **Yang Y**, Li Y, Gonzalez J, Taylor AM, Meyer CH, Epstein FH, Salerno M, Kramer CM. High resolution CMR perfusion imaging demonstrates reduced flow reserve and endo/epi ratio in microvascular coronary disease. Journal of Cardiovascular Magnetic Resonance 2015;17 (Suppl 1):P148

12. Gonzalez J, Shaw P, **Yang Y**, Kramer CM, Salerno M. ShMOLLI and 5(4R) 3 MOLLI T1 mapping in HCM detect similar ECV despite a difference in absolute T1 measurements. Journal of Cardiovascular Magnetic Resonance 2015;17 (Suppl 1):P326

13. Feng X, **Yang Y,** Meyer CH, Salerno M. Accelerated Myocardial Perfusion Imaging Using Saturation-Recovery Spiral-In/Out SSFP. Journal of Cardiovascular Magnetic Resonance 2015;17 (Suppl 1):P408

14. Chen X, Salerno M, Kramer CM, Mehta BB, **Yang Y**, Shaw P, Epstein FH. Prospectively accelerated first-pass myocardial perfusion imaging in patients using motion-compensated compressed sensing exploiting regional low-rank sparsity. Journal of Cardiovascular Magnetic Resonance 2015;17 (Suppl 1):O40

15. Chen X, **Yang Y**, Salerno M, Meyer CH, Epstein FH. Accelerated Cine DENSE Using Variable Density Spirals and Compressed Sensing with Parallel Imaging. Proc Intl Soc Mag Reson Med 2014;22:3892

16. Chen X, **Yang Y**, Salerno M, Epstein FH. Accelerated First-Pass Perfusion MRI Using BLOSM: Evaluation Using Dynamic Simulations and Patient Datasets with Prominent Respiratory Motion. Proc Intl Soc Mag Reson Med 2014;22:880

17. Feng X, **Yang Y**, Lopez D, Salerno M, Meyer CH. Myocardial Perfusion Imaging Using Transient-Phase Spiral-In/Out SSFP. Proc Intl Soc Mag Reson Med 2014;22:3938

18. Qing K, Ruppert K, Altes T, Jiang Y, Mata J, Miller WG, **Yang Y**, Shim Y, Guan S, Ruset I, Hersman WF, Mugler JP. Regional Mapping of Gas Uptake by Lung Tissue and Blood in Subjects with Asthma Using Hyperpolarized Xenon-129 MRI. Proc Intl Soc Mag Reson Med 2014;22:774

19. Salerno M, Taylor AM, **Yang Y**, Kuruvilla S, Meyer CH, Kramer CM. Adenosine stress CMR with variable density spiral pulse sequences accurately detects CAD with minimal dark-rim artifacts. Journal of Cardiovascular Magnetic Resonance 2014;16(Suppl 1):O58.

20. Kuruvilla S, Janardhanan R, **Yang Y**, Hamirani YS, Epstein FH, Keeley EC, Kramer CM, Salerno M. Increased extracellular volume and altered mechanics are associated with left ventricular hypertrophy in hypertensive heart disease, not hypertension alone. Journal of Cardiovascular Magnetic Resonance 2014;16(Suppl 1):P393.

21. Chen X, **Yang Y**, Salerno M, Meyer CH, Epstein FH. Accelerated cine DENSE MRI using compressed sensing and parallel imaging. Journal of Cardiovascular Magnetic Resonance 2014;16(Suppl 1):W16.

22. Hamirani YS, Salerno M, **Yang Y**, Kramer CM, Bourque J. Prevalence and correlation of abnormal flow reserve by stress CMR and coronary artery plaque by cardiac CTA in symptomatic diabetics. Journal of Cardiovascular Magnetic Resonance 2014;16(Suppl 1):O57.

23. Salerno M, **Yang Y**, Kuruvilla S, Meyer CH, Kramer CM. Quantitative Spiral Perfusion Imaging: Initial Clinical Experience. Proc Intl Soc Mag Reson Med 2013;21:316

24. An H, Ford AL, Eldeniz C, **Yang Y**, Chen Y, Vo KD, Powers WJ, Lee JM, Lin W. Operatively Defined Ischemic Core, Penumbra & Oligemia in Human Acute Stroke using Sequential MR Perfusion Images. Proc Intl Soc Mag Reson Med 2011;19:463

Patents

1. Epstein FH, Chen X, **Yang Y**, Salerno M. Systems and methods for accelerated dynamic magnetic resonance imaging. US Patent 9,224,210

2. Chen X, Epstein FH, **Yang Y**, Salerno M, Meyer CH. Systems and methods for accelerated imaging using variable density sampling and compressed sensing with parallel imaging. US Patent 20,150,285,889

Bibliography

1.   Al-Saadi N, Nagel E, Gross M, Bornstedt A, Schnackenburg B, Klein C, Klimek W, Oswald H, Fleck E. Noninvasive detection of myocardial ischemia from perfusion reserve based on cardiovascular magnetic resonance. Circulation 2000;101(12):1379-83.

2.   Schwitter J, Nanz D, Kneifel S, Bertschinger K, Buchi M, Knusel PR, Marincek B, Luscher TF, von Schulthess GK. Assessment of myocardial perfusion in coronary artery disease by magnetic resonance: a comparison with positron emission tomography and coronary angiography. Circulation 2001;103(18):2230-5.

3.   Nagel E, Klein C, Paetsch I, Hettwer S, Schnackenburg B, Wegscheider K, Fleck E. Magnetic resonance perfusion measurements for the noninvasive detection of coronary artery disease. Circulation 2003;108(4):432-7.

4.   Nandalur KR, Dwamena BA, Choudhri AF, Nandalur MR, Carlos RC. Diagnostic performance of stress cardiac magnetic resonance imaging in the detection of coronary artery disease: a meta-analysis. J Am Coll Cardiol 2007;50(14):1343-53.

5.   Rieber J, Huber A, Erhard I, Mueller S, Schweyer M, Koenig A, Schiele TM, Theisen K, Siebert U, Schoenberg SO and others. Cardiac magnetic resonance perfusion imaging for the functional assessment of coronary artery disease: a comparison with coronary angiography and fractional flow reserve. Eur Heart J 2006;27(12):1465-71.

6.   Klem I, Heitner JF, Shah DJ, Sketch MH, Jr., Behar V, Weinsaft J, Cawley P, Parker M, Elliott M, Judd RM and others. Improved detection of coronary artery

disease by stress perfusion cardiovascular magnetic resonance with the use of delayed enhancement infarction imaging. J Am Coll Cardiol 2006;47(8):1630-8.

7.   Hachamovitch R, Hayes SW, Friedman JD, Cohen I, Berman DS. Comparison of the short-term survival benefit associated with revascularization compared with medical therapy in patients with no prior coronary artery disease undergoing stress myocardial perfusion single photon emission computed tomography. Circulation 2003;107(23):2900-7.

8.   Shaw LJ, Berman DS, Maron DJ, Mancini J, Hayes SW, Hartigan PM, Weintraub WS, O'Rourke RA, Dada M, Spertus JA and others. Optimal medical therapy with or without percutaneous coronary intervention to reduce ischemic burden - Results from the Clinical Outcomes Utilizing Revascularization and Aggressive Drug Evaluation (COURAGE) trial nuclear substudy. Circulation 2008;117(10):1283-1291.

9.   Di Bella EV, Parker DL, Sinusas AJ. On the dark rim artifact in dynamic contrast-enhanced MRI myocardial perfusion studies. Magn Reson Med 2005;54(5):1295-9.

10. Gerber BL, Raman SV, Nayak K, Epstein FH, Ferreira P, Axel L, Kraitchman DL. Myocardial first-pass perfusion cardiovascular magnetic resonance: history, theory, and current state of the art. J Cardiovasc Magn Reson 2008;10:18.

11. Kellman P, Arai AE. Imaging sequences for first pass perfusion --a review. J Cardiovasc Magn Reson 2007;9(3):525-37.

12. Storey P, Chen Q, Li W, Edelman RR, Prasad PV. Band artifacts due to bulk motion. Magnetic Resonance in Medicine 2002;48(6):1028-1036.

13.   Salerno M, Sica CT, Kramer CM, Meyer CH. Optimization of spiral-based pulse sequences for first-pass myocardial perfusion imaging. Magn Reson Med 2011;65(6):1602-10.

14.   Mozaffarian D, Benjamin EJ, Go AS, Arnett DK, Blaha MJ, Cushman M, Das SR, de Ferranti S, Despres JP, Fullerton HJ and others. Heart Disease and Stroke Statistics-2016 Update: A Report From the American Heart Association. Circulation 2016;133(4):e38-e360.

15.   Moore B, Levit K, Elixhauser A. Costs for Hospital Stays in the United States, 2012: Statistical Brief #181. Healthcare Cost and Utilization Project (HCUP) Statistical Briefs. Rockville (MD)2006.

16.   Patel MR, Peterson ED, Dai D, Brennan JM, Redberg RF, Anderson HV, Brindis RG, Douglas PS. Low diagnostic yield of elective coronary angiography. N Engl J Med 2010;362(10):886-95.

17.   Pijls NH, De Bruyne B, Peels K, Van Der Voort PH, Bonnier HJ, Bartunek JKJJ, Koolen JJ. Measurement of fractional flow reserve to assess the functional severity of coronary-artery stenoses. N Engl J Med 1996;334(26):1703-8.

18.   Pijls NH, Van Gelder B, Van der Voort P, Peels K, Bracke FA, Bonnier HJ, el Gamal MI. Fractional flow reserve. A useful index to evaluate the influence of an epicardial coronary stenosis on myocardial blood flow. Circulation 1995;92(11):3183-93.

19.   Tonino PA, De Bruyne B, Pijls NH, Siebert U, Ikeno F, van' t Veer M, Klauss V, Manoharan G, Engstrom T, Oldroyd KG and others. Fractional flow reserve versus angiography for guiding percutaneous coronary intervention. N Engl J Med 2009;360(3):213-24.

20.   Wikipedia.   10   April.   Coronary   circulation. <https://en.wikipedia.org/wiki/Coronary_circulation>. Accessed 2016 10 April.

21.   Katz LN, Feinberg H. The relation of cardiac effort to myocardial oxygen consumption and coronary flow. Circ Res 1958;6(5):656-69.

22.   Hansson GK. Mechanisms of disease - Inflammation, atherosclerosis, and coronary artery disease. New England Journal of Medicine 2005;352(16):1685-1695.

23.   Wikipedia.   10   April.   Coronary   artery   disease. <https://en.wikipedia.org/wiki/Coronary_artery_disease>. Accessed 2016 10 April.

24.   Gould KL, Lipscomb K, Hamilton GW. Physiologic Basis for Assessing Critical Coronary Stenosis - Instantaneous Flow Response and Regional Distribution during Coronary Hyperemia as Measures of Coronary Flow Reserve. American Journal of Cardiology 1974;33(1):87-94.

25.   Ward RP, Al-Mallah MH, Grossman GB, Hansen CL, Hendel RC, Kerwin TC, McCallister BD, Jr., Mehta R, Polk DM, Tilkemeier PL and others. American Society of Nuclear Cardiology review of the ACCF/ASNC appropriateness criteria for single-photon emission computed tomography myocardial perfusion imaging (SPECT MPI). J Nucl Cardiol 2007;14(6):e26-38.

26.   Salerno M, Beller GA. Noninvasive Assessment of Myocardial Perfusion. Circulation-Cardiovascular Imaging 2009;2(5):412-424.

27.   Saghari M, Assadi M, Eftekhari M, Yaghoubi M, Fard-Esfahani A, Malekzadeh JM, Sichani BF, Beiki D, Takavar A. Frequency and severity of myocardial perfusion

abnormalities using Tc-99m MIBI SPECT in cardiac syndrome X. BMC Nucl Med 2006;6:1.

28. Schwaiger M. Myocardial Perfusion Imaging with Pet. Journal of Nuclear Medicine 1994;35(4):693-698.

29. Marwick TH, Cook SA, Lafont A, Underwood DA, Salcedo EE. Influence of left ventricular mass on the diagnostic accuracy of myocardial perfusion imaging using positron emission tomography with dipyridamole stress. J Nucl Med 1991;32(12):2221-6.

30. Yoshinaga K, Chow BJ, Williams K, Chen L, deKemp RA, Garrard L, Lok-Tin Szeto A, Aung M, Davies RA, Ruddy TD and others. What is the prognostic value of myocardial perfusion imaging using rubidium-82 positron emission tomography? J Am Coll Cardiol 2006;48(5):1029-39.

31. Wei K, Jayaweera AR, Firoozan S, Linka A, Skyba DM, Kaul S. Quantification of myocardial blood flow with ultrasound-induced destruction of microbubbles administered as a constant venous infusion. Circulation 1998;97(5):473-483.

32. Takx RA, Blomberg BA, El Aidi H, Habets J, de Jong PA, Nagel E, Hoffmann U, Leiner T. Diagnostic accuracy of stress myocardial perfusion imaging compared to invasive coronary angiography with fractional flow reserve meta-analysis. Circ Cardiovasc Imaging 2015;8(1).

33. Cademartiri F, Mollet NR, van der Lugt A, McFadden EP, Stijnen T, de Feyter PJ, Krestin GP. Intravenous contrast material administration at helical 16-detector row CT coronary angiography: Effect of iodine concentration on vascular attenuation. Radiology 2005;236(2):661-665.

34.   Murthy VL, Naya M, Foster CR, Gaber M, Hainer J, Klein J, Dorbala S, Blankstein R, Di Carli MF. Association Between Coronary Vascular Dysfunction and Cardiac Mortality in Patients With and Without Diabetes Mellitus. Circulation 2012;126(15):1858-U178.

35.   Taqueti VR, Hachamovitch R, Murthy VL, Naya M, Foster CR, Hainer J, Dorbala S, Blankstein R, Di Carli MF. Global Coronary Flow Reserve Is Associated With Adverse Cardiovascular Events Independently of Luminal Angiographic Severity and Modifies the Effect of Early Revascularization. Circulation 2015;131(1):19-+.

36.   Di Carli MF, Charytan D, McMahon GT, Ganz P, Dorbala S, Schelbert HR. Coronary Circulatory Function in Patients with the Metabolic Syndrome. Journal of Nuclear Medicine 2011;52(9):1369-1377.

37.   Naya M, Murthy VL, Taqueti VR, Foster CR, Klein J, Garber M, Dorbala S, Hainer J, Blankstein R, Resnic F and others. Preserved Coronary Flow Reserve Effectively Excludes High-Risk Coronary Artery Disease on Angiography. Journal of Nuclear Medicine 2014;55(2):248-255.

38.   Earls JP, Ho VB, Foo TK, Castillo E, Flamm SD. Cardiac MRI: recent progress and continued challenges. J Magn Reson Imaging 2002;16(2):111-27.

39.   Tofts PS. Modeling tracer kinetics in dynamic Gd-DTPA MR imaging. Jmri-Journal of Magnetic Resonance Imaging 1997;7(1):91-101.

40.   Jerosch-Herold M, Wilke N, Stillman AE. Magnetic resonance quantification of the myocardial perfusion reserve with a Fermi function model for constrained deconvolution. Med Phys 1998;25(1):73-84.

41. Jerosch-Herold M, Swingen C, Seethamraju RT. Myocardial blood flow quantification with MRI by model-independent deconvolution. Medical Physics 2002;29(5):886-897.

42. Ichihara T, Ishida M, Kitagawa K, Ichikawa Y, Natsume T, Yamaki N, Maeda H, Takeda K, Sakuma H. Quantitative Analysis of First-Pass Contrast-Enhanced Myocardial Perfusion MRI Using a Patlak Plot Method and Blood Saturation Correction. Magnetic Resonance in Medicine 2009;62(2):373-383.

43. Pack NA, DiBella EV. Comparison of myocardial perfusion estimates from dynamic contrast-enhanced magnetic resonance imaging with four quantitative analysis methods. Magn Reson Med 2010;64(1):125-37.

44. Patel AR, Antkowiak PF, Nandalur KR, West AM, Salerno M, Arora V, Christopher J, Epstein FH, Kramer CM. Assessment of advanced coronary artery disease: advantages of quantitative cardiac magnetic resonance perfusion analysis. J Am Coll Cardiol 2010;56(7):561-9.

45. Adluru G, McGann C, Speier P, Kholmovski EG, Shaaban A, Dibella EV. Acquisition and reconstruction of undersampled radial data for myocardial perfusion magnetic resonance imaging. J Magn Reson Imaging 2009;29(2):466-73.

46. Shin T, Nayak KS, Santos JM, Nishimura DG, Hu BS, McConnell MV. Three-dimensional first-pass myocardial perfusion MRI using a stack-of-spirals acquisition. Magnetic Resonance in Medicine 2013;69(3):839-844.

47. Nam S, Akcakaya M, Basha T, Stehning C, Manning WJ, Tarokh V, Nezafat R. Compressed sensing reconstruction for whole-heart imaging with 3D radial

trajectories: a graphics processing unit implementation. Magn Reson Med 2013;69(1):91-102.

48.   Ge L, Kino A, Griswold M, Mistretta C, Carr JC, Li D. Myocardial perfusion MRI with sliding-window conjugate-gradient HYPR. Magn Reson Med 2009;62(4):835-9.

49.   Meyer CH, Hu P. Spiral parallel magnetic resonance imaging. Conf Proc IEEE Eng Med Biol Soc 2006;1:369-71.

50.   Chen W, Meyer CH. Fast automatic linear off-resonance correction method for spiral imaging. Magn Reson Med 2006;56(2):457-62.

51.   Chen W, Meyer CH. Semiautomatic off-resonance correction in spiral imaging. Magn Reson Med 2008;59(5):1212-9.

52.   Pruessmann KP, Weiger M, Scheidegger MB, Boesiger P. SENSE: sensitivity encoding for fast MRI. Magn Reson Med 1999;42(5):952-62.

53.   Griswold MA, Jakob PM, Heidemann RM, Nittka M, Jellus V, Wang J, Kiefer B, Haase A. Generalized autocalibrating partially parallel acquisitions (GRAPPA). Magn Reson Med 2002;47(6):1202-10.

54.   Lustig M, Pauly JM. SPIRiT: Iterative self-consistent parallel imaging reconstruction from arbitrary k-space. Magn Reson Med 2010;64(2):457-71.

55.   Griswold MA, Kannengiesser S, Heidemann RM, Wang JM, Jakob PM. Field-of-view limitations in parallel imaging. Magnetic Resonance in Medicine 2004;52(5):1118-1126.

56.   Donoho DL. Compressed sensing. Ieee Transactions on Information Theory 2006;52(4):1289-1306.

57.   Yang Y, Kramer CM, Shaw PW, Meyer CH, Salerno M. First-pass myocardial perfusion imaging with whole-heart coverage using L1-SPIRiT accelerated variable density spiral trajectories. Magn Reson Med 2015.

58.   Lustig M, Donoho D, Pauly JM. Sparse MRI: The application of compressed sensing for rapid MR imaging. Magn Reson Med 2007;58(6):1182-95.

59.   Motwani M, Maredia N, Fairbairn TA, Kozerke S, Greenwood JP, Plein S. Assessment of ischaemic burden in angiographic three-vessel coronary artery disease with high-resolution myocardial perfusion cardiovascular magnetic resonance imaging. Eur Heart J Cardiovasc Imaging 2014.

60.   Manka R, Jahnke C, Kozerke S, Vitanis V, Crelier G, Gebker R, Schnackenburg B, Boesiger P, Fleck E, Paetsch I. Dynamic 3-Dimensional Stress Cardiac Magnetic Resonance Perfusion Imaging Detection of Coronary Artery Disease and Volumetry of Myocardial Hypoenhancement Before and After Coronary Stenting. Journal of the American College of Cardiology 2011;57(4):437-444.

61.   Manka R, Wissmann L, Gebker R, Jogiya R, Motwani M, Frick M, Reinartz S, Schnackenburg B, Niemann M, Gotschy A and others. Multicenter Evaluation of Dynamic Three-Dimensional Magnetic Resonance Myocardial Perfusion Imaging for the Detection of Coronary Artery Disease Defined by Fractional Flow Reserve. Circulation-Cardiovascular Imaging 2015;8(5).

62.   Salerno M, Sica C, Kramer CM, Meyer CH. Improved first-pass spiral myocardial perfusion imaging with variable density trajectories. Magn Reson Med 2013;70(5):1369-79.

63.   Chen L, Adluru G, Schabel MC, McGann CJ, Dibella EV. Myocardial perfusion MRI with an undersampled 3D stack-of-stars sequence. Med Phys 2012;39(8):5204-11.

64.   Shin T, Nayak KS, Santos JM, Nishimura DG, Hu BS, McConnell MV. Three-dimensional first-pass myocardial perfusion MRI using a stack-of-spirals acquisition. Magn Reson Med 2012.

65.   Otazo R, Kim D, Axel L, Sodickson DK. Combination of compressed sensing and parallel imaging for highly accelerated first-pass cardiac perfusion MRI. Magn Reson Med 2010;64(3):767-76.

66.   Lingala SG, Hu Y, DiBella E, Jacob M. Accelerated dynamic MRI exploiting sparsity and low-rank structure: k-t SLR. IEEE Trans Med Imaging 2011;30(5):1042-54.

67.   Chen X, Salerno M, Yang Y, Epstein FH. Motion-compensated compressed sensing for dynamic contrast-enhanced MRI using regional spatiotemporal sparsity and region tracking: block low-rank sparsity with motion-guidance (BLOSM). Magn Reson Med 2014;72(4):1028-38.

68.   Atkinson DJ, Burstein D, Edelman RR. First-pass cardiac perfusion: evaluation with ultrafast MR imaging. Radiology 1990;174(3 Pt 1):757-62.

69.   Salerno M, Taylor A, Yang Y, Kuruvilla S, Ragosta M, Meyer CH, Kramer CM. Adenosine stress cardiovascular magnetic resonance with variable-density spiral pulse sequences accurately detects coronary artery disease: initial clinical evaluation. Circ Cardiovasc Imaging 2014;7(4):639-46.

70. Plein S, Ryf S, Schwitter J, Radjenovic A, Boesiger P, Kozerke S. Dynamic contrast-enhanced myocardial perfusion MRI accelerated with k-t SENSE. Magnetic Resonance in Medicine 2007;58(4):777-785.

71. Pedersen H, Kozerke S, Ringgaard S, Nehrke K, Kim WY. k-t PCA: Temporally Constrained k-t BLAST Reconstruction Using Principal Component Analysis. Magnetic Resonance in Medicine 2009;62(3):706-716.

72. Adluru G, Awate SP, Tasdizen T, Whitaker RT, Dibella EV. Temporally constrained reconstruction of dynamic cardiac perfusion MRI. Magn Reson Med 2007;57(6):1027-36.

73. Jahnke C, Nagel E, Gebker R, Kokocinski T, Kelle S, Manka R, Fleck E, Paetsch I. Prognostic value of cardiac magnetic resonance stress tests: adenosine stress perfusion and dobutamine stress wall motion imaging. Circulation 2007;115(13):1769-76.

74. Kellman P, Derbyshire JA, Agyeman KO, McVeigh ER, Arai AE. Extended coverage first-pass perfusion imaging using slice-interleaved TSENSE. Magn Reson Med 2004;51(1):200-4.

75. Plein S, Radjenovic A, Ridgway JP, Barmby D, Greenwood JP, Ball SG, Sivananthan MU. Coronary artery disease: myocardial perfusion MR imaging with sensitivity encoding versus conventional angiography. Radiology 2005;235(2):423-30.

76. Meyer CH, Hu BS, Nishimura DG, Macovski A. Fast spiral coronary artery imaging. Magn Reson Med 1992;28(2):202-13.

77. Chen X, Salerno M, Epstein FH, Meyer CH. Accelerated multi-TI spiral MRI using compressed sensing with temporal constraints. 2011; Montreal. p 4369.

78. Kim YC, Narayanan SS, Nayak KS. Flexible retrospective selection of temporal resolution in real-time speech MRI using a golden-ratio spiral view order. Magn Reson Med 2011;65(5):1365-71.

79. Tannus A, Garwood M. Adiabatic pulses. NMR Biomed 1997;10(8):423-34.

80. Yang Y, Chen X, Feng X, Wang M, Epstein F, Meyer C, Salerno M. Evaluation of parallel reconstruction techniques for first-pass perfusion imaging using spiral trajectories. Proceedings of the 20th Annual Meeting of ISMRM, Melbourne, Australia 2012:3956.

81. Salerno M, Yang Y, Shaw P, Taylor A, Meyer C, Epstein F, Kramer C. High Resolution Quantitative Spiral CMR Perfusion Imaging Demonstrates a Reduced Endocardial to Epicardial Perfusion Gradient and Myocardial Flow Reserve in Patients with Microvascular Disease. Proc Intl Soc Mag Reson Med 2015(23):4484.

82. Yang Y, Feng X, Meyer CH, Kramer CM, Salerno M. First-pass myocardial perfusion imaging with whole ventricular coverage using L1-SPIRIT accelerated spiral trajectories. Journal of Cardiovascular Magnetic Resonance 2013;15(Suppl 1):P20.

83. M. Lustig MA, S. Vasanawala, D. L. Donoho, and J. M. Pauly. L1 SPIR-iT: Autocalibrating Parallel Imaging Compressed Sensing. Proc. Intl. Soc. Mag. Reson. Med. 17 2009.

84. Fessler JA, Sutton BP. Nonuniform fast Fourier transforms using min-max interpolation. Ieee Transactions on Signal Processing 2003;51(2):560-574.

85. Wang Z, Bovik AC, Sheikh HR, Simoncelli EP. Image quality assessment: from error visibility to structural similarity. IEEE Trans Image Process 2004;13(4):600-12.

86. Manka R, Paetsch I, Kozerke S, Moccetti M, Hoffmann R, Schroeder J, Reith S, Schnackenburg B, Gaemperli O, Wissmann L and others. Whole-heart dynamic three-dimensional magnetic resonance perfusion imaging for the detection of coronary artery disease defined by fractional flow reserve: determination of volumetric myocardial ischaemic burden and coronary lesion location. Eur Heart J 2012;33(16):2016-24.

87. Huang W, Yang Y, Chen X, Salerno M. Simple Motion Correction Strategy Reduces Respiratory-Induced Motion Artifacts for K-T Accelerated CMR Perfusion Imaging. Proc Intl Soc Mag Reson Med 2015(23):3686.

88. Yang Y, Chen X, Epstein FH, Meyer CH, Kuruvilla S, Kramer CM, Salerno M. Motion-corrected compressed-sensing enables robust spiral first-pass perfusion imaging with whole heart coverage. Journal of Cardiovascular Magnetic Resonance 2014;16(Suppl 1):O81.

89. Wilm BJ, Svensson J, Henning A, Pruessmann KP, Boesiger P, Kollias SS. Reduced field-of-view MRI using outer volume suppression for spinal cord diffusion imaging. Magn Reson Med 2007;57(3):625-30.

90. Le Roux P, Gilles RJ, McKinnon GC, Carlier PG. Optimized outer volume suppression for single-shot fast spin-echo cardiac imaging. J Magn Reson Imaging 1998;8(5):1022-32.

91. Pisani L, Bammer R, Glover G. Restricted field of view magnetic resonance imaging of a dynamic time series. Magn Reson Med 2007;57(2):297-307.

92. Smith TB, Nayak KS. Reduced field of view MRI with rapid, B1-robust outer volume suppression. Magn Reson Med 2012;67(5):1316-23.

93. Luo J, Addy NO, Ingle RR, Hargreaves BA, Hu BS, Nishimura DG, Shin T. Combined outer volume suppression and T preparation sequence for coronary angiography. Magn Reson Med 2014.

94. Jivan A, Horsfield MA, Moody AR, Cherryman GR. Dynamic T1 measurement using snapshot-FLASH MRI. J Magn Reson 1997;127(1):65-72.

95. Epstein FH, Wolff SD, Arai AE. Segmented k-space fast cardiac imaging using an echo-train readout. Magnetic Resonance in Medicine 1999;41(3):609-613.

96. Schreiber WG, Schmitt M, Kalden P, Mohrs OK, Kreitner KF, Thelen M. Dynamic contrast-enhanced myocardial perfusion imaging using saturation-prepared TrueFISP. J Magn Reson Imaging 2002;16(6):641-52.

97. Tsai CM, Nishimura DG. Reduced aliasing artifacts using variable-density k-space sampling trajectories. Magnetic Resonance in Medicine 2000;43(3):452-458.

98. Staewen RS, Johnson AJ, Ross BD, Parrish T, Merkle H, Garwood M. 3-D FLASH imaging using a single surface coil and a new adiabatic pulse, BIR-4. Invest Radiol 1990;25(5):559-67.

99. Pauly J, Nishimura D, Macovski A. A k-space analysis of small-tip-angle excitation. 1989. J Magn Reson 2011;213(2):544-57.

100. Combettes PL, Wajs VR. Signal recovery by proximal forward-backward splitting. Multiscale Modeling & Simulation 2005;4(4):1168-1200.

101. Furberg CD, Psaty BM, Manolio TA, Gardin JM, Smith VE, Rautaharju PM. Prevalence of Atrial-Fibrillation in Elderly Subjects (the Cardiovascular Health Study). American Journal of Cardiology 1994;74(3):236-241.

102. Dewey FE, Freeman JV, Engel G, Oviedo R, Abrol N, Ahmed N, Myers J, Froelicher VF. Novel predictor of prognosis from exercise stress testing: heart rate variability response to the exercise treadmill test. Am Heart J 2007;153(2):281-8.

103. Greenwood JP, Maredia N, Younger JF, Brown JM, Nixon J, Everett CC, Bijsterveld P, Ridgway JP, Radjenovic A, Dickinson CJ and others. Cardiovascular magnetic resonance and single-photon emission computed tomography for diagnosis of coronary heart disease (CE-MARC): a prospective trial. Lancet 2012;379(9814):453-460.

104. Shah R, Heydari B, Coelho-Filho O, Murthy VL, Abbasi S, Feng JH, Pencina M, Neilan TG, Meadows JL, Francis S and others. Stress cardiac magnetic resonance imaging provides effective cardiac risk reclassification in patients with known or suspected stable coronary artery disease. Circulation 2013;128(6):605-14.

105. Camici PG, Rimoldi OE. The Clinical Value of Myocardial Blood Flow Measurement. Journal of Nuclear Medicine 2009;50(7):1076-1087.

106. Lee DC, Johnson NP. Quantification of absolute myocardial blood flow by magnetic resonance perfusion imaging. JACC Cardiovasc Imaging 2009;2(6):761-70.

107. Wang L, Jerosch-Herold M, Jacobs DR, Shahar E, Detrano R, Folsom AR. Coronary artery calcification and myocardial perfusion in asymptomatic adults -

The MESA (multi-ethnic study of atherosclerosis). Journal of the American College of Cardiology 2006;48(5):1018-1026.

108. Christian TF, Rettmann DW, Aletras AH, Liao SL, Taylor JL, Balaban RS, Arai AE. Absolute myocardial perfusion in canines measured by using dual-bolus first-pass MR imaging. Radiology 2004;232(3):677-84.

109. Kim D, Axel L. Multislice, dual-imaging sequence for increasing the dynamic range of the contrast-enhanced blood signal and CNR of myocardial enhancement at 3T. J Magn Reson Imaging 2006;23(1):81-6.

110. Gatehouse PD, Elkington AG, Ablitt NA, Yang GZ, Pennell DJ, Firmin DN. Accurate assessment of the arterial input function during high-dose myocardial perfusion cardiovascular magnetic resonance. J Magn Reson Imaging 2004;20(1):39-45.

111. Cernicanu A, Axel L. Theory-based signal calibration with single-point T1 measurements for first-pass quantitative perfusion MRI studies. Acad Radiol 2006;13(6):686-93.

112. Avants BB, Tustison NJ, Song G, Cook PA, Klein A, Gee JC. A reproducible evaluation of ANTs similarity metric performance in brain image registration. Neuroimage 2011;54(3):2033-44.

113. Stab D, Wech T, Breuer FA, Weng AM, Ritter CO, Hahn D, Kostler H. High resolution myocardial first-pass perfusion imaging with extended anatomic coverage. J Magn Reson Imaging 2013.

114. Yutzy SR, Seiberlich N, Duerk JL, Griswold MA. Improvements in multislice parallel imaging using radial CAIPIRINHA. Magn Reson Med 2011;65(6):1630-7.

115.   Breuer FA, Blaimer M, Heidemann RM, Mueller MF, Griswold MA, Jakob PM. Controlled aliasing in parallel imaging results in higher acceleration (CAIPIRINHA) for multi-slice imaging. Magn Reson Med 2005;53(3):684-91.